Additive Manufacturing of Lunar Regolith and Regolith-Based Composites for Sustainable Manufacturing on the Moon

Mohammad Azami

A Thesis

in

The Department

of

Electrical and Computer Engineering

Presented in Partial Fulfillment of the Requirements

for the Degree of

Doctor of Philosophy (Electrical and Computer Engineering) at

Concordia University

Montréal, Québec, Canada

November 2025

CONCORDIA UNIVERSITY

School of Graduate Studies

This is to certify that the thesis prepared

By: **Mr. Mohammad Azami**

Entitled: **Additive Manufacturing of Lunar Regolith and Regolith-Based Composites for Sustainable Manufacturing on the Moon**

and submitted in partial fulfillment of the requirements for the degree of

Doctor of Philosophy (Electrical and Computer Engineering)

complies with the regulations of this University and meets the accepted standards with respect to originality and quality.

Signed by the Final Examining Committee:

________________________________ Chair
Prof. Chunjiang An

________________________________ External Examiner
Prof. Frédérick Gosselin

________________________________ External to Program
Prof. Mehdi Hojjati

________________________________ Examiner
Prof. Rastko Selmic

________________________________ Examiner
Prof. Mojtaba Kahrizi

________________________________ Supervisor
Prof. Krzysztof Skonieczny

Approved by ____
Abdelwahab Hamou-Lhadj, Chair
Department of Electrical and Computer Engineering

Novermber 17, 2025

____
Mourad Debbabi, Dean
Faculty of Engineering and Computer Science

Abstract

Additive Manufacturing of Lunar Regolith and Regolith-Based Composites for Sustainable Manufacturing on the Moon

Mohammad Azami, Ph.D.

Concordia University, 2025

NASA's Artemis program targets sustained lunar presence, making in-space manufacturing (ISM) and in-situ resource utilization (ISRU) essential. Materials extrusion (MEX), notably fused filament fabrication (FFF), offers a low-mass, energy-efficient route for ISM. This thesis investigates FFF of space-grade PEEK composites filled with lunar regolith simulant (LRS), supported by modeling and a powder bed fusion (PBF) benchmark.

Using a FFF system, we compounded and printed 70/30 wt% PEEK/LRS (PEEK/LRS30) to study the feasibility of using LRS as a filler, with neat PEEK as baseline. LRS increased melt viscosity and porosity, yielding a ∼27% strength loss attributable to porosity. Fractography showed embrittlement and reduced elongation, and microstructural analysis confirmed uniform LRS dispersion with visible pores. LRS also improved interlayer bonding and reduced warping.

PEEK and LMS-1D LRS were melt-compounded (0–50 wt%), FFF-printed, and annealed at 300 °C. Characterization (density, thermal, tensile, microstructural/elemental) showed all filaments above 96% dense. As-printed porosity rose from below 1% (neat PEEK) to 7.5% at 50 wt% LRS. Regolith increased crystallinity (17.4% → 20.5%) and elastic modulus (6–41%), while reducing delamination/warping and improving dimensional accuracy and yield. Tensile strength fell from 107 to 90 MPa through 40 wt% LRS, then to ∼70 MPa at 50 wt%. Annealing improved density and stiffness up to 30 wt% LRS (diminishing thereafter). Process refinement cut defect size/frequency, raising PEEK/LRS30 tensile strength from 67.1 to 94.8 MPa. At 50 wt% strength and ductility declined more sharply, consistent with micrography-observed defect growth.

Finite element analysis (FEA) of defect-free printed composites matches the measured stiffness up to $\sim 40\ \mathrm{wt}\%$ LRS. The divergence at $50\ \mathrm{wt}\%$ aligns with higher porosity and weak inter-bead bonding. A defect-aware model that incorporates large crack-like discontinuities at layer boundaries derived from micrographs predicts a marked reduction in modulus and, together with mechanistic reasoning, explains the observed gap.

A PBF feasibility study is conducted on regolith simulant and a 20 wt% regolith–Invar 36 composite. FFF is simpler and lower in energy/cost, while PBF enables alternative densification and resilience at higher temperatures with greater on-site use, but poor flowability and weak laser–powder coupling in regolith feeds yield porous parts with frequent large defects. The results include lessons learned on the processability window for key parameters and print conditions.

This study strengthens the technological basis for AM in lunar conditions and accelerates ISM adoption.

Acknowledgements

I am deeply grateful to my supervisor, Prof. Krzysztof Skonieczny, for steadfast guidance, high standards, and generous support throughout this work. He balanced genuine independence with timely, incisive mentorship, trusting me to explore ideas while offering clear direction at pivotal moments. I also thank my examining committee for their time, thoughtful feedback, and for pushing me to sharpen both the methods and the narrative.

I thank Dr. Marie-Josée Potvin at the Canadian Space Agency (CSA) for valuable technical guidance and for framing the broader relevance of this work to ISRU and lunar manufacturing. I am also grateful to Prof. Hojjati for facilitating access to equipment and facilities that enabled key experiments. Their professionalism made this work more rigorous and far more efficient. This thesis was made possible by the daily help and camaraderie of my labmates at Concordia University's Aerospace Robotics Lab (CUARL), especially Pierre-Lucas Aubin-Fournier, for discussions, troubleshooting, and hands-on assistance during long experimental campaigns. I am very thankful to the MSAM Lab (University of Waterloo) for highly valuable expertise, effort, and resources in laser powder bed fusion (LPBF), and especially to Prof. Mihaela Vlasea for mentorship and for enabling access to facilities and expertise critical to the PBF portion of this research. I also acknowledge the Space Copy team, especially Maddison Feehan, for providing resources, technical input, and operational support that directly enabled the PBF study.

I also appreciate my co-authors on the works included in this thesis, beyond those already mentioned, including Zahra Kazemi (University of Toronto); at ÉTS Montréal: Prof. Martine Dubé and Sare Moazen; and at the MSAM Lab: Sagar Patel, Rene Lam, Xavier Walls, Tomisin Oluwajuyigbe, and Alexandra Darroch.

This research was supported by the Natural Sciences and Engineering Research Council of Canada (NSERC), internal support from Concordia University, and FedDev Ontario (Federal Economic Development Agency for Southern Ontario) for financial support of the PBF project. The views and conclusions here are my own; any errors are solely my responsibility.

Finally, I owe the deepest thanks to my family. To my wife, Zahra, your patience, optimism, and unwavering belief carried me through late nights in the lab and at the keyboard. To my parents, whose sacrifices and encouragement made this path possible, and to my brother for his constant support and good counsel, thank you. This thesis is as much yours as it is mine.

Contents

List of Figures

List of Tables

Abbreviations

AM	Additive Manufacturing
AI	Artificial Intelligence
BJ	Binder Jetting
CCC	Cement Contour Crafting
CF	Carbon Fiber
CMC	Ceramic Matrix Composite
CR	Carbothermal Reduction
CT	Computed Tomography
DCM	Dichloromethane
DIC	Digital Image Correlation
DIW	Direct Ink Writing
DED	Directed Energy Deposition
EB-DED	Electron-Beam Directed Energy Deposition
EBM	Electron Beam Melting
EB-PBF	Electron Beam Powder Bed Fusion
EDS	Energy-Dispersive X-Ray Spectroscopy
ESA	European Space Agency
EMR	Extrusion of Molten Regolith
FDM	Fused Deposition Modeling
FFF	Fused Filament Fabrication

FGF	Fused Granulate Fabrication
HIP	Hot Isostatic Pressing
ISM	In-Space Manufacturing
ISRU	In-Situ Resource Utilization
L-DED	Laser Directed Energy Deposition
L-PBF	Laser Powder Bed Fusion
LS	Laser Sintering
LBMC	Lunar-Based Manufacturing and Construction
LRS	Lunar Regolith Simulant
LSCC	Lunar Soil Characterization Consortium
MEX	Materials Extrusion
MMC	Metal Matrix Composite
MOC	Magnesium Oxychloride
MRE	Molten Regolith Electrolysis
MRS	Martian Regolith Simulant
MSE	Molten Salt Electrolysis
MWS	Microwave Sintering
MWS-PBF	Microwave Sintering Powder Bed Fusion
PA	Polyamide
PE	Polyethylene
PEEK	Polyether ether ketone
PEKK	Polyether ketone ketone
PI	Polyimide
PSD	Particle Size Distribution
PMC	Polymer Matrix Composite
PLGA	Polylactic-co-glycolic Acid
PBF	Powder Bed Fusion

PCA	Process Control Agent
PMA	Polymer Micro-Agglomerates
RVE	Representative Volume Element
SEM	Scanning Electron Microscopy
SLAAM	Simultaneous Localization and Additive Manufacturing
SLM	Selective Laser Melting
SLS	Selective Laser Sintering
SMWS	Selective Microwave Sintering
SSLS	Selective Solar Light Sintering
SS	Solar Sintering
SS-PBF	Solar Sintering Powder Bed Fusion
SPS	Spark Plasma Sintering
SLA	Stereolithography Apparatus
TES	Thermal Energy Storage
TMS	Technological Maturity Stage
WAAM	Wire Arc Additive Manufacturing
XRD	X-Ray Diffraction

Chapter 1

Introduction

This chapter is based on, and in parts reproduces with minor editorial changes, the following published work:

Azami, M., Kazemi, Z., Moazen, S., Dubé, M., Potvin, M.-J., and Skonieczny, K. (2024). A comprehensive review of Lunar-based manufacturing and construction. *Progress in Aerospace Sciences* 150, 101045. doi:10.1016/j.paerosci.2024.101045.

1.1 Motivation

Humanity is planning to return to the Moon under NASA's Artemis program. In parallel, multiple nations are fielding robotic landers and orbiters at an accelerating pace [16]. Most of these missions are self-contained: if something fails, there is no in-situ repair. Recent successes have been tempered by notable losses [17], underscoring the operational difficulty of the Lunar environment. Payload constraints have also favored small rover deployments over larger, more capable systems because placing mass in Lunar vicinity remains costly and complex.

However, bringing humans back to the Moon for more than a few hours at a time will require substantial installations, many of which will be crucial for human survival and will need methods for repair and maintenance. Planning to bring every conceivable spare part would be infeasible. Therefore, means to fabricate on-site what is required to develop, maintain, and repair systems are essential. Likewise, delivering bulk feedstocks from Earth is prohibitively expensive, reinforcing the imperative to exploit local resources via in-situ resource utilization (ISRU). Reducing dependence on Earth-sourced materials by leveraging Lunar regolith and other indigenous resources is therefore a central objective [18, 19]. These drivers motivate Lunar-Based Manufacturing and Construction (LBMC), spanning traditional and additive approaches and tailored to the Moon's environmental and operational constraints.

Additive manufacturing (AM) is particularly attractive for LBMC. AM reduces material waste, can lower energy usage, enables complex geometries, and supports on-demand customization [2, 20–22]. These attributes matter where many parts are first-of-a-kind, logistics are constrained, and equipment mass and volume must be minimized. Practical Lunar implementations may combine compact printers for small components with mobile or scalable systems for structural elements [23–25]. Within this landscape, incorporating Lunar regolith into AM feedstocks is an active research area [24, 26]. Because returned Lunar soil is scarce, numerous Lunar regolith simulants (LRS) have been developed to emulate key physical and chemical properties and to enable technology maturation on Earth [27–30].

Among AM modalities, binder-based methods are appealing for Lunar use because they are generally more tolerant of regolith compositional variability than sintering or melting routes such as powder-bed fusion. Material extrusion (MEX), especially fused filament fabrication (FFF), offers additional advantages by employing solid thermoplastic binders that avoid the handling, outgassing, and temperature-management challenges associated with liquid binders in vacuum and extreme thermal environments [4]. MEX is mechanically simple, compatible with low-gravity printing demonstrations, and well suited to integration on small, mobile robotic platforms that are preferred for in-space manufacturing (ISM) [25, 31–34]. These characteristics position MEX as a promising pathway for responsive, fieldable Lunar fabrication.

Thermoplastic binder selection is critical. Many common polymers are not viable for Lunar day temperatures of 120–130 °C [24, 35]. For instance, polylactic acid (PLA) has $T_{\mathrm{g}} \approx 55\text{–}65\,^{\circ}\mathrm{C}$ and $T_{\mathrm{m}} \approx 160\text{–}170\,^{\circ}\mathrm{C}$ [36, 37], while polyethylene families have even lower T_{g} and modest T_{m} [38–40]. Under unshielded Lunar conditions, such materials soften or deform, and many do not satisfy NASA's strict vacuum outgassing limits. By contrast, polyether–ether–ketone (PEEK) combines thermal stability ($T_{\mathrm{g}} = 143\,^{\circ}\mathrm{C}$, $T_{\mathrm{m}} = 343\,^{\circ}\mathrm{C}$), acceptable outgassing behavior, and resistance to radiation, chemicals, and abrasive dust, while remaining compatible with MEX [41–44]. PEEK is thus a strong candidate binder for Lunar MEX.

Significant challenges remain for PEEK–regolith composites. PEEK printing demands tight thermal control, as fluctuations can introduce residual stresses, warpage, and poor interlayer bonding. PEEK's relatively high melt viscosity complicates both compounding and extrusion [41, 45]. From a logistics perspective, PEEK must be Earth-supplied because Lunar regolith lacks carbon for in-situ polymer synthesis. Increasing regolith content reduces reliance on imported polymer but raises composite viscosity, which can hinder mixing, flow, and print quality [46]. Finally, while PEEK is more recyclable than many high-performance polymers, repeated thermal cycles still degrade properties, so processes that limit re-melt and rework are desirable [47, 48].

Prior MEX studies with regolith-filled PLA demonstrate the general feasibility of extrusion with particulate Lunar media, including under simulated thermal-vacuum conditions, but they also highlight the material limitations of PLA for outdoor Lunar use [49]. By comparison, the use of space-grade, high-temperature thermoplastics as binders for regolith-rich composites remains underexplored. This gap motivates the present work: we develop PEEK-based, regolith-rich feedstocks and establish MEX AM process windows that enable robust, low-waste, and maintainable fabrication for LBMC, thereby reducing launch mass, supporting on-site repair, and accelerating progress toward sustained Lunar operations.

1.2 Problem statement

The overall problem is to enable reliable on-site fabrication and repair of functional parts on the Lunar surface using material-extrusion additive manufacturing with regolith-rich, space-grade thermoplastic binders (e.g., PEEK), with consideration of the coupled constraints of low gravity, hard vacuum with strict outgassing limits, extreme thermal gradients, and tight energy, mass, and volume budgets. The process must maximize in-situ resource utilization by accommodating high regolith loadings while minimizing Earth-supplied polymers and additives, maintain extrudability and interlayer bonding, and deliver parts with low porosity, low warpage, and sufficient mechanical and thermal stability for Lunar service.

1.3 Literature review

Additive manufacturing (AM) is a method in which components are created by depositing successive layers until a 3D structure is formed. AM empowers various industries to craft intricate shapes using a variety of materials, including metals, polymers, ceramics, and composites. It is revolutionizing numerous sectors, including construction, aerospace, automotive, food production, healthcare, electronics, and fashion, due to its capacity for customization and its ability to reduce both production time and material/energy waste [50, 51]. Various AM techniques can be categorized into seven primary groups: powder bed fusion [2, 20, 52], material jetting [53, 54], material extrusion [55, 56], binder jetting [57, 58], directed energy deposition [59, 60], vat polymerization [61, 62], and sheet lamination [63, 64].

When it comes to polymers or polymer matrix composites, AM is typically carried out through three principal methods: material extrusion, specifically fused filament fabrication (FFF) [65, 66]; vat polymerization, also known as stereolithography (SLA) [67, 68]; and powder bed fusion, specifically selective laser sintering (SLS) [69, 70].

1.3.1 Lunar regolith

Lunar regolith is the most abundant substance on the Moon [71]. Based on specimens collected from various Lunar regions during the Apollo missions, Lunar regolith primarily consists of Plagioclase, Pyroxene, Olivine, Silica, Ilmenite, Mare glass, and Highland glass, albeit in varying proportions [26]. During the Apollo missions, only 400 kg of regolith were collected and returned to Earth. As a result, researchers have endeavored to develop Lunar regolith simulants (LRS) with the goal of replicating them as closely as possible in terms of chemical composition, crystal structure, particle size distribution, and other characteristics [61].

In existing literature, various manufacturing techniques have been employed to manufacture samples using different Lunar regolith simulants. For example, Goulas et al. [72] used Laser-PBF to 3D print samples composed entirely of JSC-1A. Altun et al. [61] employed SLA-based ceramic fabrication, followed by debinding and sintering, to produce components from EAC-1A. Fateri et al. [73] chose solar sintering as the method for additively manufacturing JSC-2A specimens. Pilehver et al. [56] applied extrusion-based AM to print samples of DNA-1 mixed with an alkaline solution and urea. Additionally, Toutanji et al. [74] used casting techniques to create sulfur concrete based on JSC-1A.

1.3.2 Material Extrusion

Material Extrusion (ME) is categorized within ASTM's classification of AM technology, officially defined as a specific additive manufacturing process where the material is deposited through a nozzle or orifice [75]. Fused Filament Fabrication (FFF), also known as Fused Deposition Modeling (FDM), is a major subcategory of MEX and one of the most widely adopted AM techniques overall. Direct Ink Writing (DIW) is another significant subcategory of ME. Another intriguing category within ME, particularly relevant for AM using regolith, involves the extrusion of molten regolith, typically produced as a by-product during regolith oxygen extraction.

Fused Filament Fabrication Fused Filament Fabrication (FFF) is one of the most commonly used AM techniques for manufacturing objects from a filament, usually made of thermoplastic polymers. This method involves a layer-by-layer process in which the 3D printer warms up the thermoplastic material until it loses enough viscosity to be deposited in bead-like patterns to build individual layers [22, 45]. FFF is recognized as one of the most cost-effective AM techniques, requiring lower energy levels compared to other AM methods, minimizing the waste of materials, and being very effective in terms of manufacturing time [76–78]. Also, it does not involve the usage of any liquid-phase material. It has also been proven to work well in low-gravity or zero-gravity conditions [31, 32]. All these features make it a promising method to be used in a Lunar environment.

However, considering the extreme heating/cooling cycles that occur, along with the outgassing requirements [44], not all materials can be used as feedstock for FFF on the Lunar surface. High-performance thermoplastic polymers like Polyether ether ketone (PEEK) [79], Polyether ketone ketone (PEKK) [80], and Polyetherimide (PEI) [81], along with their composites containing glass fiber [82], carbon fiber [81, 83], and ceramic particles [84], have gained particular attention for in-space manufacturing. The reinforcement part can be added to improve the material's specific properties or make it easier to fabricate. For example, adding chopped carbon fiber can enhance the mechanical strength of the polymers [85] and simplify the printing process by forming a more uniform heat distribution in the part while printing, reducing the probability of warpage caused by thermal stresses [86]. Despite ongoing research in space agencies, including NASA [87], and academia, there remains a research gap in the literature concerning ISRU-based FFF. This method involves incorporating on-site materials, such as Lunar regolith, into a space-grade polymeric binder to reduce the cost of raw material launches and enhance the properties of the final product. When it comes to AM of polymer/regolith, in comparison to methods with the potential to use 100% ISRU-based materials, such as PBF, it is important to note that this method is not entirely reliant on ISRU and necessitates the use of off-site materials. Nonetheless, the inclusion of polymer in the composition of the fabricated component offers several advantages. The polymer can sustain stresses and transfer them to reinforcing fiber or other agents. The beneficial effects of the polymer on ductility, toughness, and elongation have been extensively validated [2, 88, 89].

Gelino et al. [49] studied various regolith/Polylactic Acid (PLA) formulations. They tested mixtures including 70:30, 80:20, and 85:15 weight percent ratios of Lunar mare simulant Black Point-1 (BP-1) with PLA, an 80:20 mixture of Lunar Highlands Simulant-1 (LHS-1) with PLA, and an 80:20 BP-1 with PLA blend that included a flow enhancer additive. These samples were printed under simulated Lunar dirty thermal vacuum conditions (-190 °C, 10^{-3} torr). Each formulation underwent several tests to evaluate the achieved mixture ratio, mechanical strength, outgassing products during vacuum printing, and the porosity and density of the printed items. The LHS-1/PLA composite exhibited a favorable combination of properties and was used in the AM of the samples and the subsequent tests. The 80:20 LHS-1 weight percent formulation was selected as the preferred material because the regolith simulant closely represents the south polar Lunar regions and the composite has acceptable mechanical properties. This formulation achieved a flexural modulus of 5.3 GPa and flexural strength of 24 MPa in the 0° orientation. Despite the promising results, PLA is not suitable as a space-grade polymer and does not meet NASA's outgassing standards or the temperature resistance requirements for Lunar conditions.

PEEK is particularly well-suited for use in extraterrestrial environments, especially Lunar conditions, due to its 3D printability, high glass transition temperature Tg (143 °C), and operating temperature (250 °C). It also offers high tensile strength (around 100 MPa) and low density (1320 $\mathrm{kg/m^3}$), meets NASA and ESA's outgassing requirements, high radiation and chemical resistance, and a semi-crystalline structure. These characteristics make it a potential alternative to metals in some applications and a suitable choice for structural and mechanical applications [41, 90, 91].

However, printing PEEK can be challenging due to its semi-crystalline nature, high melting point, and high melt viscosity. Printing PEEK in a heated environment is usually recommended, at a minimum of 70 °C, preferably above 150 °C. Given the high printing temperature of PEEK, printing at room temperature increases the cooling rate, causing significant temperature gradients and thermal stresses in part, resulting in warpage, low fabrication accuracy, poor layer adhesion, or even delamination thereafter. Therefore, it is typically printed on a heated bed and in a heated environment, with a low printing speed [41, 92, 93]. In some studies, the as-fabricated PEEK samples underwent an annealing heat-treatment phase to allow them to recrystallize and improve their mechanical properties [94–96]. However, when printing in a vacuum environment, due to the lack of a convection cooling mechanism, the cooling rate is lower compared to a non-vacuum ambient, resulting in lower temperature gradients. Liu et al. [92] showed that similar or slightly better tensile properties can be expected when printing PEEK in a vacuum, compared to the results obtained with a 150 °C ambient air temperature by Yang et al. [96]. This is a promising conclusion for Lunar-based manufacturing, facilitating the printing requirements in a vacuum.

Liu et al. [92] employed a 100 MPa vacuum environment for printing PEEK samples using FFF. They observed an improvement in the crystallinity of the samples, increasing from 14.9% to 27.8%, representing an 86.6% increase. This rise in crystallinity resulted in a shift in fracture behavior, transitioning from ductile failure to brittle failure, as anticipated. The parts printed in the vacuum environment achieved a relative density of 99.37%.

One remaining challenge in the FFF of materials, particularly PEEK, is the significant anisotropy in different directions. While the strength in the plane parallel to the layers (X-Y plane) is usually acceptable, parts exhibit lower strength levels in the direction perpendicular to the layers (Z direction) [76, 97, 98]. This is attributed to the weaker bonding between adjacent layers compared to the materials in the same layer. This presents challenges for specific applications that require high strength in all directions [98]. Although research is being conducted to reduce this anisotropy in FFF parts [99], the problem persists to some extent. Designers typically consider this limitation when designing for AM.

In a study conducted by Arif et al. [76], the effect of build orientation on the mechanical properties of PEEK (Victrex® 450G) samples was investigated. It was found that the tensile strength of the samples with building orientations and raster angles of horizontal/0°, horizontal/90°, and vertical/90° is 82.58±1.03 MPa (at yield), 72.88±1.92 MPa (at break), and 9.99±0.94 MPa (at break), respectively, which represents a reduction of more than 87% from horizontal/0° to vertical/90° samples. In comparison, the tensile strength of molded PEEK is 98 MPa (at yield). Furthermore, the horizontal/90° and vertical/90° samples exhibited brittle fracture behavior, with tensile elongation percentages of 2.91±0.14% and 0.33±0.03%, respectively. In contrast, the horizontal/0°and molded samples displayed ductile fracture characteristics, with tensile elongation percentages of 110.97±5.31% and 45%, respectively [76].

Polyetherimide (PEI) is another high-performance thermoplastic polymer that, in contrast to PEEK, lacks a distinct crystalline structure. The presence of imide groups imparts impressive mechanical and thermal properties to PEI. Additionally, the inclusion of ether groups within the polymer's structure introduces chain flexibility, contributing to its favorable printability in the molten state. It should be noted that when compared to PEEK, PEI shows a reduced service temperature range [100, 101].

PEI has a 1.27 g/cm^3 density and a tensile stress (at yield) of 110 MPa. PEI boasts a wide processing temperature range, spanning from 350 °C to 425 °C, and exhibits a high glass transition temperature, ranging from 217 °C to 250 °C. Consequently, PEI finds applications in various industries, including aerospace. Similar to PEEK, its outgassing values fall within the allowable range specified by NASA for in-space processing. Furthermore, owing to its favorable melt viscosity, PEI has gained popularity as a material of choice for AM techniques, such as FFF. ULTEM® is one of the most renowned PEI brands, initially introduced to the market by General Electric in 1982 [100–102].

Despite its lower operating temperature compared to PEEK and its high tendency to absorb moisture, which can result in print quality issues [103], PEI offers several advantages over PEEK, particularly in the context of space applications. PEI is often considered easier to work with for 3D printing due to its lower printing temperature, improved layer adhesion at similar ambient temperatures, and lower melt viscosity. This also makes it suitable for open printing environments [104]. Another advantage of PEI is its inherent flame resistance. PEI boasts a high Limiting Oxygen Index (LOI) and carries a UL-94 V-0 rating [100]. Additionally, PEI can be transparent, a property that proves advantageous in applications where visibility or light transmission is required [101]. Furthermore, PEI tends to be more budget-friendly, although this advantage may be marginal for space-related applications when compared to other incurred costs. It should be noted that PEI and PEEK are miscible, allowing for the blending of the two to create PEI/PEEK filament with desired properties [105].

Similar to PEEK, a significant number of experimental [106] and modeling [107] research studies have been conducted on the FFF of PEI and its composites. As an example, Gilmer et al. [108] utilized finite difference models to concurrently assess heat transfer, polymer diffusion (quantified as the degree of healing, Dh), and the emergence of residual stress during FFF of PEI material. Their findings indicated that the stress development in FFF demonstrates periodic fluctuations over time, influenced by temperature profiles. They concluded that variations in deposition and bed temperatures had a limited impact on stress development, whereas layer deposition time, particularly concerning print speed and duration above Tg, exerted significant influence [108].

The printability of high-performance thermoplastic polymers is significantly dependent on their rheological characteristics. Ajinjeru et al. [109] assessed the impact of introducing carbon fiber (CF) into PEI. They observed an increase in the viscosity of the composites (by 2.5× for 20 wt% CF and 3× for 30 wt% CF) and a strengthening of the shear-thinning effect. This noticeable variation in viscosity for PEI composite materials when exposed to varying shear rates and temperatures provides a wide processing range for their use as large-scale FFF feedstock materials. This adaptability can be achieved by adjusting either the screw speed or the processing temperature [109]. In another study conducted by researchers affiliated with NASA [46], the feasibility of manufacturing large-scale complex aircraft parts using Ultem 9085 and Ultem 1000/10 wt% chopped carbon fiber was investigated. The study concluded that the addition of just 10% carbon fiber content significantly increased the viscosity of the materials, making printing more challenging and resulting in higher porosity in the fabricated samples. While the initial Ultem 1000/CF blend showed porosity ranging from 0% to 15%, the filaments produced through extrusion and the Ultem 1000 composite vanes printed via FFF exhibited approximately 25% porosity. This increased porosity can also be attributed to the presence of trapped moisture or outgassing due to degradation at the high printing temperature of 420 °C in the FFF process. In contrast, the Ultem 9085 filament produced parts with 5 to 8% porosity when printed at 375 °C [46].

While incorporating Lunar regolith into PEI can potentially reduce manufacturing costs on the Moon, a research gap exists in exploring its impact on mechanical properties, printing quality, and determining the upper limit for regolith content.

Another promising material for use in space industries and in-space manufacturing is Polyetherketoneketone (PEKK). In comparison to PEEK, PEKK features an additional ketone group in its chemical structure. While PEKK shares many similarities in properties with PEEK, there are a few noteworthy differences. PEKK offers superior thermal stability, boasting a higher glass transition temperature (Tg) at around 162 °C in contrast to PEEK, with a Tg of about 143 °C. Additionally, PEKK has a lower melt viscosity, making it easier to work with during printing. Furthermore, the printing temperature of PEKK is slightly lower than that of PEEK. However, due to PEEK's earlier introduction to the market and its established track record, PEKK has remained somewhat less popular when compared to PEEK [110–112].

While research on the FFF of PEKK is not as extensive as that on PEEK, a body of research is dedicated to the FFF of PEKK and its composites. Rabinowitz et al. [113] employed the Taguchi method to optimize FFF process parameters to maximize the flexural strength of PEKK samples. This study revealed that varying parameters such as raster angle and layer height significantly impacted the flexural strength of carbon fiber-reinforced PEKK. Optimized settings resulted in a flexural strength of 111.3±5.3 MPa and a flexural modulus of 3.5 GPa. Furthermore, post-processing through pressing significantly improved both the samples' flexural strength and flexural modulus [113].

In two papers published by Rashid et al. [114, 115], they investigated the impact of various process parameters, including build orientation, infill pattern, number of contours, and raster angle, on the properties of PEKK samples. Their research revealed that build orientation had the most significant influence on tensile properties (similar to the results obtained in [76] for PEEK), followed by the number of contours, resulting in variations in Young's modulus and elongation at break. Additionally, the studies found that differences in porosity, rather than crystallinity, were responsible for the variations in mechanical properties among the different sample groups, emphasizing the importance of carefully optimizing FFF process parameters for desired material performance. The research findings also highlighted the significant influence of the number of contours on porosity and its substantial impact on a range of mechanical properties. Specifically, increased contours were associated with reduced porosity and improved mechanical and dynamic mechanical properties [114, 115].

One notable project is the Marsha initiative by AI SpaceFactory, aimed at creating sustainable habitats for human habitation on Mars using locally sourced Martian materials. The habitat features a vertical, cylindrical design optimized for Martian conditions, ensuring stability, efficient spatial utilization, and protection against the planet's harsh weather and radiation. Marsha utilizes a biopolymer-basalt composite, facilitating its construction using a form of Fused Filament Fabrication (FFF) process controlled by robotic arms [116–118]. Marsha achieved first place in NASA's 3D-Printed Habitat Challenge, Phase 3 (2019) [119]. Similarly, AI SpaceFactory's Lina project focuses on developing sustainable habitats for the Moon, employing advanced 3D printing technologies akin to those used in the Marsha project for Mars. Lina aims to construct durable, livable structures capable of withstanding the Lunar environment, using Lunar regolith-based materials to reduce dependence on Earth-sourced resources. LINA will be 3D printed using a high-performance mixture of Lunar regolith and Earth-sourced polymer binder, exploring various configurations to optimize between low reliance on off-site polymers and load-bearing capacity. The project uses BP-1 Lunar regolith simulant and employs a unique 60-degree printing angle to create continuous, vaulted roofs. A prepared regolith berm acts as an inclined print bed, supported by reusable metal tiebacks to anchor initial layers and prevent warping during cooling. As construction progresses, a mobile excavator follows to cover LINA with a protective regolith overburden. Unlike Marsha, designed as a freestanding structure on Mars, LINA is designed to expand from a single unit into a cluster, forming a larger, interconnected Lunar outpost. Its orientation provides natural self-shading, utilizing Lunar topography to shield inhabitants from solar and cosmic radiation hazards [120].

Additionally, research has been conducted on printing metals or ceramics using the FFF technique. In this process, after preparing a metallic [66, 121] or ceramic [55, 122] filament that contains a polymeric binder, it is printed using the FFF technique. Subsequently, the as-printed samples (known as green bodies) undergo a polymer removal process, typically referred to as debinding, followed by sintering. Ultimately, this results in metallic or ceramic samples [55]. This method also holds promise for Lunar-based manufacturing, particularly for printing regolith samples. However, if the process is carried out in a Lunar outdoor environment, there will be limitations in the choice of binder polymer due to outgassing requirements [44]. It is worth mentioning that the use of recyclable polymeric binders is advantageous, as it helps reduce the cost of raw materials delivery [123].

All in all, the most crucial problem for Lunar-based FFF is that carbon is very scarce on the Moon (around 142-226 ppm by mass, based on Apollo 11 data [124]), and polymers cannot be considered a material that can be developed on-site. This makes the 3D printing/extrusion of polymer-based materials on the Moon challenging. However, there are some points that make on-site polymer manufacturing important. The first case is when a part is needed on-site urgently, and fabrication and transportation from Earth (lead time) can be lengthy. This necessitates enhancing the capabilities of manufacturing, particularly using FFF, on-site. Second, as discussed above, enabling the fabrication of polymer/regolith composite parts through materials extrusion can make the process considerably more economical by greatly reducing the mass launched from Earth. Lastly, FFF offers great potential for fabrication using repurposed thermoplastics. Therefore, conducting research on this topic is crucial.

Fused Granulate Fabrication Fused Granulate Fabrication (FGF) is an AM technique that utilizes granular materials as the primary feedstock for object fabrication. Sometimes referred to as 'Fused Granular Fabrication,' this method diverges from traditional filament or resin-based approaches by employing granules or pellets composed of various materials, including plastics, metals, or ceramics. In this process, granules are heated to their melting point and then extruded through a nozzle, closely mirroring the fundamental principle of FFF. The extruded material is deposited layer by layer to form the desired object. Figure 1.1 illustrates the conceptual difference between FFF and FGF [1, 125].

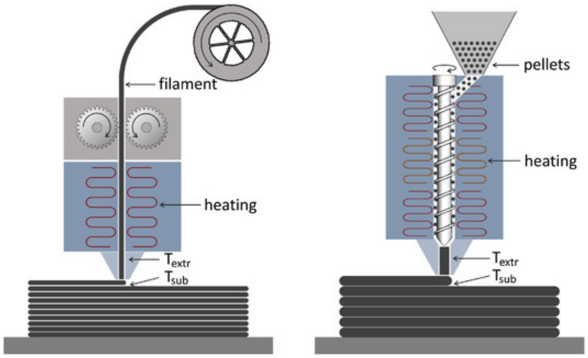

Figure 1.1: Comparison of the concept between Fused Filament Fabrication (FFF), depicted on the left, and Fused Granulate Fabrication (FGF), illustrated on the right, reproduced from [1]. FFF feeds a prefabricated filament through a short heated block, resulting in melting over a limited zone, lower throughput, and reduced material flexibility. In contrast, FGF processes polymer pellets using a heated screw barrel, providing longer residence time, improved melt homogenization, and higher deposition rates, albeit with reduced fine-scale control over the extrusion process.

FGF offers several advantages, including material versatility, simplification of filament manufacturing, and the potential for cost savings through the use of readily available granules instead of specially manufactured filaments. Moreover, when compared to filament-based techniques, FGF typically expedites the fabrication process, enabling the rapid production of large-scale components. FGF can achieve higher throughput in mass production scenarios due to its continuous extrusion process [1, 125].

As indicated in the literature [126], whenever a material undergoes a process involving melting, it can adversely affect its properties, including tensile Young's modulus, strength, and impact strength. This is primarily due to chain scission and crosslinking (when done in the atmosphere) [127]. One significant advantage of FGF over FFF is its potential to eliminate the melting step associated with filament production. This advantage becomes even more pronounced for in-space manufacturing, where recycling becomes necessary due to the high material delivery costs. This capability allows for greater material recycling over multiple cycles.

However, it is important to note that FFF still holds specific advantages over FGF. FFF often delivers higher print resolution and surface quality because it relies on pre-manufactured filaments with consistent properties. Furthermore, FFF 3D printers are typically less complex because they do not require the additional equipment necessary for granulate processing and extrusion [1, 125]. Another issue for FGF arises when attempting to let pellets or other initial material fall naturally through a funnel, as the lower gravity reduces the efficiency of this process.

The choice between FFF and FGF hinges on specific project requirements. FGF excels in scenarios where material flexibility, cost-efficiency, and rapid manufacturing are critical, particularly for large-scale parts. In contrast, FFF is preferred for applications that require higher print quality and simplicity. In contexts such as in-space manufacturing, where energy resources may be limited, the advantages of FFF, with its streamlined complexity and finer resolution, become particularly valuable [1, 125].

As a notable research on FGF using space-grade materials, Martin-Perez et al. [128] investigated the processability of company scrap LMPAEK containing 40% short carbon fiber through FGF, providing a sustainable solution for aircraft structural parts. Similar to PEEK and PEKK, Low-melt Polyaryletherketone (LMPAEK) is a high-performance polymer developed by Victrex from the Polyaryletherketone (PAEK) family. It is designed to exhibit thermal, mechanical, tribological behavior, and chemical resistance similar to PEEK but with a less complex manufacturing process due to its lower melting point [129].

Similar to other fabrication techniques, ISRU is a necessity for space-based FGF. However, ISRU-based FGF has received relatively less attention. Researchers at Polytechnique Montreal conducted a study on FGF using PEI/Lunar regolith simulants under the supervision of the Canadian Space Agency (CSA) [130]. Still, further research needs to be conducted on the FGF of polymer/regolith to assess the real potential of this technique for in-space manufacturing.

Extrusion of Molten Regolith One potential option for in-space additive manufacturing involves extruding molten regolith to achieve the desired shape. This approach is of particular interest because molten regolith/ceramic/glass represents one of the few viable options for extrusion without polymer binders. Although accessing the equipment and energy necessary for regolith melting on the Moon poses challenges, these resources could potentially be obtained from specific candidate metal/oxygen extraction processes that require regolith melting. Metals can be extracted as a by-product of the process. Another possibility is to directly use the molten material created during the oxygen extraction process for additive manufacturing. As an example of existing/ongoing research, Kilncore, a company based in Quebec, Canada, has introduced and patented a technology that combines molten regolith electrolysis and AM, enabling better efficiency than when these processes are carried out separately [131, 132].

Lunar regolith has a wide range of compositions and properties (see Section 1.3.1). Consequently, there is no single, uniform melting point for it. The melting point of Lunar regolith materials can vary depending on their specific composition and the presence of various minerals. Generally, its melting temperature range is 1100 °C to 1380 °C. Above 1380 °C, the regolith is completely molten [133]. Therefore, finding a temperature suitable for printing would be challenging, and a trade-off should be made between the fabricated part's characteristics and energy consumption. Additionally, the presence of various materials in the molten substance can complicate and make it challenging to control the solidification phase.

In a study carried out at NASA's Kennedy Space Center, Mueller et al. [28] melted and extruded BP-1 basalt regolith and JSC-1A Lunar regolith simulant using a robotic arm to explore the potential of extrusion-based additive manufacturing for Lunar-based construction. They conducted an analysis of flexural strength using a 3-point bending test. Their findings revealed that the strength of the samples surpassed that of typical residential concrete and was comparable to certain types of less durable glass materials [134]. Despite these promising results, the researchers concluded that the technology is still in its early stages of development and that further research is necessary to fully realize its potential [28].

This technology holds great promise for in-space manufacturing. One key advantage is its potential for 100% ISRU-based fabrication, providing independence from off-site materials. Additionally, as mentioned, it utilizes the molten regolith already produced for oxygen extraction, which helps energy efficiency. However, compared to AM of regolith with a polymeric binder, this method offers less control and requires significantly more power. All in all, limited research has been conducted on this technology, and it is still in its early stages. Conducting more research and assessing the characteristics of the fabricated components will provide additional evidence to evaluate the true potential of this technology.

1.3.3 Powder Bed Fusion

Powder Bed Fusion (PBF) is a major AM category in which a fine layer of powdered material, evenly distributed across the build platform, is exposed to a high-power energy source, such as a laser beam, electron beam, microwave, or solar radiation to melt and fuse powder particles layer-upon-layer selectively. A schematic representation of the PBF process is depicted in Figure 1.2. PBF is commonly implemented through various methods, including selective laser sintering (SLS), selective laser melting (SLM), electron beam melting (EBM), selective solar light sintering (SSLS), and selective microwave sintering (SMWS). Researchers have found several of these methods applicable to challenging Lunar environments, particularly for printing with Lunar regolith. This technique is also widely used for fabricating polymer parts. However, its greatest potential in the Lunar environment lies in metal printing. By extracting metals from Lunar regolith, this approach could significantly enhance the technique's ability to fabricate locally sourced metal components with high dimensional accuracy and mechanical strength.

Laser Powder Bed Fusion (L-PBF) L-PBF-based technologies, including SLM and SLS, rely on laser energy to fully melt/sinter material particles and fuse them together [20]. These processes

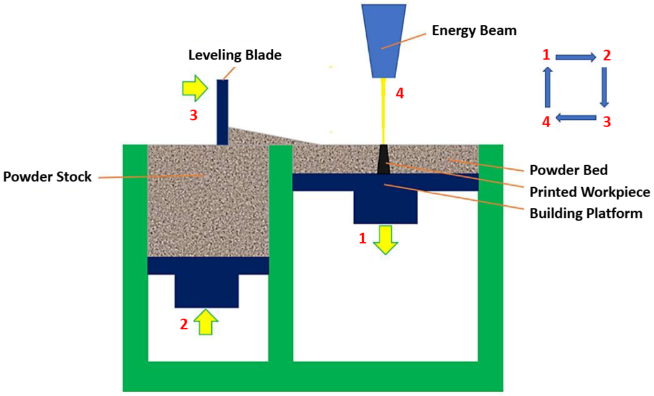

Figure 1.2: Schematic representation of the PBF process, reproduced from [2]. Powder Bed Fusion (PBF) works by repeatedly spreading a thin layer of powder and selectively melting it with an energy source. Each cycle, the build platform lowers, the feed piston rises to supply fresh powder, and the recoater blade spreads a new layer before the next scan. This layer-wise process enables high precision.

are particularly notable for their ability to work with materials with high melting points, such as powdered ceramics and multiphase soil. Thanks to this capability, these methods have been proposed for the direct fabrication of fine geometries from Lunar regolith with no need for additives. Considering that laser processing parameters directly influence the properties and characteristics of the printed materials, researchers have worked to precisely optimize the processing parameters to control and improve the outcome of the print.

Fateri et al. studied the feasibility of laser melting technology for printing Lunar regolith [135, 136]. To minimize particle size variation and ensure uniform energy absorption within the powder bed, JSC-1A regolith simulant was sieved through a 63 µm mesh. Optimal process settings were determined to be 50 W for laser power and a scan speed of 50 mm/s, which yielded acceptable microscopic results with uniform surface properties. The layer thickness was set between 100 µm and 300 µm. They printed various complex geometries at both millimeter and micrometer scales. The authors investigated the morphology and hardness of the manufactured objects using the Berkovich method, which yielded a surface hardness of 1245 HV. The measured surface roughness averaged at Ra = 1.5 µm. They reported promising outcomes in terms of structural integrity, geometrical accuracy, and density for the manufactured parts.

Laser processing parameters were optimized in another research by Goulas et al. [137]. They conducted experiments within an inert argon environment. The as-received JSC-1A regolith simulant was filtered through a 125 µm mesh. Their optimized parameters consisted of a 50 W laser power, a scanning speed of 210 mm/s, a laser beam spot size of 300 µm, and a 210 µm hatching space (with a 35% overlap) on each layer, resulting in a laser energy density of 1.011 J/mm^2. These settings produced macroscopically flawless specimens. Subsequent analysis involved SEM, X-ray fluorescence, and Vickers micro-hardness testing on the laser-processed specimens. The printed material exhibited a relative porosity of 40.8% and a material hardness of 670±11 HV. Notably, they achieved a dimensional accuracy of 99.8%. In another study [138], Goulas et al. documented that an input energy of 0.92 J/mm^2 yielded favorable morphological characteristics and mechanical properties. For this study, they set the laser scanning speed at 320 mm/s, layer thickness at 150 µm, and hatch spacing ranging from 170 to 250 µm to produce configurations with fine features without failures. The printed objects displayed a porosity ranging from 44% to 49%. The authors reported a maximum compressive strength of 4.2±0.1 MPa, an elastic modulus of 287.3±6.6 MPa, and an average hardness value of 657±14 HV. The authors concluded that the achieved strength value is sufficient for manufacturing structures or relevant replacement parts on the Moon, particularly considering the absence of storms. However, the Moon's lower gravity might negatively affect PBF-based printing processes. They also implemented the SLM method to 3D print Martian regolith [139].

The processability of regolith from other Lunar regions has also been studied. In an investigation carried out by Caprio et al. [140], the L-PBF of NU-LHT-2M highlands regolith simulant was analyzed. They investigated the feasibility and limitations of the process and thoroughly examined the optimal base plate and energy conditions. They reported a maximum compressive strength of 31.4 MPa, well above the properties achieved through alternative methods. The corresponding microhardness and porosity were measured at 680 HV and 37%, respectively. These properties were attained using specific process parameters, including a laser power of 50 W and a scan speed of 225 mm/s. The study discussed atmospheric and gravitational conditions through a simplified theoretical framework, analyzing particle settling and free-fall times [140]. However, these findings are purely theoretical and lack experimental validation at this point. Additionally, the study did not assess how these conditions affect the properties and qualities of the print; a more thorough evaluation is necessary. These aspects are fundamental for process stability and print quality due to the Rayleigh and Mie scattering effect [141]. Rayleigh scattering involves the dispersion of the laser beam in multiple directions by fine particles smaller than the laser wavelength, leading to inefficient energy transfer and inconsistent energy absorption in the powder bed. In the presence of atmospheric gases, gas molecules can further contribute to the dispersion of laser beams. Therefore, Rayleigh scattering is minimal in the vacuum environment. Mie scattering, on the other hand, refers to the phenomenon where a laser beam is scattered by suspended particles whose diameters are comparable to the wavelength of the incident laser. The suspended particulate matter comes from particle ejections near the melt pool and vaporized ejecta [141]. The presence of an atmosphere can affect Mie scattering by introducing additional particles like dust, which further disturb the laser beam. Thus, the vacuum conditions on the Moon might mitigate Mie scattering. However, Mie scattering can become more significant in the Moon's low gravity because of the higher concentrations of suspended powder particles. In other laser-based fabrication processes, any step that increases the density of suspended particles, such as the powder deposition step, can increase the Mie effect. For instance, in the Laser Directed Energy Deposition (L-DED) technique, the powder is actively blown from a nozzle, increasing the chances of particles becoming airborne and suspended in the air, thus enhancing the Mie effect. Despite their significance, the scattering effects in laser-based sintering of Lunar regolith have not been addressed in the literature. Caprio et al. studied the vacuum environment and noted substantial particulate outgassing during the fusion of the Lunar regolith simulant. They recommended implementing a strong gas recirculation system to prevent suspended particles from interfering with laser emission [140]. However, such a system adds complexities while in extraterrestrial environments simplicity is preferable. Detailed experiments by Sibille et al. [142] evaluated the strength properties and quality of sintered regolith under vacuum conditions. Their findings indicated that the processing temperature for FJS-1 basalt could be reduced by 100°C to achieve similar densification and compressive strength as in air. For the JSC-1A mare simulant, vacuum-sintered specimens showcased higher compressive strength at lower temperatures compared to those sintered in the air (152 MPa vs. 98 MPa). The sintering temperatures were 1100°C in vacuum and 1125°C in air. This reduction in temperature is attributed to the formation of iron and magnesium oxide layers on mineral grains in air, leading to higher processing temperatures than in vacuum or reduced atmospheres. For NU-LHT-2M Lunar highland regolith, test specimens processed at 1300°C and cooled at 1°C/min were fully sintered with 5.3-5.6% open porosity. In a vacuum, samples with similar porosity were obtained at 1250°C [142].

Mechanical properties have also been reported for L-PBF-printed HIT-L-1 simulant with L-PBF parameters of a 75 W laser power, a 4 mm spot diameter, a 1 mm/s scan speed, a 2 mm hatch spacing, and a 1.2 mm layer thickness [143]. These settings correspond to a volumetric energy density in the range of 3.5 to 4.3 J/mm^3. The glass-ceramics were formed at 823°C during thermal post-treatment, and polycrystalline glass-ceramics with better mechanical properties were achieved at 1100°C. The average compressive strength, fracture toughness, and Vickers hardness were measured at 50.71 MPa, 1.49 MPa.m$^{0.5}$, and 897.91 HV, respectively. These enhanced mechanical properties, compared to those reported by Goulas et al. [137, 138], are attributed to the higher energy input, facilitating sufficient melting, improved fusion, and inter-layer bonding. This results in enhanced densification and overall improved mechanical properties. The relative porosity of the print was determined to be 40% [143]. While Wang et al. were successful in 3D printing Lunar regolith with favorable mechanical characteristics, their proposed processing method raises concerns regarding its energy consumption and sustainability in the Lunar environment. Additionally, their use of a scan speed as slow as 1 mm/s makes the printing process exceedingly time-consuming.

Laser-based AM technology is capable of printing Lunar soil without any additives. Researchers were able to achieve high microhardness [135–138], as well as compressive strength [140, 143] for the printed regolith simulant. However, these prints are characterized by remarkably high porosity, primarily attributed to the high melting point of soil minerals that do not fully liquefy during laser processing [2, 137]. The low absorption coefficient of the soil and the problematic absorption of laser energy further contribute to this challenge, resulting in improper flowability and fluidity [2]. Moreover, the printed regolith is brittle due to the oxide ceramic elements it contains [137, 144]. The inclusion of metallic particles demonstrated a considerable enhancement in the quality and characteristics of the final product [2, 145].

In this regard, using the SLM method, Liao et al. [145] incorporated aluminum alloy into the Lunar regolith and produced a Lunar regolith-AlSi10Mg composite. The CAS-1 Lunar regolith, sieved through a 200-mesh screen, was mixed with spherical AlSi10Mg powder with a mean particle size of $33.1\mu m$ in a 1:1 weight ratio. The process parameters were set as follows: laser power of 200 W, scanning speed up to 800 mm/s, layer thickness of $20\mu m$, and a hatching space of 0.1 or 0.12 mm. The experiments were conducted within an inert argon gas atmosphere to prevent oxidation. Based on microstructure analysis, two types of defects were observed in the printed composites. Pore defects were predominant at low scan speeds, while lack-of-fusion defects occurred at high scan speeds, with other process parameters held constant. The maximum relative density of the fabricated test specimens reached 92.5% for an 800 mm/s scan speed and a 0.12 mm hatching space. Correspondingly, compressive strength testing of the Lunar regolith-AlSi10Mg composite yielded a strength of 264 MPa. During the process, various metallurgical reactions were observed in the molten pool, leading to the loss of Lunar regolith. Aluminum reduced SiO_2, FeO, and TiO_2 in simulant Lunar regolith, while Al_2O_3 was transformed into gaseous Al_2O at high temperatures.

L-PBF processes have also found applications for larger-scale projects on the Moon. Recently, a high-power CO_2 laser was implemented for paving on the Moon and the creation of dust-free roads, with a maximum laser spot diameter of 100 mm [146]. Large samples, each 250 mm×250 mm with interlocking capabilities, were produced by melting the EAC-1A simulant directly on the powder bed using the laser. The process employed laser parameters of 3 kW and a speed of 5 mm/min in a single-layer fabrication approach. These printed samples can cover large areas of Lunar soil, forming roads and launchpads. The manufactured samples were analyzed for their mineralogical composition, internal structure, and mechanical properties. To ensure the printed samples could support the weight of heavy exploration equipment, their compressive strength was tested and compared to solar-sintered specimens from the RegoLight project [73]. Compressive strength was measured using 10 mm×10 mm×10 mm cubic samples. The results showed a compressive strength range of 56.19 to 216.29 MPa, with an average of 93.97 MPa, approximately 50 times higher than the 2.49 MPa achieved in the solar-sintered project [73]. However, a significant standard deviation of 55.88 MPa was observed, likely due to internal defects such as porosity and micro-cracks within the samples [146].

ICON and SEArch+ have developed design schematics with concepts for surface-site deployment, construction sequencing, and structural design for large-scale infrastructures for permanent

Lunar settlements [147]. These designs include landing pads, roadways, habitats, shelters, and blast shields, and their double-protective ”Lunar Lantern,” all constructed using Lunar regolith and enabled by additive construction technologies. They have investigated various extrusion deposition and sintered-based additive methods. In collaboration with NASA KSC, ICON developed the Laser Vitreous Multi-Material (VMX) transformation process. This process autonomously deposits, compacts, and selectively preheats and sinters thin layers of prefiltered Lunar highland regolith. The system operates with 6-DOF robotic arms inside a Lunar surface simulation chamber that measures 6.4 m ×8.5 m in area with a bed depth of 0.9 meters [148]. The Laser VMX vacuum-produced material showcased high performance, with compressive strengths of 344.7 MPa at 25°C and 251.66 MPa after one year of Lunar thermal vacuum (TVAC) cycles. Its flexural strength was 37.92 MPa, and the thermal expansion coefficient was 3.6×10^{-6} °C^{-1} over a temperature range from -150°C to 50°C in a vacuum. Simulations of the Laser VMX process are conducted to predict how the laboratory results will scale to actual Lunar surface conditions.

The feasibility of using the SLS method on the Moon to 3D print Lunar regolith has also been studied by Xu et al. [149]. They conducted experiments to print CLRS-2 Lunar highlands regolith powder and ilmenite powder and investigated the impact of laser manufacturing parameters on the properties of the printed Lunar regolith. More pores were present in the printed CLRS-2 specimens compared to the ilmenite printed specimens, resulting in inferior mechanical properties for CLRS-2. To enhance these properties, CLRS-2 powder and ilmenite powder were pre-pressed at pressures of 10 MPa and 40 MPa to become denser. This preprocessing step reduced the porosity of the laser-sintered CLRS-2 but had no effect on ilmenite. Laser-sintered materials that underwent 10 MPa pre-pressurization displayed much smoother surfaces and fewer porosities than samples without pre-pressurization.

The substantial energy density required for laser-based processes poses challenges for Lunar operations, given that energy production and storage remain issues in extraterrestrial settings. The electrical energy required for laser-based additive manufacturing is a major concern on the Moon. To enhance sustainability for Lunar operations, it is essential to rely on in situ resources for electricity generation to support laser-based additive manufacturing. Solar light, an abundant renewable resource, can be converted into electricity through photovoltaic (PV) cells, which are a standard method for energy conversion. In situ fabrication of solar PV cells has been proposed, as more than 90% of solar cell materials are available on the Moon (e.g., Si, Fe, $\mathrm{TiO_2}$, Ca, and Al) [150, 151]. Manufactured solar cells consist of a Lunar glass substrate, a doped silicon layer between aluminum electrodes, and a $\mathrm{TiO_2}$ antireflective coating. Single-crystal thin-film Si solar cells can potentially achieve efficiencies of around 25%, though this necessitates the use of advanced deposition and surface coating technologies [152]. However, in situ fabrication of solar cells from extraterrestrial sources presents difficulties due to limited controllability, leading to efficiencies as low as 5–10% [150, 153]. Moreover, these manufactured cells experience long-term degradation from radiation exposure and the high temperatures of the Lunar day [154], which further reduces their energy conversion efficiency by an additional 30%. An alternative solar-electric energy generation method proposed by Ellery [150] involves leveraging Lunar resources for solar power production using a Fresnel lens-thermionic conversion system. This system can achieve conversion efficiencies around 15–20%, with the potential for higher efficiencies through advanced techniques and improvements. Therefore, although solar light is abundant, the conversion of this energy into electricity for laser operations presents certain challenges, making laser-based additive manufacturing highly inefficient in the Lunar setting.

Although substantial research has been conducted in this area, the primary challenge with printing Lunar regolith is its low optical absorption due to its ceramic composition, resulting in fabricated parts with poor mechanical strength. While preprocessing techniques, such as mixing locally extracted metallic particles with regolith, can enhance laser absorption, the technique's true potential lies in metal fabrication. Since transporting metals to the Moon is extremely costly, extracting metals from Lunar regolith offers a viable solution.

For instance, Ellery et al. [155] explored the use of LPBF with titanium (Ti) extracted from Lunar regolith via the Metalysis Fray Farthing Chen (FFC) process. A significant achievement of their study was the successful extraction of Ti powder from rutile using the FFC method, which was then utilized to fabricate test structures through LPBF. The high energy efficiency of these processes makes them highly suitable for Lunar-based ISRU [155]. The combination of metal extraction from regolith and subsequent LPBF offers nearly 100% ISRU-based fabrication of robust, complex parts, making it highly promising for the future of LBMC.

Given the extensive literature, including textbooks and review papers, on terrestrial metal LPBF, delving into further detail here would add limited value (Please refer to [156]). However, there is very limited literature on adapting metal LPBF for the Lunar environment, highlighting the need for further research to fully tailor this technique for Lunar applications.

EB-PBF Electron-beam PBF (EB-PBF), commonly known as EBM, replaces the laser with an electron beam to selectively melt and fuse powdered materials. EB-PBF operates in a vacuum [157], which is particularly well-suited for applications in space environments. While laser-based printing often results in materials with high porosity due to its sensitivity to the reflectivity of the processed material, impacting the overall mechanical properties of the final product [2, 137], EBM is less influenced by the absorption characteristics of the material. However, EBM machines are typically more complex and expensive to operate and maintain, making them less accessible for Lunar missions. It also comes with a limitation that prevents its widespread application for LBMC: its applicability is limited to metals and is less effective for non-metallic materials [158, 159]. This limitation can be attributed to the fundamental differences in how electrons interact with various types of materials. In response to this limitation, Howell and colleagues [158] incorporated aluminum as a binder material to enhance the ductility of the material and improve its fluidity within the melt pool. They successfully printed Lunar soil simulants (JSC-1 and LHT-1M) aluminum composites via the EBM method. There is no information available about the mechanical properties of their prints. Despite the potential shown by Howell et al., there has been a notable absence of subsequent research on the topic. This gap in research may stem from the limitations of EB-PBF technology in processing non-metallic materials like regolith. However, this technique holds significant potential for fabricating metallic components using metals extracted from Lunar regolith. Another issue is the interaction of electrons with powder particles, which can lead to the emission of powders, particularly in the microgravity Lunar environment. Given these limitations and challenges, there exists a research gap that must be addressed before this process can be used on the Moon.

SS-PBF Solar sintering PBF (SS-PBF), also known as SSLS, harnesses concentrated sunlight to fuse powdered materials. Taking into account the full potential of resources present on the Lunar surface, including solar light and Lunar regolith, while avoiding the use of additive binders in methods like binder jetting or direct ink writing, and direct sintering without the need for a laser or EB source, like those used in L-PBF or EB-PBF methods, represents a viable approach to on-site manufacturing, thereby reducing reliance on Earth-supplied materials and technology.

The solar sintering of Lunar regolith was initially limited to sintering a thin layer of Lunar regolith to fabricate launchpads, aiming for surface stabilization and dust mitigation [160–162] during take-off and landing of missions, which can cause problems for nearby infrastructures and human activities on the Moon [163–166]. Hintze et al. [167] constructed a $1\ \mathrm{m}^2$ solar concentrator, comprising a Fresnel lens installed on a frame designed to track the sun and collect solar energy for sintering JSC-1 regolith simulant. The highest measured temperature produced by the concentrator was 1350°C, well above the temperature required to melt the regolith simulant. Their work also discussed the physical and mechanical assessments, including load strength and abrasion resistance, both in the field and for the laboratory-prepared sintered test specimens. Their findings showcased the potential of the proposed method, which uses a simple and cost-effective technology for sintering Lunar regolith and preparing large launch pads.

Meurisse et al. [168] and Fateri et al. [73], in their collaborative works, demonstrated the feasibility of printing basic geometries through selective solar sintering of Lunar regolith using mirror-based solar collectors. Their setup included artificial sunlight-Xenon lamps and a water-cooled mirror inclined to 45° onto which the horizontal irradiated light was projected to adjust the light beam orientation and direct it vertically onto the build platform. These two Xenon lamps collectively delivered a concentrated light density of $1.2\,\mathrm{MW/m}^2$ onto a 20 mm focal point. The lamps were calibrated to obtain a sharp beam with the smallest focal point. The as-received JSC-2A powder, resembling Lunar mare soil, was dispersed in 100μm-thick layers and sintered layer upon layer through the selective solar sintering process. Tests were carried out under both ambient conditions and in a vacuum. Bricks were printed with a scanning speed of 47 mm/s, a layer thickness of 100μm, a hatch spacing of 15 mm, and a focal spot of 12 mm in the ambient condition. However, these printing parameters led to a molten state for the layers and a porous brittle medium for the print in the vacuum environment. The processing parameters were subsequently adjusted for the vacuum condition and set at $1.0\,\mathrm{MW/m^2}$ for lamp intensity and a scanning speed of 65 mm/s. Morphological analysis of the printed cubes revealed the presence of open pores, some of which measured up to 0.60 mm in size, indicating weak interlayer bonding. Additionally, closed porosity with dimensions of up to 0.45 mm was observed due to the outgassing of minerals at the melting temperature. Solar sintered materials under ambient atmosphere were characterized by compressive strength of 2.49 MPa and Young's modulus of 0.21 GPa. For a given set of sintering parameters, smaller sintered components displayed greater strength compared to larger ones. The assessment of vacuum-sintered parts was omitted. It was speculated that the absence of an atmosphere might adversely affect the sintering process due to a substantial release of gases from the highly molten material, causing the fracture of the initial sintered layers or resulting in uneven surface textures. On the other hand, the vacuum environment might enhance mechanical properties by preventing the oxidation of Lunar minerals and facilitating a more uniform distribution of heat within the sintered material, improving material strength and reducing thermal stresses.

Outward Technologies utilized concentrated solar energy to power powder bed fusion (PBF) and fused deposition modeling (FDM) processes [169]. These methods were used to fabricate volumes of 1 m × 0.3 m × 0.1 m and various lab-scale components from CSM-LHT-1 Lunar highlands regolith simulant. The components included rover parts and structural elements like trusses for bridges, towers, and ramps. The sintered specimens achieved 95% density. The fused regolith demonstrated a compressive strength of 25 MPa and Young's modulus of 10.3 GPa, comparable to M25 concrete. Additionally, its stress-strain curve revealed 20% more strain at failure and greater toughness than M25 concrete. The flexural strength of the PBF-printed specimens was measured at 3.5 MPa. This solar-powered PBF process could be suitable for large-scale manufacturing, potentially replacing concrete-type infrastructure on the Moon. However, the solar sintering AM presents certain geometric limitations due to the low precision of its beam focus, making it inappropriate for creating highly complex designs with fine details, acute angles, and smooth surface finish. As a bulk method, solar sintering is a simple and cost-effective technology, ideal for sintering Lunar regolith to prepare large launchpads for dust-free stabilized road and landing pads, as well as for fabricating less detailed parts [160–162, 167]. In contrast, laser-based and electron beam sintering technologies use high-powered energy beams with precise energy delivery in controlled environments, ensuring consistent quality and enabling intricate details with fine resolutions [135–137]. Notably, laser-based additive manufacturing methods have showcased a promising dimensional accuracy of 99.8% [137]. Long sintering processes can also be challenging, particularly with the sintered parts' thermal stresses. Slow scanning speed and rapid cooling resulted in stress buildup, causing the sintered part to warp during the process. The most effective strategy involved alternating scanning of successive layers along the length and width of the part and sintering a contour before each layer to minimize warping of the part edges.

MWS-PBF The Microwave sintering PBF, also known as SMWS, is a method that involves subjecting powdered material to controlled microwave radiation to induce heating and initiate the sintering process. Microwave heating is currently recognized as a more practical approach for constructing structures and extracting resources on the Moon compared to solar [73, 168] and laser sintering [136] methodologies. This preference is due to the volumetric heating characteristic of microwave processes, which consumes approximately 23% less energy than laser sintering and in shorter fabrication times [170]. Microwave radiation can penetrate the material deeply (up to 65 cm), making it an efficient method for subsurface heating [171, 172]. This ensures a more consistent sintering process and minimal temperature gradients across the targeted material, ultimately improving the mechanical properties of the sintered material.

Based on successful microwave sintering of Lunar regolith in previous studies [172–178], the SMWS method was suggested for on-site additive manufacturing on the Moon. NASA researchers in [179, 180] developed a 3D microwave print head facility using a 2.45 GHz wave generator to explore the feasibility of additive manufacturing using Lunar and Martian simulants. This involved integrating a temperature-resistant quartz tube vertically through the cavity. The JSC-2A simulant was gradually fed through the tube and heated beyond its melting point to enhance the flow rate. The resulting melted simulant exited the tube to be selectively placed onto a substrate to form walls or pave a road. The researchers understood how to control the sintering and melting of the target material subjected to microwave radiation and determined optimal operating parameters for large-scale manufacturing. Various operating parameters such as power, flow rate, tube diameter, and location were adjusted based on sample size and the estimated temperature dependence of the dielectric constant to optimize performance. Evaluation extended to Lunar highland and mare simulants as well as Mars soil simulants. To verify whether the enhanced heating effect was associated with a chemical interaction with oxygen in the surrounding atmosphere, measurements were repeated on a Lunar JSC-2A simulant with a nitrogen atmosphere surrounding the cavity, yielding consistent results. Consequently, the remaining studies were then performed in Earth's atmosphere. To establish a suitable construction procedure, it is essential to ensure that regolith simulants' particle size and shape distribution align closely with those of authentic Lunar regolith [181]. A thorough examination of the necessity for nanophase iron in Lunar simulants is also advised.

Although promising for additive manufacturing on the Moon, microwave sintering takes a different path in the fabrication process compared to laser and solar sintering methodologies, which are typically used for layerwise sintering and material addition to building up geometries. This divergence is attributed to the challenges associated with fine-tuning and controlling process parameters to achieve the desired material properties and print resolution. The relative lack of attention to this specific method for Lunar additive manufacturing could hold potential for future research and development. Microwave radiation's deep penetration into materials allows for processing within the volume, ensuring an even distribution of heat throughout the substance. Reduced temperature gradients throughout the sintered material minimize the risk of fracture and pore formations. This characteristic makes microwave heating a promising method for thermal post-treatment to alter the microstructure and mechanical properties of pre-sintered materials [182, 183].

1.4 Gaps and positioning of this work

While space agencies such as NASA [87] and academic institutions continue active research in the field of in-space manufacturing, a notable gap persists at the intersection of in-situ resource utilization (ISRU) and fused filament fabrication (FFF). In an ISRU-oriented FFF approach, locally available feedstocks, such as Lunar regolith, are combined with high-performance, space-grade polymeric binders. The goal is twofold: to reduce the mass and cost associated with transporting raw materials from Earth and to enable, where feasible, improved or tailored properties in the final parts.

This research addresses the fabrication of structures intended to operate in the demanding Lunar environment while meeting requirements set by space agencies, including constraints on vacuum outgassing and tolerance to extreme thermal cycling. Achieving these targets requires process routes that maximize on-site resource utilization and minimize reliance on imported constituents, which are logistically and economically expensive to deliver from Earth.

The findings of this thesis carry direct implications for advancing additive manufacturing (AM) capabilities in Lunar settings and, more broadly, for in-space production. By demonstrating the use of PEEK within an ISRU-compatible FFF framework, this work lays the groundwork for more robust, efficient, and maintainable manufacturing pathways that can support long-duration missions and the progressive build-out of Lunar infrastructure.

1.5 Thesis statement

Lunar regolith can be added to space-grade PEEK as a filler to reduce the cost of transporting materials from Earth for in-space additive manufacturing. Below a threshold percentage, it results in a gradual and acceptable decline in strength, while actually reducing warping and improving interlayer bonding to a point. At a critical threshold, however, high melt viscosity causes large defects and reduced interlayer bonding, and a subsequent dramatic decrease in part strength.

1.6 Potential applications of PEEK/regolith composites in Lunar surface operations

The mechanical performance, thermal stability, printability, and ISRU compatibility demonstrated in this thesis position PEEK/regolith composites as promising candidates for a range of structural, functional, and environmental protection components for sustained Lunar operations. These applications primarily target small to medium engineering parts suitable for in-space manufacturing platforms and robotic fabrication systems.

1.6.1 Structural and Functional Parts

PEEK/regolith composites can support low to moderate load-bearing functions while providing abrasion resistance, thermal stability, and acceptable dimensional accuracy. Representative applications include

- **Rover body components:** panels, housings, sensor mounts, dust-shielding covers, and thermal or radiation shielding tiles.
- **Habitat interior hardware:** brackets, cable trays, equipment mounts, and small structural frames for modular layouts.
- **ISRU system parts:** hoppers, chutes, regolith-handling linings, fixtures, and support frames for material preprocessing and transport.

1.6.2 Construction and Assembly Uses

The favorable printability and on-demand fabrication capability of PEEK/regolith feedstocks enable their use in construction and assembly tasks, for example

- **Interlocking blocks and connectors** for joining sintered-regolith elements or attaching polymer components to regolith-based structures.
- **Formwork and molds** for cast or sintered regolith architectures, where the composite provides lightweight, thermally stable tooling.
- **Repair parts and adapters** for on-demand replacement of damaged components without requiring Earth resupply.

1.6.3 Protection and Environmental Functions

The combination of stiffness, toughness, and thermal stability also makes these composites suitable for protective roles:

- **Sacrificial dust or micrometeoroid skins** placed over vulnerable surfaces to mitigate erosion and impact damage.

- **Locally thickened composite panels** for enhanced shielding around sensitive electronics bays or crew-adjacent areas.
- **Wear-resistant liners** in dust-exposed interfaces within mechanisms or ISRU hardware.

1.7 Past and Forthcoming Publications

This proposal contains research that has either already been published or is planned for publication in the following sources:

In preparation:

- Azami, Mohammad, Rene Lam, Sagar Patel, Xavier Walls, Tomisin Oluwajuyigbe, Alexandra Darroch, Krzysztof Skonieczny, Mihaela Vlasea, and Madison Feehan. ”Comparative Investigation of Laser Powder Bed Fusion of Lunar Regolith Simulant and Its Composite with Invar 36.” Manuscript in preparation (2025).

Preprints:

- Azami, Mohammad, Pierre-Lucas Aubin-Fournier, Mehdi Hojjati, and Krzysztof Skonieczny. ”Additive Manufacturing of PEEK/Lunar Regolith Composites for Sustainable Lunar Manufacturing.” arXiv preprint arXiv:2508.00894 (2025).

Journal papers:

- Malekpour, Farshad, Marjan Abdali, Krzysztof Skonieczny, Mohammad Azami, and Mehdi Hojjati. ”Sustainable Lunar Additive Manufacturing of High Regolith-Loaded PEKK Composites for Space Infrastructure.” Composites Part B: Engineering 310 (2026): 113176.
- Azami, Mohammad, Zahra Kazemi, Sare Moazen, Martine Dubé, Marie-Josée Potvin, and Krzysztof Skonieczny. ”A comprehensive review of Lunar-based manufacturing and construction.” Progress in Aerospace Sciences 150 (2024): 101045.
- Azami, Mohammad, Pierre-Lucas Aubin-Fournier, and Krzysztof Skonieczny. ”Enhancing economical Lunar-based manufacturing by incorporating Lunar regolith into polyether–ether–ketone

(PEEK): material development, additive manufacturing, and characterization.” Progress in Additive Manufacturing (2025): 1-7.

Conference papers:

- Azami, Mohammad, Pierre-Lucas Aubin Fournier, and Krzysztof Skonieczny. ”Additive manufacturing of polyether ether ketone (PEEK)/Lunar regolith composites via fused filament fabrication.” In Earth and Space 2024: Engineering for Extreme Environments, pp. 976-986. 2024.

Oral/poster presentations (presenter bolded):

- Oral presentation: ”Toward adapting mobile 3D printing to metals and regolith,” HI-AM Conference, 2022, **Mohammad Azami**, Pierre-Lucas Aubin-Fournier, Krzysztof Skonieczny
- Oral presentation (Online): ”Toward Mobile 3D Printing of Lunar Regolith via Simultaneous Localization and Additive Manufacturing,” ASME IMECE, 2022, **Mohammad Azami**, Pierre-Lucas Aubin-Fournier, Krzysztof Skonieczny
- Oral presentation: ”Toward Mobile 3D Printing of Lunar Regolith through Simultaneous Localization and Additive Manufacturing,” CASI ASTRO, 2022, **Mohammad Azami**, Pierre-Lucas Aubin-Fournier, Krzysztof Skonieczny
- Poster presentation: ”Robotic 3D printing of Lunar Regolith/Polymer Composite by Simultaneous Localization and Additive Manufacturing,” HI-AM Conference, 2023, **Mohammad Azami**, Pierre-Lucas Aubin-Fournier, Krzysztof Skonieczny
- Oral presentation: ”Robotic 3D Printing of Lunar Regolith/polymer Composite Through Simultaneous Localization and Additive Manufacturing,” ASTM ICAM, 2023, **Mohammad Azami**, Pierre-Lucas Aubin-Fournier, Krzysztof Skonieczny
- Oral presentation ”Robotic 3D printing of Lunar regolith/PEEK large-scale parts through simultaneous localization and additive manufacturing (SLAAM),” ASCE Earth & Space, 2024, Mohammad Azami, Pierre-Lucas Aubin-Fournier, **Krzysztof Skonieczny**

- Oral presentation ”Additive manufacturing of polyether ether ketone (PEEK)/ Lunar regolith composites through fused filament fabrication,” 35th Canadian Materials Science Conference (CMSC), 2024, **Mohammad Azami**, Pierre-Lucas Aubin-Fournier, Krzysztof Skonieczny
- Oral presentation ”Lunar-based Manufacturing and Construction: A Comprehensive Review,” CASI ASTRO, 2024, **Mohammad Azami**, Zahra Kazemi, Sare Moazen, Martine Dubé, Marie-Josée Potvin, Krzysztof Skonieczny
- Oral presentation ”In-Space Manufacturing: Developing Lunar Infrastructure with Robotic Additive Manufacturing and In-Situ Resources,” Formnext, 2024, **Mohammad Azami**, Pierre-Lucas Aubin-Fournier, Krzysztof Skonieczny
- Keynote presentation ”Advancing Lunar Manufacturing and Construction: Leveraging In-Situ Resources and Additive Manufacturing for Sustainable Space Exploration,” 36th Canadian Materials Science Conference (CMSC), 2025, **Mohammad Azami**, Krzysztof Skonieczny

1.8 Outline

The remainder of the thesis is as follows: **Chapter 1** introduces the problem context and motivation for Lunar-based manufacturing, reviews prior work on Lunar regolith and additive manufacturing modalities (with emphasis on MEX/FFF and PBF), identifies gaps, and states the objectives; **Chapter 2** (Phase I) demonstrates initial feasibility of FFF with PEEK–regolith composites, describing materials, fabrication, density, tensile behavior, and microstructural observations; **Chapter 3** (Phase II) develops composition–property relationships for PEEK/LRS (0–50 wt%), including annealing effects, DSC, density/porosity, mechanical performance, and microstructure improvements; **Chapter 4** (Phase III) constructs finite-element models (homogenized and defect-aware RVEs) to explain stiffness trends and the modulus drop at high regolith loadings; **Chapter 5** (Phase IV) assesses LPBF feasibility for regolith-based materials (and a regolith–Invar blend), reporting powder attributes, printing observations, and micro-CT insights to distill processability lessons; finally, **Chapter 6** concludes the work, synthesizes key findings, and outlines prioritized directions for future research and Lunar deployment.

Chapter 2

Phase I: Initial Demonstration of Additive Manufacturing with PEEK–Regolith Composites

This chapter is based on, and in parts reproduces with minor editorial changes, the following published work:
Azami, M., Aubin-Fournier, P.-L., & Skonieczny, K. (2025). Enhancing economical Lunar-based manufacturing by incorporating Lunar regolith into polyether–ether–ketone (PEEK): material development, additive manufacturing, and characterization. *Progress in Additive Manufacturing*, 1–7. doi:10.1007/s40964-024-00934-0.

2.1 Motivation

NASA's Artemis Program is motivating future Lunar settlement and resource utilization. In-space manufacturing (ISM), particularly Lunar-based manufacturing and construction (LBMC), is crucial for extending human exploration beyond Earth [49]. Additive manufacturing (AM) offers great promise for ISM. Materials extrusion (MEX), and more particularly fused filament fabrication (FFF), stands out as one of the most commonly used AM techniques for creating objects with thermoplastic polymer matrices [184]. Utilizing thermoplastics gives FFF a significant edge over techniques employing thermosets due to their recyclability [24]. Furthermore, FFF is increasingly recognized as one of the most cost-effective AM methods, characterized by lower energy requirements, reduced material wastage, process simplicity, and efficient fabrication times [22, 41, 76–78]. Its capability to perform well in low-gravity or zero-gravity conditions [31, 32] positions FFF as a promising approach for LBMC.

Polyether ether ketone (PEEK) is a high-performance, space-grade, recyclable thermoplastic that can be 3D-printed using FFF, making it particularly intriguing for LBMC [41, 185]. However, transporting materials to space comes at great expense. In-Situ Resource Utilization (ISRU) involves using local resources at mission sites, rather than solely relying on off-site supplies [186]. Lunar regolith, abundant on the Moon, presents a significant advantage as a raw material for LBMC [26]. Despite various studies investigating the feasibility of using regolith for LBMC [26], there is a literature gap concerning ISRU-based FFF. This method entails incorporating Lunar regolith into a space-grade binder to reduce the costs of launching raw materials. While polymer/regolith composites are not made from exclusively in-situ materials, recycling can further reduce the amount of polymer required from Earth [24].

This phase demonstrates the feasibility of FFF to produce PEEK–LRS composites, using PEEK as the binder and regolith as the filler. Pulverized PEEK and regolith blend, in a 7:3 weight ratio, is processed into filaments with a twin-screw extruder. Samples are printed using an FFF machine with a heated chamber and undergo simultaneous annealing. Pure PEEK samples are also made for comparison. Investigations evaluate density, mechanical properties, and microstructure. These findings have significant implications for advancing AM capabilities in Lunar environments and

ISM.

2.2 Materials and Methods

2.2.1 Filament making

PEEK pellets (90G, Victrex, United Kingdom) are ground using a 254 mm Lab pulverizer (Orenda, Canada) to achieve a particle size of approximately $150\,\mu\text{m}$. Subsequently, the pulverized PEEK is pre-mixed with $30\,\text{wt}\%$ ($18\,\text{vol}\%$) of regolith using as-received Lunar regolith simulant (LMS-1D, Exolith, United States), with a particle size range of $< 0.04 - 32\,\mu\text{m}$, mean particle size of $7\,\mu\text{m}$, and grain density of $2.92\,\text{g/cm}^3$. This simulant, designed to mimic Lunar mare dust, was chosen for its fine particle size distribution, which is crucial for both the mechanical properties and printability of the composite. Finer particles promote a more uniform dispersion within the polymer matrix, reducing weak points and minimizing the risk of mechanical failure caused by stress concentration [187]. Given the limitations of the current equipment, the maximum concentration achievable with the current setup is 30 wt%. Despite differences in some characteristics between real Lunar regolith dust (which is not available for incorporation into composites at this point) and LMS-1D, particularly in surface morphology (regolith can be highly irregular), particle size distribution is the prime consideration when using the simulant as a filler. The composite 'PEEK/LRS30' powder is then fed into a parallel twin-screw extruder (Process 11, Thermo Scientific™, Germany) operating at 380 °C and a rotary speed of 100 rpm to make filament. For comparison, all subsequent steps are also conducted for pure PEEK, using commercial filament (PEEK K10, Kexcelled, China).

2.2.2 Sample preparation

A high-temperature FFF AM machine (PEEK 300, CreatBot, China) was employed for printing. To enhance print quality and prevent warping, we discovered that printing on top of a raft combined with using Nano Polymer Print Adhesive (Vision Miner, USA) on the bed yielded the best results. To enhance the crystallization of the samples and mitigate thermal stresses, the printer's simultaneous annealing feature (Direct Annealing System by CreatBot) was activated for all samples, set at 420 °C, eliminating post-process annealing. The printer's chamber temperature was adjusted to

120 °C. Printing parameters for all samples were refined to ensure improved printability and the absence of visible defects. These parameters included nozzle and bed temperatures of 420 °C and 180 °C, respectively, a layer thickness of 250 μm, and a print speed of 7.5 mm/s. To assess reproducibility, three samples of each composition were printed. For a smoother surface finish, all samples underwent ironing using the UltiMaker Cura printing software's ironing feature.

2.2.3 Tensile examination

Tensile testing followed the guidelines outlined in the ISO 527 standard. A 5000 N machine (Hoskin Scientific, Canada) was utilized, with the test conducted at a tensile speed of 2 mm/min.

2.2.4 Density assessment

The density of both filaments and printed samples was examined using Archimedean density analysis. This analysis utilized a density determination kit (YDK02MS, Sartorius, Germany) and water at 22 °C.

2.2.5 Micrography

Microstructural analysis was performed on both filaments and samples using a scanning electron microscope (SEM, S-3400N, Hitachi, Japan). Polished cross-sections of the samples were examined, and an energy-dispersive X-ray spectrometer (EDS) was employed to analyze their elemental composition. EDS maps were also generated. For EDS mapping, instead of analyzing just a few isolated points, a broad region was investigated to ensure a comprehensive elemental analysis. The EDS system continuously collected signals, which were processed by the software to produce detailed maps illustrating the distribution of each element across the region.

2.3 Results and Discussion

2.3.1 Fabrication

Despite the challenges associated with elevated melt viscosity after incorporating regolith (similar to those reported by Chuang et al. [46]), we successfully produced a PEEK/LRS30 filament with consistent color, surface quality, and diameter. This achievement was made possible through the careful selection of a high-shear twin-screw extruder, optimization of a pre-mixing strategy, and precise adjustments to feeding and extrusion parameters (as mentioned in Section 2.2.1). While increasing the extrusion temperature can reduce melt viscosity to some extent, it must be managed carefully to prevent material degradation, as highlighted by Zanjanijam et al. [41]. After filament preparation, three samples of each composition were fabricated under identical conditions. Samples showing poor bed adhesion, warpage, visible cracks, or significant porosity were excluded from further analysis. The as-printed samples are shown in Figure 2.1. The process demonstrated acceptable reproducibility, as evidenced by visual assessments, tensile testing, density measurements, microstructural analysis, and dimensional accuracy.

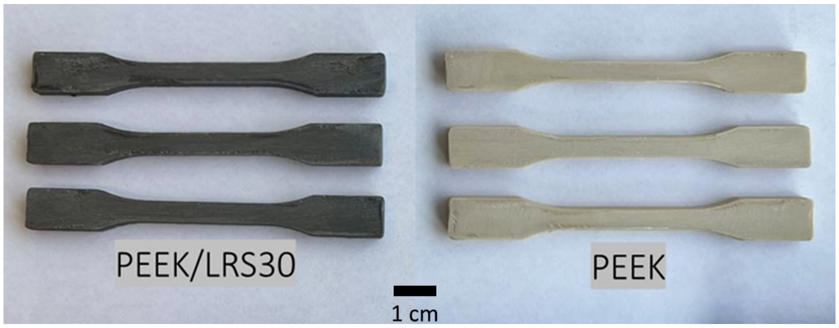

Figure 2.1: Tensile specimens printed from pure PEEK and PEEK/LRS30, with three samples fabricated for each composition to assess printing reproducibility. The regolith-filled specimens appear darker and slightly rougher, while both materials retain similar geometry and dimensional consistency.

2.3.2 Impact of ironing on surface finish quality

The impact of ironing and sanding on the surface finish quality of both PEEK and PEEK/LRS30 samples was found to be significant. Figure 2.2 presents the appearance of the samples under three conditions: without ironing, with ironing immediately after printing, and with ironing followed by light sanding.

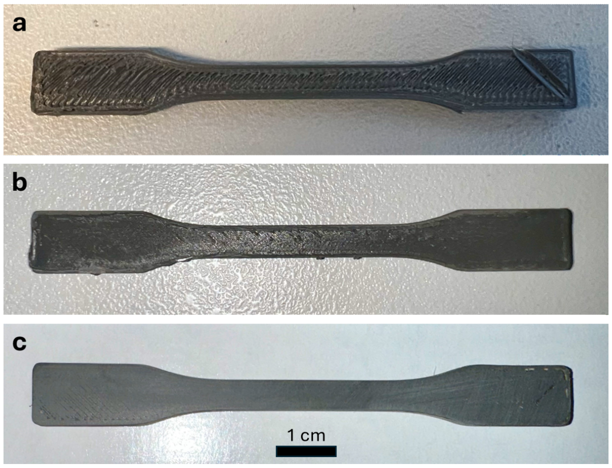

Figure 2.2: The as-printed PEEK/LRS30 sample (a) shows a pronounced bead texture and visible toolpath patterns. After ironing (b), the surface becomes noticeably smoother with reduced ridges and improved uniformity. Ironing followed by light sanding (c) produces the smoothest finish, effectively eliminating most surface irregularities.

2.3.3 Density analysis

Density analysis was performed using the Archimedean method on samples and filaments, with the results presented as percentages relative to the reference density of the material. In the case of pure PEEK, the relative density of the filament was determined to be 99.0%, whereas for the as-fabricated samples, it ranged from 98.2% to 98.8%. This demonstrates that the printing parameters, including nozzle temperature, were appropriately chosen to ensure the desired viscosity of the molten polymer during the AM process.

For PEEK/LRS30, the relative density of the filament was determined to be 79.7%, whereas for the as-fabricated samples, it ranged from 75.6% to 78.4%. The disparity in density values between the filament and the samples ranged from 1.5% to 4.0%. This discrepancy can be attributed to the elevated melt viscosity of the composite, stemming from its 30 wt% solid materials content, which poses challenges during extrusion, as discussed in previous literature [46]. The FFF method's inherent limitations could also further contribute to this variation.

2.3.4 Tensile testing

The stress-strain graph presented in Figure 2.3 illustrates the tensile properties of the as-printed specimens. For PEEK samples, tensile strength ranged from 88.1 MPa to 94.9 MPa, with the median tensile strength measured at 91.6 MPa, achieved at a strain of 15.2%. The maximum elongation at break observed for these samples was 20.43%. All subsequent data and tests for PEEK refer to the sample with this median tensile strength, unless otherwise noted. These samples exhibit ductile fracture characteristics, including noticeable necking before failure. PEEK/LRS30 samples exhibit a reduced tensile strength, ranging from 65.2 MPa to 69.1 MPa, with a median value of 67.0 MPa. All subsequent data and tests for PEEK/LRS30 are based on the sample with the median tensile strength unless indicated otherwise. The maximum elongation at break for PEEK/LRS30 was 7.8%. The results represented a 26.8% decrease in tensile strength and a 62.0% reduction in elongation compared to pure PEEK samples. This reduction is primarily attributed to the approximately 23% porosity in the PEEK/LRS30 composite, compared to less than 2% porosity in pure PEEK samples. Additionally, the PEEK/LRS30 composite displays brittle behavior, with no observable necking. The Young's modulus for the PEEK samples is approximately 917.3 MPa, while for the PEEK/LRS30 composite, it is 1152.1 MPa, indicating a 25.6% increase. This increase in stiffness can be attributed to the inherent properties of the regolith particles, which are ceramic-based materials with a higher modulus of elasticity compared to PEEK. When these rigid particles are dispersed within the polymer matrix, they constrain the deformation of the polymer chains under stress, resulting in an overall increase in the composite's stiffness [188].

Regolith introduces two opposing mechanisms affecting mechanical strength. Firstly, the presence of nanoparticles within the incorporated regolith, even at low percentages of the regolith particles falling within the nanometer range (i.e., below a few hundred nanometers), could significantly impact the composite's properties. This is particularly noteworthy given that the matrix consists of a semi-crystalline polymer like PEEK. These nanoparticles could function as a nano-reinforcement phase, enhancing mechanical properties by acting as nucleation points during solidification, resulting in finer crystals [188, 189]. Consequently, this could improve the crystallinity of the samples, with the mechanical strength and deformation-fracture behavior of PEEK being highly contingent

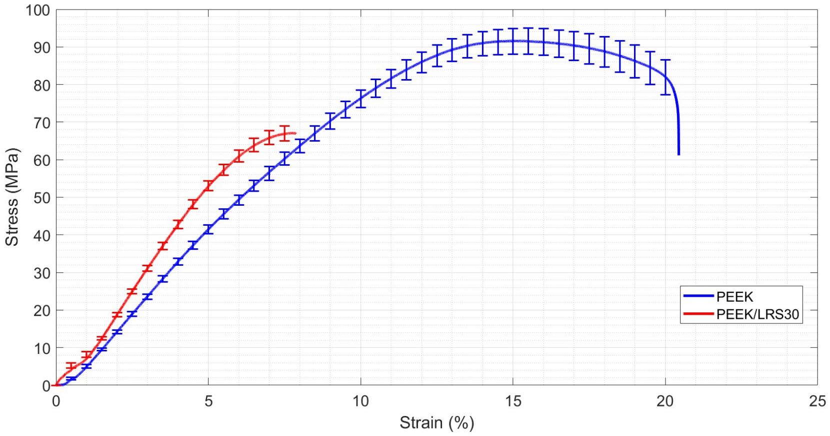

Figure 2.3: Engineering Stress vs. Strain (%) curves for as-printed samples: PEEK and PEEK/LRS30. The plot includes median curves with error bars indicating the range of uncertainty. The PEEK/LRS30 samples exhibit a higher initial slope than neat PEEK, indicating an increase in Young's modulus. However, regolith addition reduces both the ultimate tensile strength and the elongation at break. Overall, the stress–strain response shifts from more ductile behaviour in PEEK toward a comparatively more fragile (brittle-like) failure in PEEK/LRS30.

on its degree of crystallinity. Secondly, the presence of regolith content diminishes the strength of the materials due to a reduction in density percentage caused by the more challenging extrusion process resulting from higher melt viscosity [46]. While including nanoparticles could potentially enhance the tensile strength of the PEEK/LRS samples, it appears that the porosity ratio is the dominant mechanism leading to an overall decrease in mechanical strength.

All in all, although the inclusion of regolith particles decreased the tensile strength of the samples, the composite still provides sufficient strength for many Lunar applications, such as radiation shielding and structural components, where the Moon's lower gravity reduces strength requirements [190]. Also, as discussed earlier, the reduction in strength is mainly due to porosity in the material. Post-processing techniques like annealing and Hot Isostatic Pressing (HIP) can help minimize porosity and improve the crystallinity of the PEEK matrix, which is expected to enhance the composite's overall mechanical properties.

2.3.5 Microstructural analysis

Figure 2.4 presents backscattered electron (BSE) SEM micrographs depicting the polished cross-section of the specimen. The PEEK sample exhibits no visible defects in the bulk (in-layer) region (Figure 2.4(a & b)). However, visible gaps are evident between the layers, which is consistent with the FFF process. The PEEK filament cross-section shows no discernible features and is, therefore, not included in the figure.

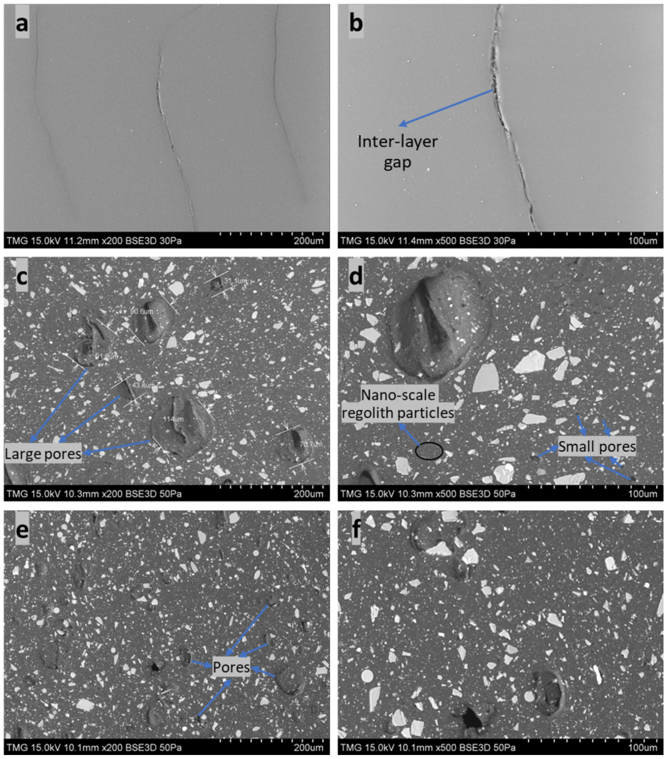

Figure 2.4: Backscattered SEM micrographs of polished cross-sections: (a–b) as-printed PEEK showing a defect-free bulk region with visible inter-layer gaps typical of FFF; (c–d) PEEK/LRS30 filament exhibiting uniform, random regolith dispersion with two pore populations (large irregular extrusion-induced pores and fine air-entrapment pores); and (e–f) as-printed PEEK/LRS30 where pore size is reduced, inter-layer boundaries are less pronounced (indicating improved bonding) and particle sizes span from tens of micrometers down to the nanometer scale.

The PEEK/LRS30 filament showcases a uniform and random distribution of regolith particles within the PEEK matrix, without any noticeable accumulation of regolith particles over the matrix, indicating the efficacy of the mixing strategy (Figure 2.4(c & d)). Nonetheless, pores are present in the structure, exhibiting two size ranges: irregularly shaped pores larger than roughly 30 microns, attributed to the extrusion process and high melt viscosity of the composite due to the solid material content, and smaller pores in the range of a few microns or less, attributed to air entrapment.

Figures 2.4(e & f) depict the as-printed samples of PEEK/LRS30, revealing that the regolith particles remain randomly distributed after printing. Additionally, there appears to be a reduction in the size of the pores post-printing, suggesting the proper selection of printing parameters. However, due to the high melt viscosity of the material and the limitations of the FFF process, complete elimination of pores is unattainable. Moreover, the inter-layer area of the composite is not visible, unlike in PEEK samples, aligning with the fracture behavior of the samples, where the PEEK/LRS30 sample demonstrates better inter-layer bonding compared to the PEEK sample. This improvement can be attributed to the effect of regolith particles, which mitigate shrinkage and warping tendencies by providing better heat distribution and promoting more uniform cooling. Furthermore, they act as nucleation agents in solidification, leading to smaller crystals and spherulite sizes. Figure 2.4(c-f) additionally shows the size variety of the regolith particles, ranging from a few tens of microns to the nanometer range.

EDS was employed to reveal the elemental composition and spatial distribution of elements within the microstructure of the PEEK/LRS30 specimen. The investigation encompassed five distinct regions of the as-printed specimen, as depicted in Figure 2.5. Zone 1 (matrix) exhibited a dense presence of carbon and oxygen atoms, confirming the presence of PEEK within this region. In this zone, the total percentage of metallic elements was negligible, with any detected presence likely attributable to sample preparation contamination. Zones 2 to 5, associated with various regolith particles, displayed significant oxygen content, as anticipated due to the regolith's composition of diverse oxides. It is important to note that the EDS analysis, combined with the color contrast between the particles and the matrix, allowed us to distinguish between them without encountering significant difficulties. In Zone 2, Ti and Fe were the predominant metallic elements, constituting 13.08% and 8.58% of the composition, respectively. Zone 3 showcased notable proportions of Mg, Si, and Fe, comprising 21.64%, 14.75%, and 3.70%, respectively. Zone 4 was characterized by a substantial Si presence, accounting for 31.4% of the composition. Lastly, Zone 5 unveiled a composition comprising 15.90% Si, 11.64% Al, 5.11% Ca, and 1.45% Na. The diverse oxide compositions observed across different regolith-containing zones underscored the heterogeneous distribution of oxides inherent in the Lunar regolith simulant used. This diverse oxide composition aligns with expectations for Lunar regolith [191].

EDS X-ray maps for the as-printed PEEK/LRS30 sample are depicted in Figure 2.6. These maps illustrate the distribution of different elements within the microstructure and further demonstrate that

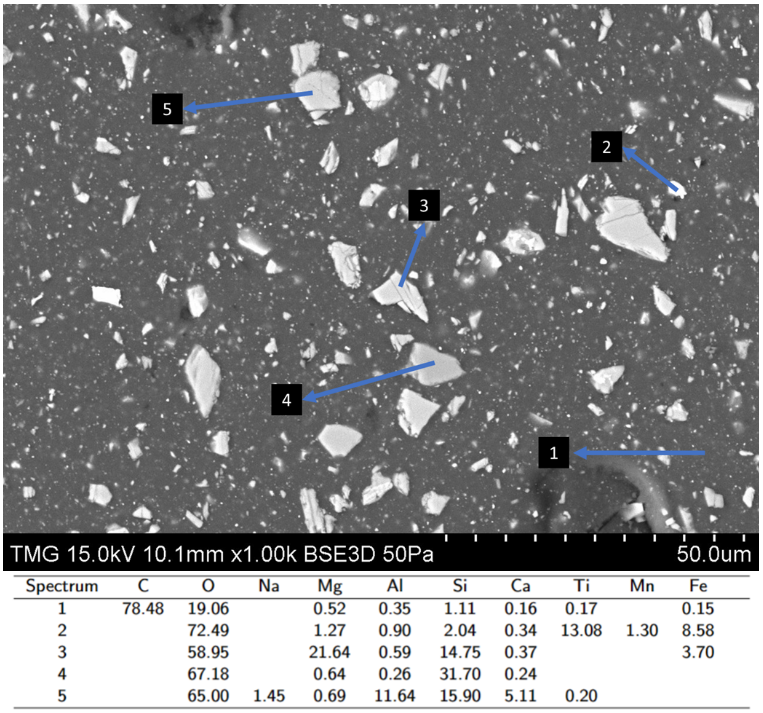

Spectrum	C	O	Na	Mg	Al	Si	Ca	Ti	Mn	Fe
1	78.48	19.06		0.52	0.35	1.11	0.16	0.17		0.15
2		72.49		1.27	0.90	2.04	0.34	13.08	1.30	8.58
3		58.95		21.64	0.59	14.75	0.37			3.70
4		67.18		0.64	0.26	31.70	0.24			
5		65.00	1.45	0.69	11.64	15.90	5.11	0.20		

Figure 2.5: EDS point analyses collected from five regions of the as-printed PEEK/LRS30 specimen. Zone 1 (matrix) contains primarily C and O, confirming the presence of PEEK with negligible metallic content. Zones 2 to 5 correspond to individual regolith particles and show diverse oxide chemistries with varying amounts of Ti, Fe, Mg, Si, Al, Ca, and Na, which reflects the heterogeneous mineralogy of the Lunar regolith simulant. The contrast between particles and matrix, combined with the compositional data, allowed clear identification of each region.

the regolith particles are dispersed randomly and uniformly throughout the matrix. Additionally, they highlight variations in composition among the various regolith particles.

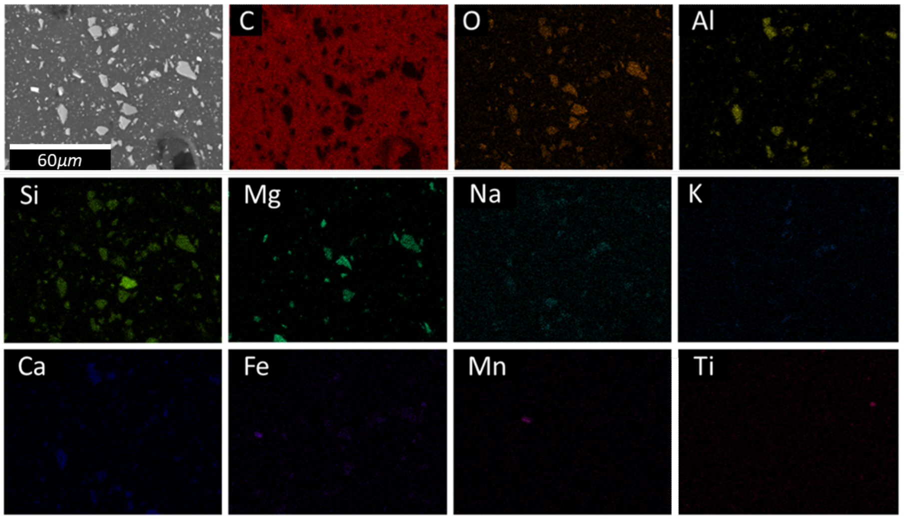

Figure 2.6: Backscattered electron image and EDS X-ray maps of the as-printed PEEK/LRS30 specimen. The elemental maps (C K_α, O K_α, Al K_α, Si K_α, Mg K_α, Na K_α, K K_α, Ca K_α, Fe K_α, Mn K_α, Ti K_α) confirm a uniform and random dispersion of regolith particles throughout the PEEK matrix. The maps also reveal particle-to-particle compositional differences, which is consistent with the mineralogical diversity of the Lunar regolith simulant.

2.4 Conclusion and future work

In summary, this phase investigated the potential of incorporating Lunar regolith into polyether ether ketone (PEEK) to reduce raw material costs for Lunar-based manufacturing and construction (LBMC) using fused filament fabrication (FFF). In this approach, PEEK acts as the binding agent, while regolith primarily serves as a filler, making it suitable for creating PEEK composites with various regolith blends. This adaptability ensures versatility in Lunar applications across different regions. Density analysis revealed that higher solid material contents pose challenges in extrusion due to increased melt viscosity, resulting in greater sample porosity. Adding 30 wt% of Lunar regolith simulant to PEEK decreased the tensile strength by 26.8%, primarily due to around 21% lower relative density. However, the resulting 67.0 MPa remains high enough for many practical applications. The addition of 30 wt% regolith also increased Young's modulus from approximately 917.3 MPa for pure PEEK to 1152.1 MPa, representing a 25.6% enhancement. Moreover, a higher content of solid materials leads to more brittle fracture and reduced elongation at break. SEM micrography alongside EDS confirmed the random distribution of regolith in the PEEK matrix, along with the presence of pores in both filament and sample after adding regolith, albeit with improved in-layer bonding.

The next phase will concentrate on exploring a wider range of PEEK/regolith ratios and achieving higher regolith weight percentages, which could significantly reduce launch costs. Additionally, we will focus on mitigating porosity through techniques such as annealing, which can also enhance the crystallinity of the PEEK matrix. We will also conduct a more comprehensive characterization of the resulting parts.

Chapter 3

Phase II: Additive Manufacturing of PEEK–Regolith Composites: Process–Composition–Property Relationships

This chapter is based on, and in parts reproduces with minor editorial changes, the following preprint:

Azami, M., Aubin-Fournier, P.-L., Hojjati, M.,& Skonieczny, K. (2025). Additive Manufacturing of PEEK/Lunar Regolith Composites for Sustainable Lunar Manufacturing. *arXiv preprint*, arXiv:2508.00894. doi:10.48550/arXiv.2508.00894.

3.1 Motivation

NASA's Artemis program marks the beginning of a new era of sustained human exploration on the Moon, requiring the development of substantial infrastructure to support long-term human presence and mission activities on the Lunar surface [49]. Developing all required materials and components on Earth and subsequently transporting them to the Lunar surface is neither practical nor sustainable, especially considering significant mass and volume constraints. Furthermore, if a component or structure on the Lunar surface requires development, replacement, or repair, it is impractical and unsafe for astronauts to await deliveries from Earth. Consequently, in-space manufacturing (ISM), and more specifically Lunar-based manufacturing and construction (LBMC), has become a central element in the strategic planning of future Lunar missions, regardless of the organization involved. [24, 26, 61, 192].

Significant volume and mass launch costs and limitations underscore the critical need for maximizing the utilization of the Moon's local resources through in-situ resource utilization (ISRU). Therefore, reducing dependence on Earth-sourced raw materials by leveraging available Lunar regolith and other indigenous resources is essential [18, 19].

To enhance operational efficiency and reduce dependency on heavy equipment transported from Earth, additive manufacturing (AM) techniques offer substantial advantages. These methods are preferred due to their minimal material waste, reduced energy consumption, increased geometric freedom, and enhanced customization capabilities [2, 20–22]. Such capabilities are particularly valuable since many Lunar-manufactured components are likely to be unique or unprecedented. Therefore, additive manufacturing, using compact printers for smaller parts and mobile, scalable systems for larger structural elements, represents a critical technological pathway toward sustainable, efficient, and responsive Lunar manufacturing and infrastructure development [23–25].

Incorporation of Lunar regolith into additive manufacturing is thus an active area of research [24, 26]. The limited availability of authentic Lunar regolith on Earth, brought back by Lunar missions, poses considerable challenges for technology development and validation for future Lunar applications. To address this limitation, several international research groups have developed Lunar regolith simulants (LRS), which are synthetic materials engineered to replicate the physical and chemical properties of Lunar regolith [27–30].

Ensuring reproducibility on the Moon of testing results with simulants motivates manufacturing processes that exhibit minimal sensitivity to variations in regolith geochemistry. This requirement arises from two primary considerations. Firstly, current simulants cannot fully replicate all Lunar regolith properties because accurately reproducing Lunar conditions on Earth is inherently difficult [193, 194]. Lunar regolith comprises a diverse mixture of highly angular and irregular mineral fragments, agglutinates, dust particles ($< 20\,\mu\mathrm{m}$), small rocks ($< 1\,\mathrm{cm}$), and larger boulders, varying significantly in composition, cohesion, packing density, abrasion resistance, and flow characteristics. These variations result from regolith maturity, location-specific geochemical processes, and environmental exposure to meteorite impacts, solar wind, and galactic cosmic radiation [194]. Secondly, significant variability in Lunar regolith properties across different Lunar regions further complicates direct replication efforts [191].

Consequently, binder-based manufacturing methods are highly attractive for Lunar applications due to their reduced sensitivity to variations in regolith composition, especially when compared to sintering or melting-based techniques such as powder-bed fusion. Among these binder-based methods, material extrusion (MEX), specifically fused filament fabrication (FFF), stands out as particularly advantageous due to the use of solid-state thermoplastic binders [4]. This preference arises because traditional liquid binders face substantial operational challenges on the Lunar surface, including incompatibility with NASA's stringent outgassing regulations in vacuum conditions and risks of boiling or freezing under the Moon's extreme temperature fluctuations. Furthermore, FFF-based material extrusion offers additional benefits such as process simplicity, minimal reliance on large, heavy equipment, and demonstrated efficiency in low-gravity environments [31–34]. Notably, MEX is highly compatible with robotic systems, particularly small mobile robots, which are preferred for ISM due to the critical need to minimize the mass and volume of equipment [25]. This makes MEX a promising approach for the construction of large-scale structures and components in future Lunar and space missions.

Among the thermoplastic binders used for MEX, many are not suitable for the harsh thermal conditions of the Lunar surface, particularly during the Lunar day when temperatures can reach 120–$130\,^{\circ}\mathrm{C}$ [24, 35]. This is because their glass transition temperatures (T_{g}) are typically well below these levels, leading to softening and deformation. For example, polylactic acid (PLA) has a T_{g} of approximately 55–65 °C and a melting temperature (T_{m}) around 160–170 °C or slightly above [36, 37], while the polyethylene (PE) family exhibits an even lower glass transition temperature (T_{g}), typically ranging from approximately -125 °C to -73 °C, and a melting point generally between 105 and 130 °C, depending on its density [38–40]. Under Lunar daytime conditions, these materials would easily deform or fail to maintain structural integrity. Another critical limitation is that not all thermoplastics comply with NASA's strict outgassing requirements for use in vacuum environments. These challenges make high-performance thermoplastics like Polyether–ether–ketone (PEEK) especially attractive for Lunar applications. PEEK offers excellent thermal stability ($T_{\mathrm{g}} = 143$ °C, $T_{\mathrm{m}} = 343$ °C), meets NASA's outgassing standards, and provides additional benefits such as radiation resistance, chemical stability, and abrasion resistance against Lunar regolith dust [41–44]. With its high strength-to-weight ratio and proven compatibility with MEX processes, PEEK stands out as a promising material for reliable and efficient Lunar manufacturing.

Processing and printing PEEK–regolith composites, however, present several significant challenges. Printing PEEK-based materials is demanding, as PEEK is highly sensitive to temperature fluctuations during fabrication. Variations in thermal conditions can induce thermal stresses, leading to deformation, warpage, and compromised part quality. In addition, PEEK exhibits relatively high melt viscosity, which complicates both the material mixing process and AM process [41, 45].

A higher proportion of PEEK in the composite increases material delivery costs, as polymers cannot be synthesized or sourced in situ on the Moon due to the extremely low carbon content in Lunar regolith. Therefore, PEEK remains an off-site, Earth-supplied material. Conversely, increasing the weight fraction of regolith in the composite is desirable to reduce reliance on Earth-sourced materials; however, high regolith filler content further increases the melt viscosity of the composite, making extrusion and processing more difficult [46]. These trade-offs must be carefully considered when designing the printing process and material formulation.

PEEK is well-regarded for its proven performance in space environments and its relatively high potential for recyclability, which can help offset the substantial costs associated with transporting materials from Earth. Although it can withstand more thermal cycles than many other polymers, repeated melting and reprocessing can still degrade its mechanical properties over time [47, 48]. Therefore, fabrication strategies should aim to minimize the number of thermal cycles to preserve material integrity and ensure long-term performance.

Efforts have been made to explore the use of MEX AM methods for fabricating regolith–thermoplastic composites. Gelino et al. [49] investigated several regolith/PLA composite formulations, including weight ratios of 70:30, 80:20, and 85:15 for Lunar Mare simulant Black Point-1 (BP-1), as well as an 80:20 blend of Lunar Highlands Simulant-1 (LHS-1) with PLA. An additional BP-1/PLA mixture incorporating a flow enhancer was also evaluated. These composites were printed under simulated Lunar thermal vacuum conditions (-190 °C, 10^{-3} torr) and characterized in terms of mixture uniformity, mechanical strength, outgassing behavior, porosity, and density. The 80:20 LHS-1/PLA composite, selected for its favorable mechanical performance and its relevance to the Lunar south polar regions, exhibited a flexural modulus of 5.3 GPa and a flexural strength of 24 MPa [49]. Despite these promising results, as previously discussed, PLA remains inherently unsuitable for uncontained Lunar applications because of its poor outgassing behavior and inadequate thermal resistance under Lunar environmental conditions.

The Phase I [3, 4] reported the first demonstration of manufacturing space-grade high-performance thermoplastic composites with Lunar regolith via MEX. That initial work focused on the FFF of PEEK/regolith composites, with comparisons drawn against pure PEEK and PEEK/carbon fiber blends. The study identified that increasing the fraction of solid particles led to extrusion challenges, particularly an increase in sample porosity. The addition of 30 wt% Lunar regolith as filler decreased tensile strength by 26.78%. Furthermore, regolith content increased brittleness and reduced elongation at break. Microstructural analysis revealed a random dispersion of regolith particles throughout the PEEK matrix, confirming the effectiveness of the mixing approach, but also indicated the presence of pores in both filaments and printed samples. Interestingly, the inclusion of regolith improved interlayer bonding [3, 4]. However, Phase I served primarily as a proof-of-concept, constrained by the inability at that stage to achieve regolith loadings above 30 wt% and by the limited scope of characterization.

To address the aforementioned challenges, this Phase II study additively manufactured PEEK/regolith composites via MEX at 0–50 wt% regolith (10 wt% increments), including pure PEEK. Pulverized

PEEK and Lunar regolith were blended and processed into filament form via a twin-screw extruder with a customized screw configuration. The resulting filaments were printed using an FFF MEX system equipped with a heated chamber and a fine-tuned, previously unreported setup, under conditions that enabled in-situ annealing during the printing process. To assess the effects of thermal post-processing, a subset of the printed samples underwent additional annealing, while others remained untreated. The printed composites were evaluated and compared in terms of crystallinity, density, mechanical performance, and microstructural characteristics. To the best of our knowledge, this study reports the highest Lunar regolith content incorporated into PEEK to date, using a 50:50 wt% ratio. PEEK, as a high-performance, high-temperature thermoplastic, was processed via MEX. Specifically, (i) PEEK/regolith composites were developed and successfully printed, (ii) processing parameters were fine-tuned to ensure printability and dimensional fidelity, and (iii) key mechanical, thermal, and microstructural characterizations were conducted. The results highlight both the promise and the practical design limits of regolith-rich thermoplastic composites, representing a significant step toward ISRU for the additive manufacturing of Lunar infrastructure, outposts, and functional components.

3.2 Materials and Methods

3.2.1 Filament making

Polyether–ether–ketone (PEEK) pellets (90G, Victrex, United Kingdom) were pulverized using a 254 mm Lab Pulverizer (Orenda, Canada) to achieve an average particle size of approximately $150\,\mu$m. The resulting PEEK powder was pre-mixed with 10–50 wt% of as-received Lunar regolith simulant (LMS-1D, Exolith, United States), which features a particle size distribution ranging from < 0.04 to $32\,\mu$m, with a mean particle size of $7\,\mu$m, a median (D_{50}) of $4\,\mu$m, D_{10} of approximately $1\,\mu$m, and D_{90} of 15–16 μm. According to the supplier, these values were obtained via laser diffraction analysis using a CILAS 1190 particle size analyzer (CILAS, France) [5]. The simulant has a reported grain density of $2.92\,\text{g/cm}^3$. LMS-1D was selected for its close resemblance to Lunar mare dust in terms of particle size distribution, which is a critical parameter influencing composite printability and mechanical performance. The fine particle size aids in achieving uniform dispersion of the regolith within the polymer matrix, thereby reducing stress concentrations and minimizing mechanical failure risks [187].

Compared to Phase I [3, 4], substantial improvements were made to the filament production process to ensure consistent filament diameter and to increase the extruder's capacity for higher regolith loading. These enhancements included replacing the previously used custom-built filament tensioner with a commercial model, which enabled more stable filament formation and eliminated fluctuations in filament thickness during extrusion. Additionally, a high-performance polymer screw configuration (see Figure 3.1) was implemented in the extrusion system to further improve processing quality. While the prior setup limited regolith content to a maximum of 30 wt%, the optimized screw design allowed successful processing of filaments containing up to 50 wt% regolith.

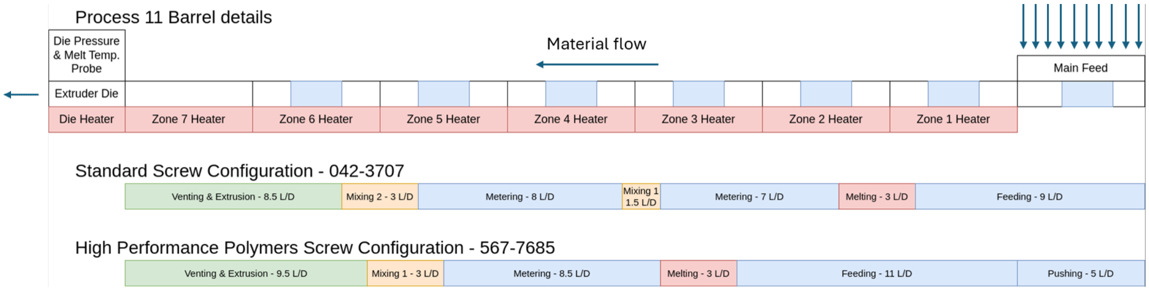

Figure 3.1: Schematic of the filament making process using the Process 11 twin-screw extruder. The standard screw configuration used in [3, 4] is compared with the high-performance polymers screw configuration employed in the current study. The updated setup enabled processing of up to 50 wt% Lunar regolith simulant (LRS). L/D denotes the length-to-diameter ratio.

The PEEK/Lunar regolith simulant (PEEK/LRS) composite powder was extruded into filament using a parallel twin-screw extruder (Process 11, Thermo Scientific™, Germany), with temperature zones ranging from 355 °C to 380 °C and a screw speed of 50–100 rpm.

For comparative purposes, identical procedures were applied to a commercial PEEK filament (K10, Kexcelled, China), which served as the baseline material in this study.

Prior to printing, all filaments were dried at 65 °C for 24 hours using a filament dryer to minimize moisture content and ensure consistent extrusion quality.

3.2.2 Additive manufacturing

A high-temperature FFF MEX 3D printer (PEEK 300, CreatBot, China) was utilized to process the prepared composite filaments. To enhance crystallinity and reduce thermal-induced stress, the printer's Direct Annealing System (DAS) was employed, which delivers a controlled stream of hot air at 420 °C directly to the printed component. Additionally, the build chamber temperature was maintained at 120 °C to minimize thermal gradients and residual stresses throughout the part. Printing parameters were fine-tuned for each composition to ensure reliable printability and defect-free structures.

In Phase I [3, 4], the following samples were fabricated using the printing parameters summarized in Table 3.1: neat PEEK (**PEEK**), PEEK reinforced with 20 wt% chopped carbon fiber (**PEEK/CF20**), and PEEK composites containing 15 wt% and 30 wt% Lunar regolith simulant (**PEEK/LRS15** and **PEEK/LRS30**, respectively). While acceptable results were achieved, further enhancements in print quality were identified as possible. Consequently, a revised set of printing parameters was applied to a second series of samples, which included neat PEEK and PEEK composites containing 10–50 wt% LRS. These samples are referred to as **PEEK**, **PEEK/LRS10**, **PEEK/LRS20**, **PEEK/LRS30**, **PEEK/LRS40**, and **PEEK/LRS50** throughout this study. The updated parameters used for their fabrication are summarized in Table 3.2.

For the prior batch of samples [3, 4], printing was performed on a raft made from the same material as the part, using a single-nozzle configuration. To improve both bed adhesion and bonding between the raft and the printed PEEK/LRS part, a dual-nozzle approach was adopted for this study. In this configuration, the raft, which serves as an intermediate layer between the build plate and the printed component, was fabricated using polyether–ketone–ketone (PEKK). Due to its superior adhesion to the build surface and strong interfacial bonding with PEEK, PEKK significantly reduced detachment during printing and minimized warpage. This improvement enhanced dimensional accuracy and improved the overall structural integrity of the printed parts. The use of PEKK as a dedicated raft material effectively mitigated common challenges in PEEK printing, including delamination, warping, and dimensional inconsistency. The layer-by-layer deposition sequence used for all specimens is illustrated in Fig. 3.2, highlighting the raster orientation and the two-pass perimeter strategy applied after each infill region. The figure shows the toolpath for two successive layers, printed with alternating raster angles, representing the pattern repeated throughout the build until the full specimen height is achieved.

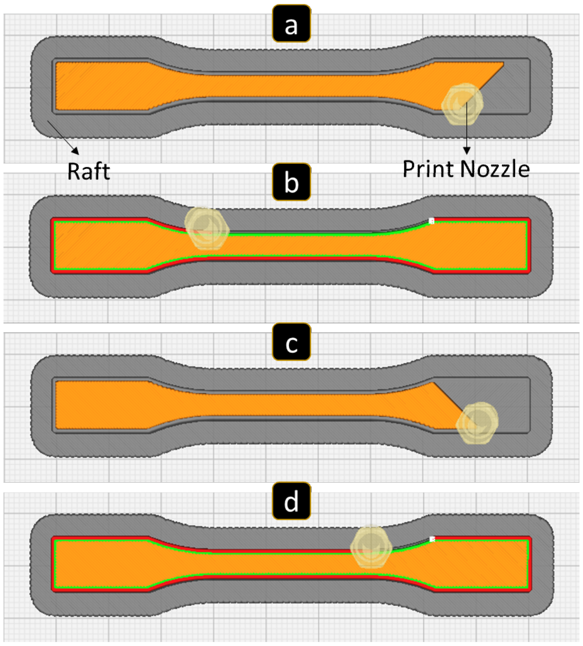

Figure 3.2: Illustration of the deposition sequence used for fabricating tensile specimens over two successive layers. This alternating raster and perimeter sequence is repeated throughout the build until the full specimen height is achieved. (a) Initial raster pattern deposited at a 45° angle in the xy-plane on a raft. (b) After depositing the infill, two perimeter (wall) passes are printed following the contour of the specimen. (c) Subsequent layer printed with a 90° rotated raster. (d) Two perimeter passes deposited after completing the rotated raster. In all subfigures, orange denotes the infill, gray denotes the raft, and red/green lines indicate the nozzle path for the perimeter walls.

To evaluate reproducibility, three specimens of each composition were printed. In Phase I [3, 4], the surface smoothness of the first set of samples was improved using the ironing feature in UltiMaker Cura; ironing may also reduce residual stress through localized reheating. However, ironing was omitted for the samples in the current study, as it introduced inconsistencies in properties and resulted in nozzle clogging at higher regolith loadings.

3.2.3 Annealing heat treatment

Although the printer's DAS provided in-situ annealing during the printing process, an additional post-processing annealing step was carried out on a subset of samples to assess its influence on the

Table 3.1: Summary of the printing parameters used in Phase I. [3, 4].

Material	Nozzle Temp. (°C)	Bed Temp. (°C)	Ambient Temp. (°C)	Layer Thickness (mm)	Print Speed (mm/s)	Infill Density (%)	Nozzle Diameter (mm)	Bed Adhesion Mechanism
PEEK	420	180	120	0.25	7.5	100	0.4	PEEK Raft
PEEK/CF20	400	150	120	0.25	20	100	0.4	None
PEEK/LRS15	420	180	120	0.25	7.5	100	0.4	PEEK/LRS15 Raft
PEEK/LRS30	420	180	120	0.25	7.5	100	0.4	PEEK/LRS30 Raft

Table 3.2: Summary of the printing parameters used in the current study.

Material	Nozzle Temp. (°C)	Bed Temp. (°C)	Ambient Temp. (°C)	Layer Thickness (mm)	Print Speed (mm/s)	Infill Density (%)	Nozzle Diameter (mm)	Bed Adhesion Mechanism
PEEK	430	180	120	0.25	7.5	100	0.4	PEEK Raft
PEEK/LRS	430	180	120	0.25	7.5	100	0.4	PEKK Raft

properties of the as-printed parts. These specimens will be referred to as “annealed” throughout the remainder of this article. The annealing procedure was conducted in a furnace, where the sample temperature was increased at a controlled rate of 5 °C/min until reaching 300 °C. The samples were held at this temperature for 2 hours, followed by gradual cooling inside the furnace by simply turning off the heating element and allowing the system to cool down naturally.

3.2.4 Differential scanning calorimetry (DSC)

Thermal behavior was analyzed using a TA Instruments DSC Q200 equipped with *Universal Analysis* V4.7A software (TA Instruments, USA). Each specimen, cut from samples, was sealed in a standard aluminum pan and run against an empty reference under a dry nitrogen purge (50 mL min^{-1}). The thermal program consisted of a single heating and cooling cycle: samples were stabilized at $50\,^{\circ}\mathrm{C}$, heated to $450\,^{\circ}\mathrm{C}$ at $10\,^{\circ}\mathrm{C\,min^{-1}}$, and immediately cooled back to $50\,^{\circ}\mathrm{C}$ at the same rate. No second heating was performed. Various compositions of materials were examined, ranging from neat PEEK to composites containing up to 50 wt% regolith.

The degree of crystallinity of the polymer phase (χ) was calculated based on the net enthalpy of fusion, following the approach adopted by Yap et al. [195]:

$$\chi = 100\% \times \left(\frac{\Delta H_m + \Delta H_c}{\Delta H_f \, (1 - w_f)} \right), \tag{1}$$

In this equation, ΔH_m refers to the enthalpy of fusion obtained from the melting endotherm ($\mathrm{J\,g^{-1}}$), while ΔH_c is the magnitude of the crystallization exotherm ($\mathrm{J\,g^{-1}}$). The reference value $\Delta H_f = 130\,\mathrm{J\,g^{-1}}$ corresponds to the enthalpy of fusion for fully crystalline PEEK [196], and w_f represents the mass fraction of regolith filler. All enthalpy values were initially normalized to the total mass of the composite; division by $(1 - w_f)$ subsequently converts them to a polymer-phase basis, thereby correcting for the dilution effect introduced by the inert filler.

3.2.5 Tensile examination

For tensile testing, all specimens were prepared in accordance with ISO 527. Tests were conducted on a 5000 N universal testing machine (Hoskin Scientific, Canada) at a constant crosshead speed of 2 mm/min. An extensometer was not used and strain was evaluated from the machine crosshead displacement, and particular care was taken during specimen gripping to minimize slippage.

3.2.6 Density assessment

The density of both the filaments and the printed samples was measured using Archimedean density analysis, employing a density determination kit (YDK02MS, Sartorius, Germany) with deionized water at 22 °C as the immersion medium.

3.2.7 Micrography

Microstructural characterization of both the filaments and as-printed specimens was performed using a scanning electron microscope (SEM, S-3400N, Hitachi, Japan). Prior to imaging, cross-sectional samples were polished to enable high-resolution surface examination. Elemental composition was analyzed using energy-dispersive X-ray spectroscopy (EDS). To ensure a comprehensive assessment, EDS mapping was also conducted over broad regions rather than isolated points. Continuous signal acquisition across the selected areas allowed the generation of spatially resolved elemental distribution maps, providing insights into the homogeneity and dispersion of the composite constituents.

3.3 Results and Discussion

3.3.1 Filament preparation

As detailed in Phase I [3, 4], the use of pulverized PEEK, combined with an increased screw speed of 100 rpm and a maintained processing temperature of 380 °C, enabled successful processing of the PEEK/regolith composite using a twin-screw extruder. This approach yielded a uniform filament (other than some short-lived inconsistencies), with the extruder's high shear mixing capability playing a crucial role in achieving homogeneous dispersion of the regolith particles. This was further supported by the stable torque observed throughout the extrusion process. Figure 3.3 presents an example comparison between the neat PEEK filament and the composite filament containing 30 wt% regolith.

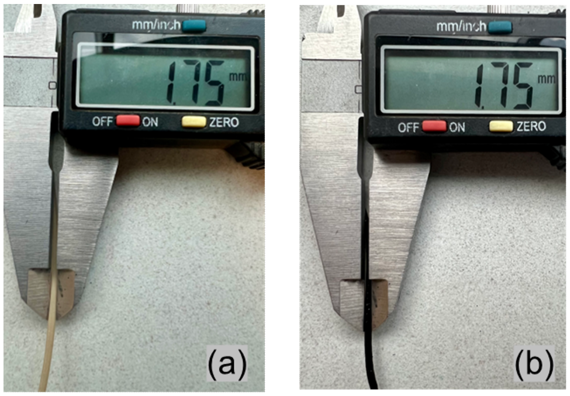

Figure 3.3: Filament comparison: (a) neat PEEK and (b) PEEK/LRS30. The regolith-containing filament exhibits a noticeably darker color, and its diameter remains consistent with the required filament specifications.

However, increasing the regolith content beyond 30 wt% resulted in a significant rise in torque, which adversely affected the extrusion process. A 10–15% increase in torque was already observed when the regolith content increased from 15 wt% to 30 wt%, primarily due to the elevated melt viscosity of the mixture. This viscosity increase is attributed to the higher proportion of solid particles that remain unmelted during processing, as reported in [46]. At contents exceeding 30 wt%, the torque rose further, making continuous extrusion increasingly difficult. Additionally, intermittent inconsistencies in filament diameter, typically spanning 1–4 cm in length, were occasionally observed. These defects required manual intervention to remove the affected segments and resume spooling. An example of such an inconsistency is shown in Figure 3.4.

Subsequent improvements implemented in this work included replacing the custom-built filament tensioner with a commercial unit and adopting the “high-performance polymer” screw configuration recommended by the twin-screw extruder’s manufacturer (Thermo Scientific™, Germany). These modifications collectively resulted in a 30–40% reduction in torque during extrusion compared to the original configuration. Notably, this setup enabled the successful extrusion of composite blends containing up to 50 wt% regolith. This was achieved through a combination of the improved screw configuration, a 30% reduction in screw speed, and a 10 °C increase in processing temperature across all extruder zones. Remarkably, the torque recorded during extrusion of the 50 wt% blend was over 10% lower than that observed for the 30 wt% blend processed with the initial configuration. Although processing even higher regolith contents may be technically feasible, the blend ratio was intentionally limited to 50 wt% as a precaution against any potential accumulative negative effects on the mechanical integrity of the extruder.

Figure 3.4: Example of intermittent filament diameter inconsistency, typically occurring over lengths of 1 to 4 cm during extrusion prior to implementing the improved screw configuration and a more effective filament tensioner.

3.3.2 Additive manufacturing

Following filament preparation, a range of printing parameters, including nozzle temperature, bed temperature, and printing speed, were systematically fine-tuned to enhance the quality of the printed specimens. Any parts exhibiting visible defects such as cracking or excessive porosity were excluded from further analysis. The specimens fabricated using the fine-tuned parameters listed in Table 3.2 displayed no observable defects.

Print consistency and process repeatability were confirmed through visual inspection, tensile testing, density measurements, and dimensional analysis. These evaluations indicate that the refined parameters produced reliable and reproducible results across different material compositions.

A key finding of this study is that incorporating regolith into the polymer matrix significantly reduced delamination and warping, which are common challenges in pure PEEK prints, resulting in enhanced dimensional accuracy and higher print success rates.

To further enhance print quality, PEKK was introduced as the raft material in place of PEEK/LRS composites. This modification proved critical for print reliability. When PEEK-based rafts (composed of the same material as the printed part) were used, success rate was less than 50%. In contrast, substituting PEKK as the raft material resulted in an almost 100% success rate. This outcome underscores the importance of interfacial adhesion, both between the raft and the print bed and between the raft and the printed structure. Acting as an effective intermediary, PEKK provided superior bonding at both interfaces, thereby eliminating adhesion-related failures. This improvement represents a significant advancement in the additive manufacturing of PEEK-regolith composites, especially in the context of space-based fabrication, where minimizing material waste and maximizing print reliability is critical. Representative samples from this phase are shown in Figure 3.5.

Figure 3.5: Representative as-printed tensile specimens spanning the full composition range from neat PEEK to PEEK reinforced with 50 wt% regolith. The progressive darkening of the material with increasing regolith content reflects the oxide-rich particulate phase, while all compositions retain consistent overall geometry.

3.3.3 Effect of annealing

Upon annealing, no notable changes were observed in the color or overall dimensions of the samples, aside from a slight and uniform shrinkage likely associated with pore consolidation. The parts retained their structural integrity. The effects of annealing on other material properties are discussed in the corresponding sections.

3.3.4 Density analysis

The relative density of the feedstock filaments, as-printed specimens, and annealed samples for neat PEEK as well as all PEEK/LRS composites was determined using the Archimedean method and reported as a percentage of the corresponding nominal theoretical density (see Table 3.3). It was observed that, for all compositions and manufacturing strategies, the variation in relative density across replicates remained below 3%. To facilitate a clearer interpretation of compositional trends, the values reported here correspond to the samples exhibiting median tensile strength for each composition.

For pure **PEEK**, the filament exhibited a high density of 99.0%, while both the as-printed and annealed specimens maintained densities exceeding 99%. These results confirm that the selected thermal and processing parameters, particularly the nozzle temperature and chamber conditioning, were effective in promoting sufficient melt flow and inter-raster bonding during printing, yielding a slight improvement over the outcomes reported in Phase I [4].

For the **PEEK/LRS10** composite, the filament exhibited a relative density of 97.8%. Printing improved this to 98.5%, indicating that the melt pressure and thermal conditions were sufficient to overcome the moderate viscosity increase due to filler addition. Annealing at 300 °C further increased the density to above 99%, highlighting the effectiveness of post-processing in eliminating residual porosity.

The **PEEK/LRS20** filament showed a slightly lower density of 97.0%, attributed to increased melt viscosity with higher filler content. After printing, the density increased to 97.6%, and subsequent annealing restored it to above 99%, confirming that the matrix retained sufficient mobility for defect healing and densification.

For the **PEEK/LRS30** composite, filament density dropped further to 96.1%, and printing offered only a marginal improvement (96.2%), indicating that inter-raster fusion was hindered by the higher viscosity. Annealing yielded a modest increase to 97.2%, reflecting the diminishing effectiveness of thermal post-treatment at higher filler contents.

The **PEEK/LRS40** filament exhibited a higher density (98.2%) than PEEK/LRS30, which is attributed to process modifications during extrusion: the twin-screw rpm was reduced by half, allowing more time for air evacuation, and the increased solid content elevated die pressure, enhancing melt compaction. Nevertheless, the as-printed density dropped to 95.1% (–3.1%), primarily due to inadequate flow under the high-viscosity conditions. Annealing offered limited improvement, increasing density by only 0.5%.

In the **PEEK/LRS50** case, filament density declined to 96.9% (–1.3% compared to PEEK/LRS40). High viscosity prevented adequate melt pressure and flow continuity during printing, leading to a substantial reduction in as-printed density to 92.5% (–4.5% compared to filament). Annealing resulted in only a 0.3% gain, underscoring the limited mobility of the polymer chains within the highly constrained matrix.

Trend analysis. Up to 30 wt% regolith, filament porosity increases progressively with filler content due to rising melt viscosity. At 40 wt% there is a discontinuity in the trend, with improved filament density (i.e. a drop in porosity) resulting from longer residence time and higher die pressure during extrusion. At 50 wt%, porosity increases again, likely due to the limits of degassing efficiency under extreme viscosity. Further reduction in screw speed might have improved air evacuation, but was avoided to prevent material degradation due to prolonged residence in the high-temperature barrel. For regolith contents of 10 wt% to 30 wt%, porosity decreases during printing (relative to filament porosity), as the process conditions effectively promote interbead diffusion. Beyond this point in regolith content, the trend reverses: the as-printed porosity increases sharply due to poor flow and inadequate bead fusion at high filler loadings. Further increasing the nozzle temperature was not pursued, as the selected setting (430 °C) approaches the onset of thermal degradation in PEEK.

Post-processing annealing was effective for composites with 10 wt% and 20 wt%, closing interfacial voids. However, as regolith content increases further, the benefits diminish considerably.

This trend is attributed to reduced chain mobility: at the annealing temperature of 300 °C (approximately 44 °C below the melting point of PEEK), polymer segments must diffuse around rigid filler particles. As the filler content increases, the available free matrix volume decreases, limiting molecular rearrangement and the potential for crystallinity development, weld healing, and porosity reduction. Consequently, the mechanical enhancement achievable through annealing becomes increasingly constrained at higher regolith loadings.

Table 3.3: Representative as-printed tensile specimens spanning the full composition range from neat PEEK to PEEK reinforced with 50 wt% regolith. The specimens gradually darken with increasing regolith content, consistent with the inherent color of the Lunar regolith simulant, while maintaining comparable overall geometry across all compositions.

Regolith Content (wt%)	**Filament (%)**	**As-Printed (%)**	**Annealed (%)**	**%Δ Fil→Pr**	**%Δ Pr→Ann**	**%Δ Fil vs Prev**	**%Δ Pr vs Prev**	**%Δ Ann vs Prev**
0 (Pure PEEK)	> 99	> 99	> 99	–	–	–	–	–
10	97.8	98.5	> 99	+0.72%	≥+0.51%	–	–	–
20	97.0	97.6	> 99	+0.62%	≥+1.44%	–0.82%	–0.91%	–
30	96.1	96.2	97.2	+0.10%	+1.04%	–0.93%	–1.43%	–
40	98.2*	95.1	95.6	–3.16%	+0.53%	+2.19%*	–1.14%*	–1.65%*
50	96.9	92.5	92.8	–4.54%	+0.32%	–1.32%	–2.73%	–2.93%

3.3.5 Differential scanning calorimetry (DSC)

As shown in Figure 3.6a, DSC revealed that the as-printed neat PEEK exhibited a degree of crystallinity of 17.4%. Incorporation of regolith increased the crystallinity to $20.5 \pm 1.3\%$ across the composites, with a gradual increase up to 40 wt%, followed by a slight decrease at 50 wt%. The regolith particles, particularly those at the nano- and submicron scales, serve as effective heterogeneous nucleation sites, lowering the energy barrier for crystallization during cooling. This promotes rapid nucleation and leads to the formation of numerous fine crystal grains. However, in the presence of filler, the crystallization peak temperature (T_{cp}) shifts to lower values, decreasing from 296.6 °C for pure PEEK to 289.1 ± 0.7 °C for the PEEK/LRS composites (see Figure 3.6b). This downward shift indicates an increasing restriction in PEEK chain mobility during solidification. In this regime, the reduced molecular mobility becomes the dominant influence, limiting crystal growth and slightly decreasing both T_{cp} and the overall crystallinity (X_{c}). Consequently, at high filler contents, the inhibitory effect on chain mobility outweighs the nucleation-enhancing benefits of the particles [197].

A representative DSC thermogram is provided in Figure 3.7 to illustrate the typical thermal

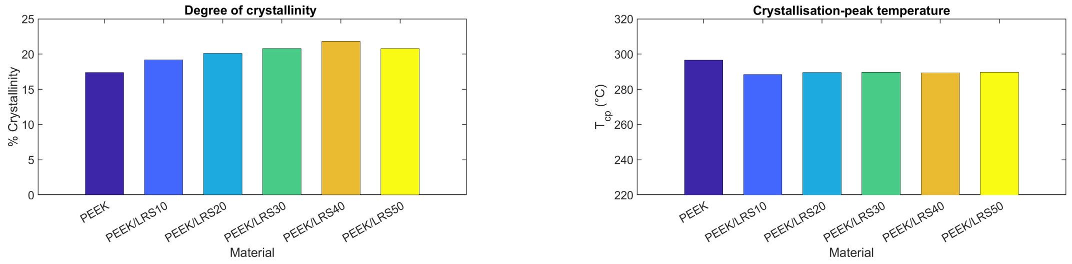

(a) Degree of crystallinity.

(b) Crystallization-peak temperature, T_{cp}.

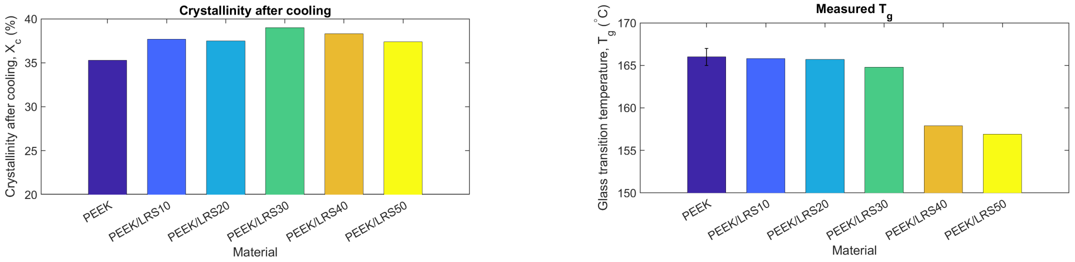

(c) Crystallinity after cooling, X_c.

(d) Glass transition temperature, T_g.

Figure 3.6: Differential scanning calorimetry (DSC) results for as-printed neat PEEK and PEEK/LRS composites. The degree of crystallinity after the heating cycle increases from 17.4% in neat PEEK to about 20.5% in the regolith-filled blends, with a slight reduction at 50 wt% LRS, while the crystallization-peak temperature T_{cp} decreases from 296.6 °C to approximately 289 °C, indicating reduced chain mobility during solidification. Crystallinity after cooling X_{c} remains similar for all compositions, averaging about 38%, and the glass transition temperature T_{g} stays near 165 °C up to 30 wt% LRS but decreases for 40 and 50 wt% LRS, consistent with increased processing-induced defects and porosity at higher filler loadings.

behavior, while key thermal parameters for various compositions are summarized in Figure 3.6.

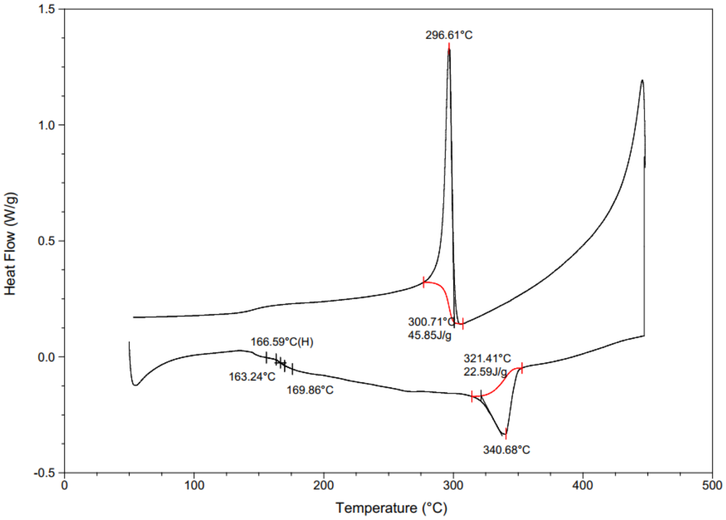

Figure 3.7: Representative DSC thermogram of as-printed neat PEEK, showing the heating and cooling cycles. The heating curve displays the glass transition region, followed by the endothermic melting peak near 340–350 °C, while the cooling curve exhibits the crystallization exotherm with a peak at approximately 296.6 °C.

The crystallization exotherms recorded during the cooling cycle revealed that the neat PEEK sample achieved a crystallinity of 35.3%, while all PEEK/LRS composites exhibited comparable values, averaging $38.3 \pm 0.7\%$ (see Figure 3.6c). This consistency is primarily attributed to the fixed cooling rate of $10\,^{\circ}\mathrm{C\,min^{-1}}$, which ensured uniform and sufficiently slow thermal conditions across all samples. For neat PEEK, the relatively high crystallization peak temperature $(T_{\mathrm{cp}} = 296.6\,^{\circ}\mathrm{C})$ and high chain mobility provided adequate time for lamellar growth. In contrast, the PEEK/LRS composites underwent rapid heterogeneous nucleation due to the abundance of regolith particles, resulting in an average increase of 3.0 percentage points in crystallinity (from 35.3% to 38.3%). At these higher crystallinity levels, the process becomes growth-limited rather than nucleation-limited. Once nucleation sites are saturated, further increases in filler content no longer enhance crystallinity, and the final degree of crystallinity is largely governed by the imposed cooling conditions.

The glass transition temperature (T_{g}) of as-printed neat PEEK was measured to be $166 \pm 1\,^{\circ}\mathrm{C}$, based on four repeated tests. Notably, these values are significantly higher than the typical T_{g} reported in data sheets (onset at 143 °C and midpoint at 150 °C), which can be attributed to the elevated thermal conditions applied during printing. Specifically, Creatbot's DAS was employed, wherein both tuyeres directed hot air at $420\,^{\circ}\mathrm{C}$, complemented by a heated bed at $180\,^{\circ}\mathrm{C}$, and a build chamber maintained at $120\,^{\circ}\mathrm{C}$. Similar T_{g} elevations have also been reported in previous studies [198, 199]. The observed increase in T_{g} results from a combination of crystallization and thermally induced changes in the amorphous phase. While annealing is commonly associated with enhancements in crystalline structure and degree of crystallinity in semi-crystalline polymers such as PEEK, it also significantly reduces chain mobility within the rigid amorphous regions. This reduced mobility contributes to the observed elevation in T_{g} [199, 200].

As shown in Figure 3.6d, the glass transition temperature (T_{g}) remained stable at $165.2 \pm 0.5\,^{\circ}\mathrm{C}$ for composites containing up to 30 wt% LRS. However, it decreased noticeably to $157.9\,^{\circ}\mathrm{C}$ and $156.9\,^{\circ}\mathrm{C}$ for the 40 wt% and 50 wt% LRS composites, respectively. This reduction is attributed to the increased incidence of processing-induced defects and increased porosity in as-printed parts at higher filler loadings, which elevate the free volume and enhance segmental mobility within the polymer matrix [201].

For the annealed samples, a modest increase in crystallinity was observed for neat PEEK, rising from 17.4% to 20.1%. In contrast, no meaningful change was detected in the DSC data of the PEEK/LRS composites compared to the as-printed specimens. DSC analysis indicated that annealing at $300\,^{\circ}\mathrm{C}$ should be sufficient to promote crystallization in PEEK without risking part deformation. Specifically, the cooling curves of the as-printed samples display a pronounced exothermic crystallization peak ending just below $300\,^{\circ}\mathrm{C}$, confirming that this temperature lies within the effective crystallization window. Meanwhile, the heating curves reveal that melting onset begins around $321\,^{\circ}\mathrm{C}$, suggesting that annealing above $300\,^{\circ}\mathrm{C}$ would approach the deformation threshold. Therefore, holding the parts at $300\,^{\circ}\mathrm{C}$ should, in principle, enable further crystal growth while maintaining dimensional stability, making it a practical and thermally safe annealing temperature.

This annealing condition is more aggressive than many protocols reported in the literature. For example, Lannunziata et al. [199] and Sarasua et al. [202] used temperatures as low as $200\,^{\circ}\mathrm{C}$. However, no appreciable increase in the crystallinity of the PEEK/LRS samples was observed. One contributing factor may be the partial crystallization that occurred during the printing process itself. The slow-cooling environment, characterized by a high bed and ambient temperature, and the simultaneous annealing enabled by the DAS system facilitated primary crystal formation during printing.

Once a lamellar network is established, further crystal growth requires long-range chain diffusion, which becomes increasingly limited under these conditions.

Additionally, in the PEEK/LRS composites, the regolith particles disrupt the continuity of the polymer matrix by creating isolated domains and interfacial layers where chain mobility is suppressed. These particles act as barriers to lamellar propagation, restricting crystallization to already available polymer-rich regions. Furthermore, the presence of interlayer gaps in MEX-printed PEEK introduces microvoids and poorly bonded interfaces, which reduce chain continuity and hinder the nucleation and growth of crystalline domains.

Although slightly higher annealing temperatures (e.g., $315-320\,^{\circ}\mathrm{C}$) might enhance recrystallization, they also pose a higher risk of deformation. In the context of space applications, such thermal treatments may be impractical due to additional energy, equipment, and time demands. Thus, while $300\,^{\circ}\mathrm{C}$ is thermodynamically favorable for crystallization, the combination of kinetic constraints, filler-induced barriers, and structural discontinuities limited the observed crystallinity increase in the samples from post-process annealing.

3.3.6 Tensile testing

Figure 3.8 presents the engineering stress-strain curves for the as-printed samples fabricated in the current work, including neat PEEK and PEEK/LRS composites containing 10–50 wt% Lunar regolith simulant. As-printed **neat PEEK** exhibited the highest tensile performance among all samples, with an ultimate tensile strength (UTS) of 107.4 MPa and elongation at break of 14.1 %. The material demonstrated ductile fracture behavior with a visible necking phenomenon prior to failure. When compared to the results reported in Phase I [4], this corresponds to a 17.3 % increase in UTS and a 30.1 % reduction in elongation at break. Given that the porosity levels in both studies remained nearly unchanged, these mechanical differences are attributed primarily to the increased crystallinity achieved in the current study. This enhancement is likely due to the use of a higher nozzle temperature combined with the activation of both DAS tuyeres during printing. These conditions promote better thermal management and improved interbead fusion. The Young's modulus for neat PEEK in the current work was 1,094.0 MPa, reflecting a 19.3 % increase relative to the value reported in Phase I [4].

The addition of regolith (up to 40 wt%) resulted in a gradual reduction in both elongation at break and ultimate tensile strength (UTS), while stiffness increased with filler content. The as-printed **PEEK/LRS10** sample exhibited an elongation at break of 10.4 %, a UTS of 100.5 MPa, and a Young's modulus of 1,225.3 MPa, corresponding to a 26.2 % reduction in elongation, a 6.4 % decrease in UTS, and a 12.0 % increase in stiffness relative to neat PEEK. For as-printed **PEEK/LRS20**, the corresponding values were 9.8 %, 97.2 MPa, and 1,307.9 MPa, representing a 30.5 % reduction in elongation, a 9.5 % reduction in UTS, and a 19.6 % increase in elastic modulus relative to neat PEEK. The trend continued with as-printed **PEEK/LRS30**, which showed values of 8.5 %, 94.8 MPa, and 1,402.6 MPa, corresponding to a 39.7 % reduction in elongation, an 11.7 % decrease in UTS, and a 28.2 % increase in elastic modulus relative to neat PEEK. As-printed **PEEK/LRS40** exhibited elongation, UTS, and modulus values of 7.5 %, 90.3 MPa, and 1,544.9 MPa, respectively, representing a 46.8 % reduction in elongation, a 15.9 % decrease in UTS, and a 41.2 % increase in stiffness compared to neat PEEK.

A direct comparison with the as-printed PEEK/LRS30 data from Phase I [4] further highlights the superiority of the current process. In the prior work, PEEK/LRS30 exhibited a tensile strength of only 67.1 MPa, 7.9 % elongation, and a Young's modulus of 1152.1 MPa. In contrast, the present results show improvements of 41.3 % in UTS, 7.6 % in elongation, and 21.7 % in elastic modulus over the prior results. These improvements are attributed to higher print quality, diminished porosity, and stronger interbead bonding achieved through the refinements of the process parameters described earlier.

However, when the filler content was increased to 50 wt%, the mechanical performance began to deteriorate. The as-printed **PEEK/LRS50** composite showed a UTS of 70.4 MPa, elongation of 6.0 %, and Young's modulus of 1,268.2 MPa. This represents a 22.0 % decrease in UTS, a 20.0 % reduction in elongation, and a 17.9 % decrease in stiffness compared to the PEEK/LRS40 sample. Interestingly, the modulus dropped below the value observed for PEEK/LRS30, indicating a deviation from the earlier increasing trend. This behavior is likely the result of excessive melt viscosity at such high filler concentrations, which severely restricted polymer chain mobility and extrusion flow, leading to higher porosity and weaker interbead bonding.

All PEEK/LRS composites exhibited brittle fracture behavior, characterized by the absence of necking. The mechanical properties follow a consistent trend with increasing regolith content: for every additional 10 wt% of filler, the UTS decreased by approximately 2.5–6.4 %, elongation at break dropped by less than 12 %, and Young's modulus increased by 6.7–12.0 %. Between neat PEEK and PEEK/LRS10, for instance, there was a 26.2 % decrease in elongation, while the modulus increased by 12.0 %.

The observed mechanical response is governed by two competing mechanisms. On one hand, the presence of submicron- and nanoscale regolith particles may act as nucleating agents during solidification, enhancing crystallinity and contributing to improved stiffness and potentially strength [188, 189]. On the other hand, increased regolith content raises the melt viscosity of the composite, making extrusion more difficult and increasing the risk of pore formation [46]. It also limits chain mobility during annealing by acting as a barrier to polymer chain movement, thereby hindering crystallization. While the potential reinforcement effects of the nanoscale particles are beneficial, the increase in porosity due to poorer flow dominates, leading to reduced tensile strength despite gains in elastic modulus.

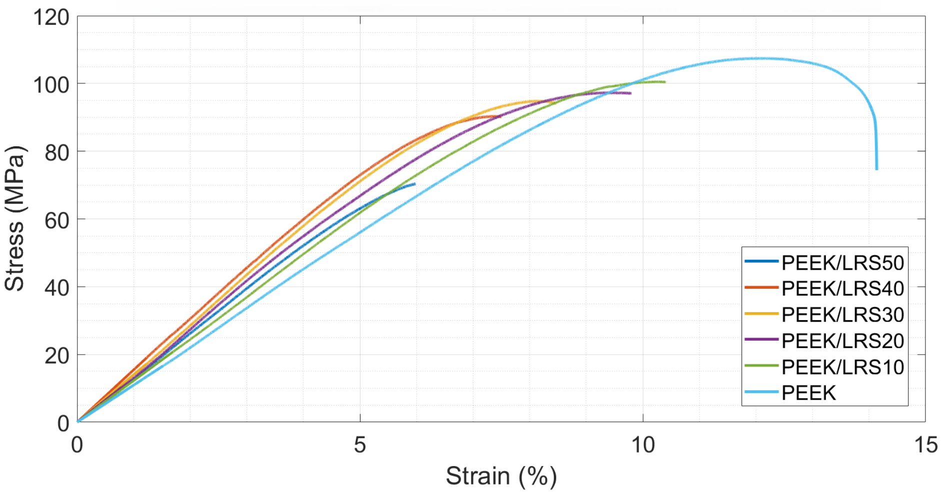

Figure 3.8: Engineering stress–strain curves for the as-printed specimens produced in this study, including neat PEEK and PEEK/LRS composites containing 10–50 wt% Lunar regolith simulant. Each curve corresponds to the specimen exhibiting the median ultimate tensile strength for its composition. The results show a progressive decrease in ductility and tensile strength and an increase in stiffness with regolith loading up to 40 wt%, followed by a marked reduction in both strength and stiffness at 50 wt%, likely due to more significant processing-induced defects at high filler contents.

One final observation concerns the fracture surface morphology. The fracture surface of pure

PEEK shows a distinct layered structure. With the addition of 10 wt% regolith particles, this layered structure becomes nearly indistinguishable, and for composites with higher filler contents, it is completely absent. This suggests a progressive improvement in interlayer bonding, which may enhance Z-direction mechanical properties. The improvement is likely due to the higher thermal conductivity of the regolith-filled composites, which promotes more uniform thermal distribution and better fusion between layers during the printing process.

As shown in Figure 3.9, following annealing, all compositions demonstrated modest yet consistent enhancements in mechanical performance, particularly in stiffness. For **neat PEEK**, the ultimate tensile strength (UTS) increased from 107.4 to 109.9 MPa, representing a 2.3% improvement, while the Young's modulus rose from 1,094.0 to 1,135.3 MPa. This corresponds to a 3.8% increase, which is a larger effect than that observed on the UTS. It should be noted that the annealed PEEK sample retained a layered structure similar to that of the as-printed sample, indicating the limited effectiveness of the annealing process in altering the microstructural morphology.

In the case of **PEEK/LRS10**, the UTS increased from 100.5 to 102.1 MPa (+1.6 %), and the modulus improved from 1225.3 to 1248.1 MPa (+1.9 %). For **PEEK/LRS20**, the UTS rose to 100.2 MPa (+3.1 %) and the modulus to 1340.5 MPa (+2.5 %). **PEEK/LRS30** experienced more modest gains, with a UTS of 96.8 MPa (+2.1 %) and a modulus of 1426.0 MPa (+1.7 %). These enhancements are primarily attributed to the reduction in processing-induced porosity during the annealing step.

The enhancements were even less pronounced for higher filler loadings. **PEEK/LRS40** exhibited a UTS of 91.5 MPa (+1.3 %) and a modulus of 1560.7 MPa (+1.0 %), while **PEEK/LRS50** showed the smallest improvements, reaching 70.9 MPa in UTS (+0.7 %) and 1278.2 MPa in modulus (+0.8 %). As anticipated from the observed changes in density and crystallinity after annealing, the mechanical benefits become limited at higher filler contents. This is primarily due to the increased prevalence of structural defects and disrupted matrix continuity, which hinder chain mobility during annealing and collectively restrict further improvements in mechanical performance.

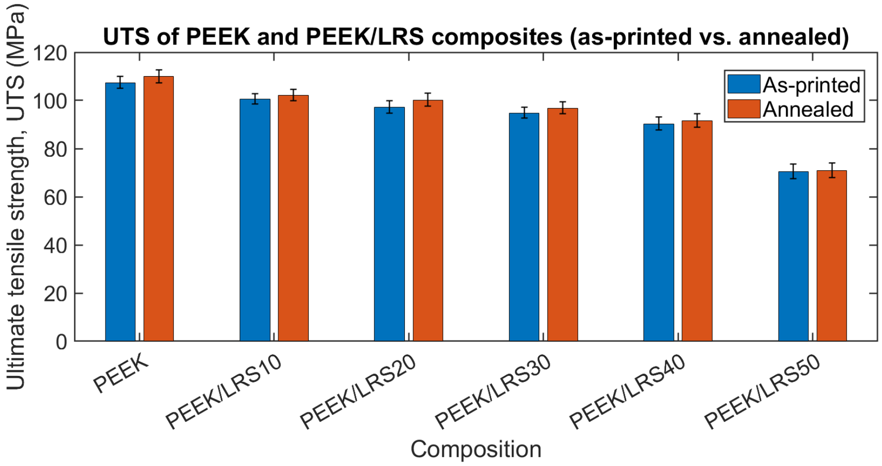

(a) Ultimate tensile strength (UTS) of as-printed and annealed samples.

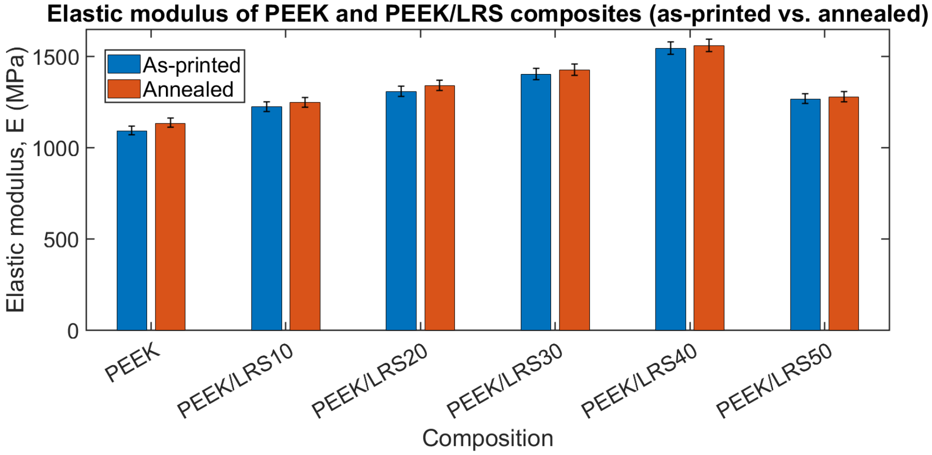

(b) Young's modulus (E) of as-printed and annealed samples.

Figure 3.9: Comparison of mechanical properties for as-printed and annealed specimens, including (a) ultimate tensile strength (UTS) and (b) Young's modulus. All compositions exhibit modest improvements after annealing, with the most pronounced gains observed in neat PEEK and composites containing up to 30 wt% regolith. At higher filler contents, the benefits of annealing diminish, likely due to increased structural defects and reduced matrix continuity, which limit further enhancement of mechanical performance.

3.3.7 Microstructural analysis

Scanning electron microscopy (SEM)

Backscattered electron (BSE) SEM micrographs of polished cross-sections are obtained for filaments and the as-printed samples with median UTS from the second phase. These micrographs appear to be consistent with the reduction in mechanical performance observed in tensile testing with increasing regolith particle concentration. As the regolith content increases, a corresponding rise in defect incidence is observed.

Figure 3.10a presents the microstructure of the neat PEEK filament, which appears nearly defect-free. In contrast, Figure 3.10b shows the cross-section of an as-printed PEEK sample. No significant defects are observed within individual layers; however, visible interlayer gaps are present, which are characteristic of the layer-by-layer deposition inherent to the MEX process. This morphological observation is consistent with the fracture behavior seen during tensile testing. Fracture surfaces of neat PEEK specimens reveal a distinctly layer-controlled failure mode. Cracks typically initiate at the interlayer interfaces and propagate as planar segments oriented perpendicular to the loading direction. However, rather than forming a continuous break across the specimen width, the fracture surface often appears stepped, with adjacent layers failing at different positions along the gauge length. This staggered rupture pattern may indicate non-uniform stress transfer across layers, resulting from limited polymer chain diffusion and insufficient interlayer entanglement during printing. Notably, despite achieving near-full bulk density ($> 99\%$) as measured by the Archimedean method, the interlayer regions appear to remain mechanically weak. Cracks tend to initiate and propagate along these interfaces under tensile loading or during post-fracture handling (e.g., cutting), underscoring the pronounced anisotropy inherent to MEX-processed PEEK.

The addition of LRS significantly alters the fracture behavior of the printed composites. Even at the lowest filler content investigated (PEEK/LRS10), the fracture path propagates uniformly across the specimen width and occurs nearly in the same plane perpendicular to the tensile loading direction, cutting through multiple printed layers rather than varying in position from layer to layer. SEM analysis of the fracture cross-sections (Figures 3.11a and 3.11b) reveals no discernible interlayer boundaries, indicating a potential improvement in interlayer cohesion. This behavior suggests

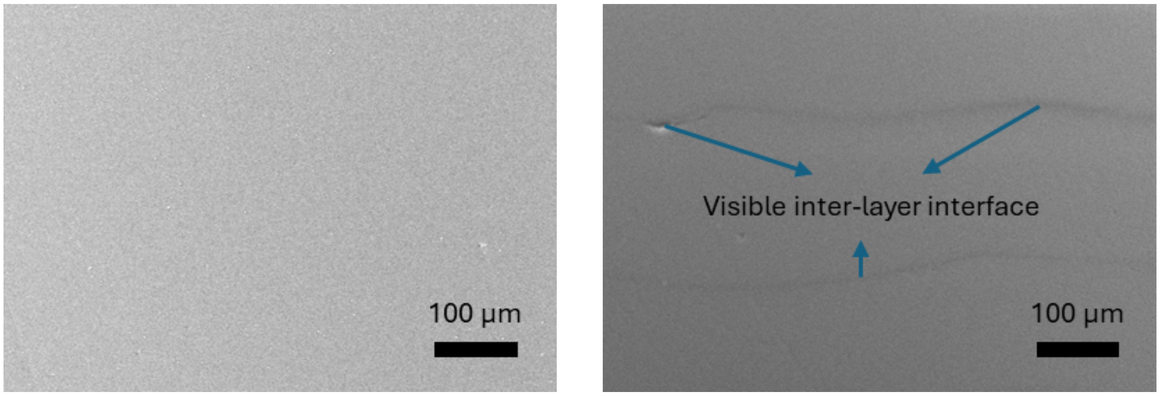

(a) Neat PEEK filament. (b) As-printed PEEK sample.

Figure 3.10: (a) Microstructure of the neat PEEK filament prior to printing. (b) Cross-section of the as-printed PEEK sample, where the interlayer boundary is clearly visible as a result of the layer-by-layer deposition process.

improved material integrity and interlayer bonding, even at modest regolith loadings. Two key mechanisms may contribute to this altered failure mode. First, **particle-mediated stress redistribution**: the rigid ceramic particles could promote mechanical bridging across adjacent rasters, enabling localized stress transfer between layers. As a result, crack fronts may be forced to deflect or branch, increasing the fracture surface area and improving the effective interlayer fracture toughness. Second, **crystallization inhibition and thermal stress relaxation**: the presence of regolith particles during PEEK solidification may disrupt spherulite growth, thereby reducing residual shrinkage stresses between layers. Although the thermal conductivity of the regolith is lower than that of metals, it remains significantly higher than that of polymers. This enhanced thermal conductivity could facilitate better heat dissipation during printing, reduce thermal gradients, and minimize residual stresses that might arise from differential cooling.

The transition in fracture morphology is further supported by the observed increase in elastic modulus with increasing regolith content (up to 40 wt%), despite reductions in ultimate tensile strength. These findings may suggest that particle-induced stiffening and improved resistance to interlayer crack propagation can partially compensate for the brittleness introduced by the ceramic filler.

SEM micrographs of the as-printed PEEK/LRS10 sample (Figures 3.11a and 3.11b) reveal a

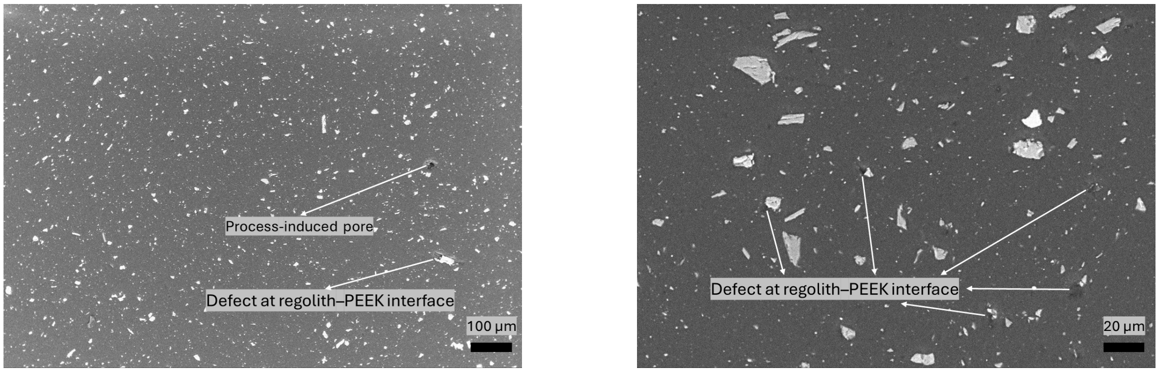

(a) PEEK/LRS10 (100×).

(b) PEEK/LRS10 (500×).

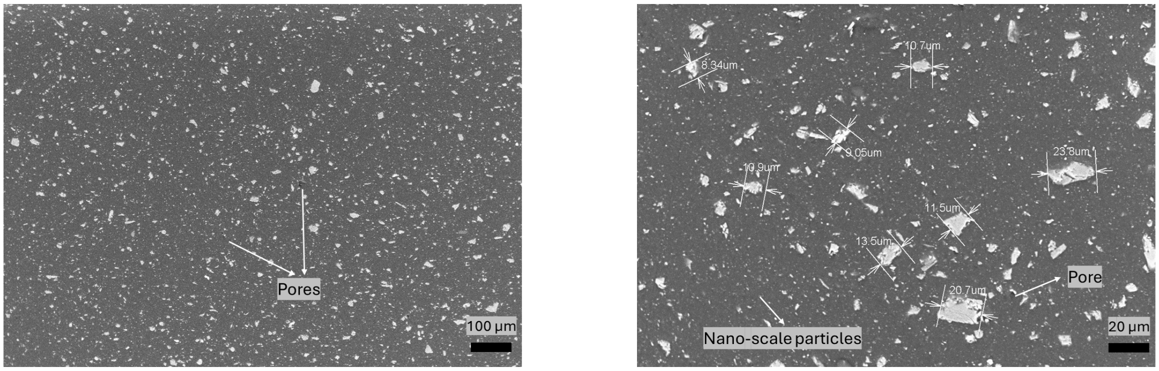

(c) PEEK/LRS20 (100×).

(d) PEEK/LRS20 (500×).

Figure 3.11: Backscattered SEM micrographs of polished cross-sections of as-printed PEEK/regolith composites. (a, b) PEEK/LRS10 and (c, d) PEEK/LRS20 at 100× and 500× magnifications, respectively. Both compositions exhibit uniform particle dispersion and low pore density, with no evidence of particle agglomeration and no resolvable interlayer boundaries, indicating good interlayer cohesion and effective mixing during compounding and extrusion.

uniform and randomly distributed dispersion of regolith particles within the PEEK matrix, demonstrating the effectiveness of the compounding and filament extrusion process. The observed process-induced pores are relatively small, typically less than 5 µm in diameter, and are predominantly located near regolith particles. This spatial correlation suggests that pore formation may result from incomplete particle–matrix wetting or localized thermal shrinkage mismatch during solidification, leading to microvoid nucleation at the particle–polymer interface.

SEM micrographs of the PEEK/LRS20 composite (Figures 3.11c and 3.11d) reveal microstructural characteristics similar to those observed in the PEEK/LRS10 formulation. The pore population remains relatively low, with small and sparsely distributed voids consistent with the 2.4 % porosity measured via the Archimedean method. Notably, the increased regolith content does not lead to particle agglomeration; individual regolith grains remain well dispersed throughout the matrix, and their maximum observed diameter aligns with the nominal particle size distribution (PSD) of the LRS feedstock. At 500× magnification (Figure 3.11d), sub-micron-scale fragments are also visible, likely corresponding to the fine tail of the PSD, further supporting the conclusion that the mixing and extrusion process can achieve uniform dispersion without particle segregation.

An increase in pore density is observed when transitioning from PEEK/LRS20 to PEEK/LRS30, as evident in Figures 3.11d and 3.12d. This microstructural change is consistent with a 1.4 percentage point decrease in relative density, as determined by the Archimedean method, and a corresponding 2.5% reduction in ultimate tensile strength (UTS), from 97.2 MPa to 94.8 MPa. Despite the increased filler content, no particle agglomeration is observed, and the regolith remains well-dispersed throughout the matrix.

Furthermore, SEM micrographs appear to reinforce the mechanical performance improvements achieved in the present study relative to those reported in Phase I [4]. As shown in Figure 3.12, the PEEK/LRS30 specimens fabricated in the current work exhibit visibly fewer and smaller defects compared to those from the previous study. This notable microstructural refinement is consistent with a significant increase in UTS (from 67.1 MPa to 94.8 MPa), highlighting the effectiveness of the optimized processing conditions employed in this work.

As shown in Figure 3.13, BSE–SEM micrographs of the PEEK/LRS40 and PEEK/LRS50 filaments reveal only minor differences in defect density and pore size between the two compositions.

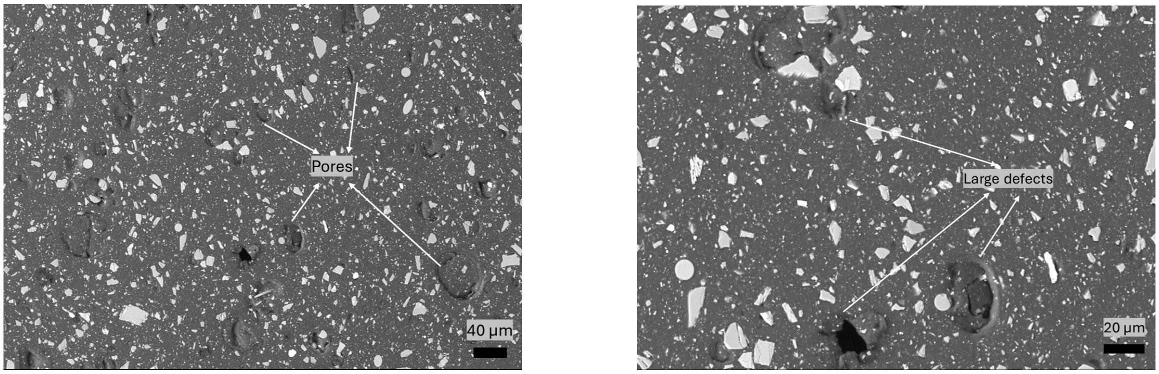

(a) Phase I [4], PEEK/LRS30 (200×).

(b) Phase I [4], PEEK/LRS30 (500×).

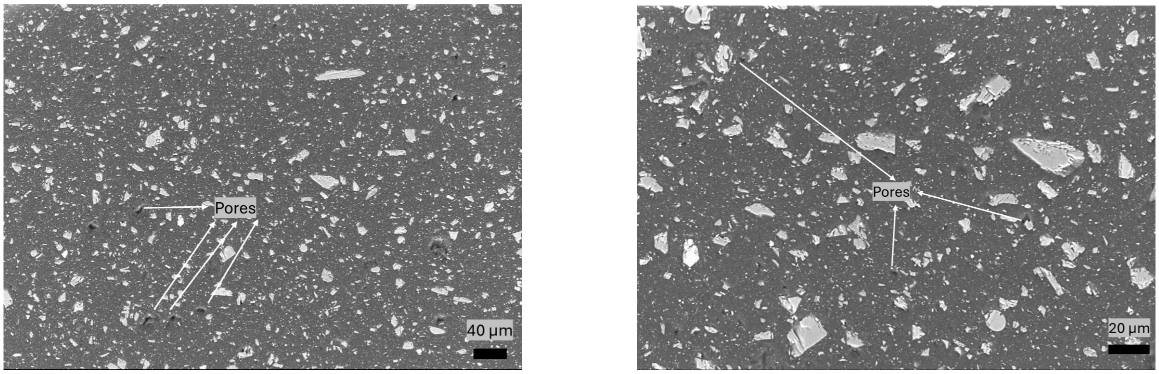

(c) This work (Phase II), PEEK/LRS30 (200×).

(d) This work (Phase II), PEEK/LRS30 (500×).

Figure 3.12: Comparison of backscattered SEM micrographs of polished cross-sections of as-printed PEEK/LRS30 composites from Phase I [4] and the current work (Phase II). (a, b) Micrographs from Phase I at 200× and 500× magnifications show larger and more numerous defects. (c, d) Corresponding images from the present phase demonstrate a substantially refined microstructure, with fewer and smaller pores, reflecting improvements in extrusion quality and printing parameters.

This observation is supported by Archimedean porosity measurements, which show just a 1.3 percentage point decrease in porosity when increasing the regolith content from 40 to 50 wt%. However, the PEEK/LRS50 filament exhibits a noticeably rougher surface, likely due to the higher melt viscosity of the composite at elevated filler loadings. The increased regolith content also makes the filament more brittle, consistent with its higher ceramic fraction.

Figures 3.14a and 3.14b present SEM micrographs of the as-printed PEEK/LRS40 sample. A gradual increase in both pore number and size is evident in samples ranging from neat PEEK to PEEK/LRS40, aligning well with the trends observed in porosity and mechanical performance based on Archimedean and tensile test results, respectively.

In contrast to the relatively small changes observed in the filaments (Figure 3.13), SEM images of the corresponding as-printed samples (Figure 3.14) display a pronounced increase in both the density and size of defects when the regolith content is raised from 40 to 50 wt%. This microstructural deterioration is consistent with the 2.6 percentage point increase in porosity observed via the Archimedean method and corresponds with the measured decline in mechanical properties at higher regolith loadings.

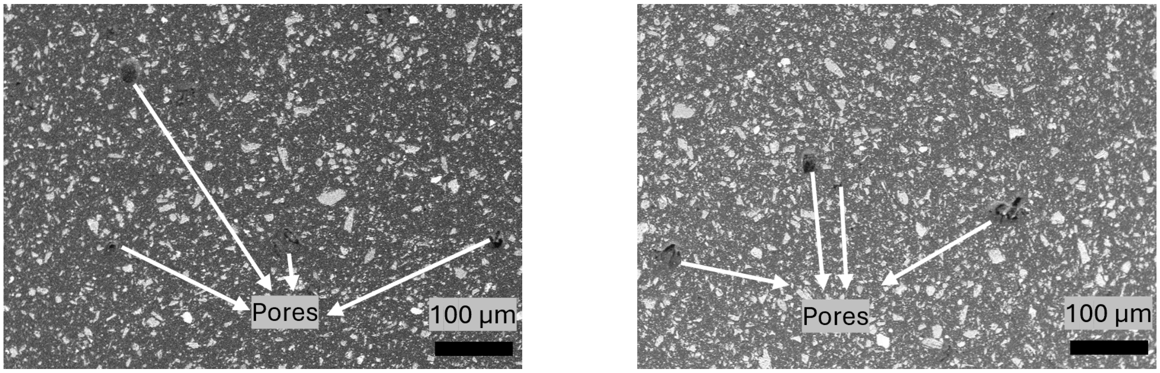

(a) PEEK/LRS40 filament.

(b) PEEK/LRS50 filament.

Figure 3.13: Backscattered SEM micrographs of extruded filament cross-sections for (a) PEEK/LRS40 and (b) PEEK/LRS50. Both compositions exhibit similar internal pore densities, consistent with Archimedean measurements. At 50 wt% regolith, the filament displays a rougher surface and increased brittleness due to the higher ceramic fraction and elevated melt viscosity during extrusion.

All SEM analyses in this study were conducted on the fracture surfaces of the extruded filaments and as-printed specimens. Although a limited set of annealing experiments was conducted to

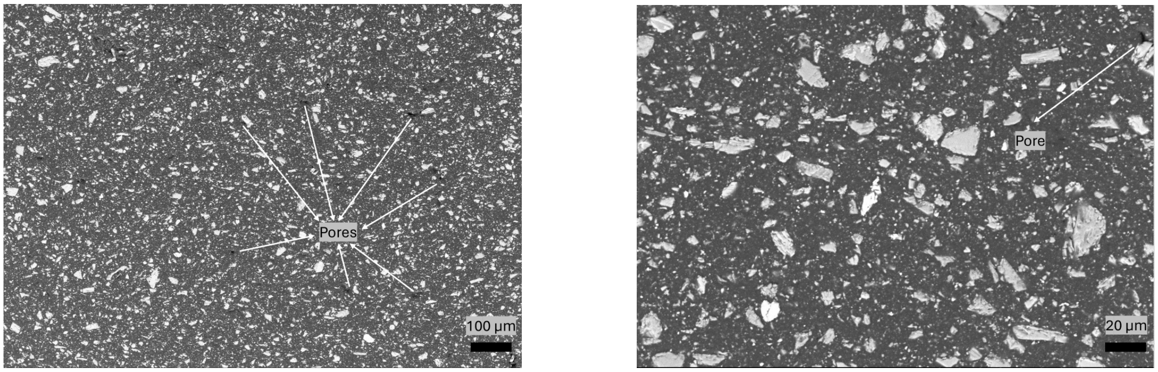

(a) PEEK/LRS40 as-printed (100×). (b) PEEK/LRS40 as-printed (500×).

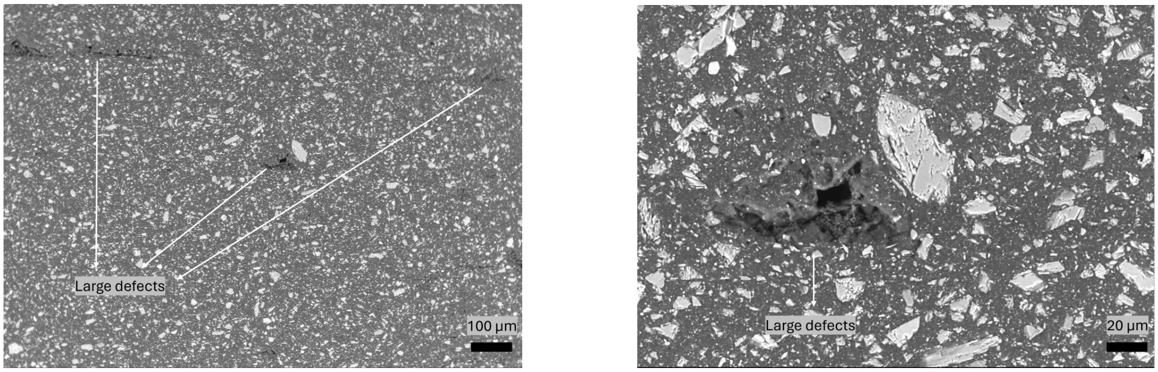

(c) PEEK/LRS50 as-printed (100×). (d) PEEK/LRS50 as-printed (500×).

Figure 3.14: Backscattered SEM micrographs of polished cross-sections of as-printed composites: (a, b) PEEK/LRS40 and (c, d) PEEK/LRS50 at 100× and 500× magnifications. A notable increase in pore density and defect size is observed when the regolith content increases from 40 to 50 wt%, consistent with the higher porosity and reduced mechanical properties measured for PEEK/LRS50.

evaluate crystallinity gains and defect closure, the primary focus of this work remains on as-printed properties. This choice is deliberate and grounded in practical constraints specific to space-based ISRU manufacturing.

First, annealing introduces an additional thermal cycle that runs counter to the ISRU objectives of minimizing operational complexity, energy consumption, and processing time. Transporting an oven to the Moon incurs significant cost and logistical challenges. Printing 1 kg of PEEK typically consumes 1–5 kWh depending on printing parameters, whereas heating and maintaining a well-insulated 30 × 30 × 30 cm oven at 300°C for a 2-hour annealing cycle requires approximately 5 kWh, placing the annealing energy demand within the same range or potentially exceeding the energy required for printing alone. For off-Earth manufacturing systems, where power and time are highly constrained, this extra step, along with the necessary hardware and energy expenditure, represents an inefficient overhead. From a system-level perspective, the added equipment, extended processing time, and substantial energy demands are difficult to justify given the relatively marginal mechanical property improvements achieved through annealing.

Second, repeated thermal exposure can negatively affect the long-term durability and reusability of thermoplastic components. PEEK is susceptible to molecular chain scission and oxidative degradation under extended or repeated high-temperature cycles [203, 204]. For ISRU applications, where components may be repurposed, repaired, or recycled across multiple mission cycles, limiting cumulative thermal history helps preserve performance and extend material service life.

Third, and most critically, the mechanical and densification benefits of annealing diminish substantially at higher regolith contents. As detailed in Table 3.3, annealing almost fully eliminated residual porosity in neat PEEK and composites up to 20 wt% regolith. However, for 30–50 wt% formulations, the relative density gains were minimal (typically less than 1 %) and produced negligible improvements in tensile strength. These high regolith loadings are the most relevant for ISRU, as they most significantly reduce the amount of imported PEEK required. For example, composites with 50 wt% regolith content halve the mass of polymer needed, which is a key advantage in logistics-constrained environments. At these concentrations, porosity and interlayer defects become the dominant limiting factors while annealing offers little remediation. Conversely, for regolith contents up to 30–40 wt%, the as-printed quality already seems to be sufficient for many aerospace structures, with only slightly lower mechanical performance compared to post-process annealed parts.

Elemental composition characterization

Energy-dispersive X-ray spectroscopy (EDS) was performed at the nine labelled sites shown in Figure 3.15, and the corresponding elemental compositions are summarized in Table 3.4. Elemental distribution maps further illustrate, in line with the SEM data, that the regolith particles are dispersed randomly and uniformly throughout the matrix, highlighting the consistency of the material's microstructure.

Matrix locations (Points 1 and 9). These regions exhibited high carbon (74–79 wt%) and oxygen (18–24 wt%) content, with only trace amounts of metals. This composition is consistent with the polymer matrix, confirming that these points are located within the PEEK phase. Minor elements such as Si, Na, and Fe were detected at levels below 1.5 wt%, likely attributable to surface contamination or polishing debris.

Mg–Si-rich silicates (Points 2 and 3). These inclusions were dominated by oxygen (60–63 wt%), magnesium (13–15 wt%), and silicon (18–20 wt%), along with minor iron (2–3 wt%). Such a composition suggests the presence of pyroxene or olivine fragments, commonly found in regolith simulants.

Na–Al–Ca feldspathic particles (Points 4 and 5). These sites contained oxygen concentrations around 63 wt%, along with notable amounts of Na (1.6–2.7 wt%), Al (11–12 wt%), Si (17–18 wt%), and Ca (4–5 wt%). The overall chemistry aligns with plagioclase-type feldspars ranging from sodic to calcic composition.

Ti-bearing oxide inclusions (Points 6 and 8). These regions were characterized by high oxygen content (73–75 wt%) and elevated titanium (13–14 wt%), along with iron (6–9 wt%), and minor amounts of Mg, Si, and Mn. This composition is typical of ilmenite-like phases, frequently observed in Lunar regolith.

Fe-rich inclusion (Point 7). This point revealed an exceptionally high iron content (48.7 wt%), with reduced oxygen (35.6 wt%), accompanied by Mg, Si, and minor Ti and Al. The data indicate a dense iron oxide such as magnetite.

In summary, the EDS results effectively distinguish the carbon-rich PEEK matrix from the oxide-based regolith particles, while also highlighting the chemical heterogeneity of the filler phase. The identified phases include Mg–Si silicates, feldspathic materials, ilmenite, and Fe-rich inclusions, all of which are representative of the complex oxide distribution expected in Lunar regolith simulants. These findings have direct implications for the thermal, mechanical, and interfacial behavior of the composite.

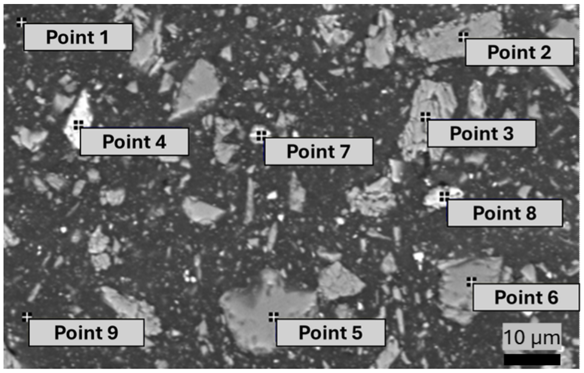

Figure 3.15: Backscattered SEM micrograph of the PEEK/LRS50 composite showing the nine locations selected for EDS point analysis. Points 1 and 9 correspond to the PEEK matrix, while the remaining points represent distinct regolith particles exhibiting varied oxide chemistries characteristic of Mg–Si silicates, feldspathic phases, Ti–Fe oxides, and Fe-rich inclusions.

Table 3.4: Elemental composition (wt%) at the nine EDS acquisition points shown in Fig. 3.15.

Point	**C**	**O**	**Na**	**Mg**	**Al**	**Si**	**Ca**	**Ti**	**Mn**	**Fe**
Point 1	73.64	23.66	0.19	0.56	0.37	1.27	0.16	0.16	–	–
Point 2	–	63.44	–	13.08	0.94	18.28	2.04	–	–	2.21
Point 3	–	60.36	–	14.81	1.02	20.21	0.64	–	–	2.97
Point 4	–	62.94	1.64	0.48	12.12	17.62	5.20	–	–	–
Point 5	–	63.62	2.73	0.53	11.24	17.85	4.04	–	–	–
Point 6	–	72.82	–	1.05	0.73	1.84	0.54	13.05	0.74	9.24
Point 7	–	35.57	–	5.48	1.57	6.76	0.82	1.10	–	48.69
Point 8	–	74.62	–	1.64	0.91	1.95	–	13.50	0.65	6.73
Point 9	78.72	18.20	–	1.22	0.25	1.39	–	–	–	0.22

Figure 3.16 presents a BSE SEM overview (upper-left) together with quantitative X-ray maps for the principal elements detected. A clear two-phase architecture emerges:

Carbon map. A bright, continuous signal outlines the polymer phase, while angular and rounded voids correspond to the locations of regolith particles. This contrast is consistent with carbon being predominantly confined to the PEEK matrix.

Oxygen map. Oxygen is broadly distributed, with the highest intensity observed in the carbon-deficient regions, which appears to highlight the oxide-rich nature of the filler particles. In contrast, the matrix shows a lower oxygen signal.

Silicon and aluminum maps. Silicon exhibits strong and widespread contrast across nearly all regolith inclusions, while aluminum is concentrated in a subset of these Si-bearing regions. Their co-localization is characteristic of feldspathic silicates (e.g., Na- or Ca-rich plagioclase) and is consistent with the earlier point analyses.

Magnesium map. Magnesium appears in discrete, elongated clusters that coincide with the Mg–Si-enriched domains identified in Table 3.4 (Points 2 and 3). These areas can be interpreted as fragments of, or at least are compatible with, Mg-rich pyroxene or olivine.

Titanium and iron maps. Titanium shows a sparse distribution of bright pixels that often coincide with intense iron signals, suggesting the presence of Ti–Fe oxides such as ilmenite. Several areas exhibit strong iron with negligible titanium, in line with the Fe-rich particle observed at Point 7 in Figure 3.15.

Calcium, sodium, and potassium maps. Calcium is localized within a limited number of grains and commonly co-occurs with silicon and aluminum, suggesting the presence of, or at least compatibility with, calcic plagioclase. Sodium and potassium appear as weak, diffuse signals, broadly following the feldspathic regions. Their low intensity is in good agreement with the quantitative point spectra.

To summarize, the elemental maps are broadly consistent with the EDS point analysis: (i) the carbon-rich continuous phase is most reasonably interpreted as PEEK, and (ii) the embedded filler phase appears to consist of a chemically heterogeneous mixture of feldspathic materials, Mg-silicates, Ti–Fe oxides, and isolated Fe-rich particles. This compositional diversity, clearly visualized in the X-ray maps, is consistent with the mineralogical complexity of the Lunar regolith simulant and with the pronounced matrix–filler contrast that is expected to govern local thermal and mechanical behavior.

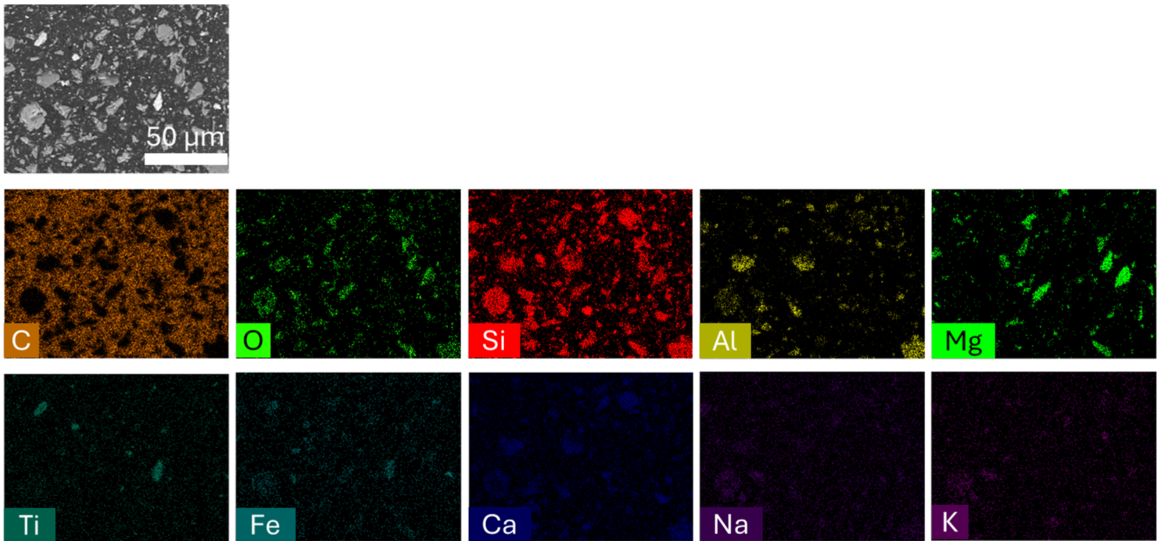

Figure 3.16: Backscattered electron SEM micrograph (a) and EDS X-ray maps of the as-printed PEEK/LRS50 composite acquired using C K_α, O-K_α, Al-K_α, Na-K_α, Mg-K_α, Si-K_α, Ca-K_α, Ti-K_α, Fe-K_α, and K-K_α radiations. The maps corroborate the point-analysis data, delineating the carbon-rich PEEK matrix from oxide-based regolith particles and highlighting the heterogeneous distribution of feldspathic, Mg–silicate, Ti–Fe oxide, and Fe-rich phases.

3.4 Conclusion and future work

This phase of the study demonstrates the material extrusion (MEX) additive manufacturing of polyether–ether–ketone (PEEK) and its composites containing 10–50 wt% Lunar regolith simulant (LRS), addressing key challenges in developing ISRU-compatible structural materials for Lunar infrastructure. Filaments were produced via twin-screw extrusion, printed in a high-temperature chamber, and post-processed by annealing at 300 °C. The resulting composites were systematically evaluated in terms of density, crystallinity, mechanical performance, and microstructural characteristics.

The main findings are as follows:

- *Processability:* All filament compositions achieved densities above 96%. However, as-printed porosity rose from under 1% in neat PEEK to 7.5% at 50 wt% LRS due to increased melt viscosity. A practical printability limit of 40 wt% LRS is identified for mechanically critical parts, while 50 wt% remains viable for non-load-bearing or secondary structures. LRS incorporation and the use of a PEKK raft reduced delamination and warping, leading to improved dimensional accuracy and higher print success rates compared to pure PEEK.

- *Thermal and mechanical performance:* Regolith addition increased matrix crystallinity from 17.4 % to 20.5 %, and enhanced the elastic modulus by 6–41 %. Tensile strength declined steadily from 107 MPa for neat PEEK to 90 MPa at 40 wt% LRS, followed by a sharper reduction to approximately 70 MPa at 50 wt%.

- *Post-processing response:* Furnace annealing improved both density and stiffness in composites containing up to 30 wt% LRS. Above this threshold, gains were minimal, likely due to entrapped porosity, indicating the need for advanced post-processing methods at higher filler contents.

- *Microstructural integrity:* Scanning electron microscopy (SEM) and energy-dispersive spectroscopy (EDS) revealed a carbon-rich PEEK matrix with uniformly dispersed regolith particles. The detected fillers included feldspathic, Mg-silicate, Ti–Fe oxide, and Fe-rich phases, confirming effective mixing and good phase contrast.

Overall, the results define a viable processing window for regolith-filled thermoplastic composites, with 40 wt% LRS representing an important trade-off point balancing between mechanical performance and reduction in Earth-derived material. At 50 wt%, the composite remains printable and structurally coherent, offering potential for non-critical or shielding applications where high stiffness is valued over strength.

Future work should focus on extending the printing process to simulated vacuum and low-gravity environments, exploring additional Lunar regolith simulants and alternative high-performance polymers, and integrating finite element simulation to model material flow and stress evolution. Further studies are also needed to assess durability under Lunar-relevant thermal cycling, radiation exposure, and micrometeoroid impacts. Scaling up to robotic, large-format extrusion systems will be critical for enabling autonomous, ISRU-driven additive manufacturing for long-duration Lunar operations.

Chapter 4

Phase III: Finite-Element Analysis of Additively Manufactured PEEK–Regolith Composites

4.1 Motivation

A rigorous understanding of the intrinsic capability of PEEK–regolith composites is essential to distinguish composition-driven behavior from performance losses caused by manufacturing defects. Without a defect-free reference, measured stiffness and strength conflate the effects of regolith loading with porosity, weak interlayer welds, and particle–matrix debonding, obscuring clear guidance for process optimization and design allowables. To address this, we used finite-element analysis to establish an upper-bound (defect-free) response for compositions spanning 10–50 wt% regolith in 10% increments, mirroring the experimental matrix. We then incorporated imaging-derived porosity fields and representative interfacial flaws to quantify the shortfalls attributable to the specific defects. This framework isolates true material potential, identifies the effect of defects, and defines actionable targets to close the gap between printed parts and their defect-free limits.

4.2 Methodology

The first step is to create a material model with varying regolith contents that includes both the matrix and particles while excluding structural defects. This establishes the idealized mechanical potential under flawless conditions. A representative volume element (RVE) of the composite is generated in CAD, followed by assignment of boundary conditions and material properties. The RVE is meshed and subjected to uniaxial tension at a constant nominal strain rate, mirroring the experimental setup to characterize elastic behavior. Plastic deformation is outside the scope of this study; we focus on the elastic regime to determine Young's modulus.

The analysis of idealized PEEK–regolith composites involves simplifying assumptions to keep the problem computationally tractable. First, additive manufacturing process effects are neglected; in particular, anisotropy and inhomogeneity from layer-by-layer fabrication are ignored, and the material is treated as isotropic and homogeneous. Second, the semi-crystalline nature of PEEK is simplified by neglecting spatial variations in crystallinity between amorphous and fully crystallized regions. Third, the morphology of regolith particles is idealized as random polygons, despite their inherently irregular shapes. Fourth, each particle is treated as homogeneous with a single effective (composition-averaged) elastic modulus, while in reality, regolith grains are multiphase aggregates with spatially varying properties. Finally, nanoscale effects are excluded because continuum finite element tools such as ABAQUS and ANSYS cannot capture quantum-scale interactions or surface-dominated phenomena. These assumptions enable practical modeling but limit fidelity to real composite behavior.

Two-dimensional (2D) modeling is adopted as the most practical approach. The high particle count, complex morphologies, and broad size distribution render 3D models computationally prohibitive; trial runs show that a $4 \times 4 \times 4$ mm RVE produces CAD files on the order of tens of gigabytes, exceeding available resources. This choice is justified on two grounds. First, scanning electron microscopy indicates a reasonably homogeneous particle distribution, so an in-plane representation captures the essential microstructural statistics for elastic response. Second, the elastic tensile behavior of interest is well represented by planar stress–strain relationships; out-of-plane interactions and plasticity are not analyzed here, so a 3D model would add cost without commensurate insight. The 2D approach therefore balances computational efficiency with the study objectives.

Generating CAD models of the particles. The particulate geometry is generated with a MATLAB script. We first construct a 3D stochastic RVE populated with non-overlapping particles, then extract a 2D mid–plane section to obtain the planar CAD used for analysis. Under standard stereological assumptions, the areal fraction measured in the 2D section provides an unbiased estimate of the 3D particle volume fraction. User inputs include the maximum particle size, the matrix (RVE) dimensions, and the target particle volume fraction.

For robust control of volume fraction we seed the 3D RVE with *spherical* particles and later replace each sphere by a cube having the same circumscribed diameter. If the diameter of the (temporary) sphere is d, the edge length of the cube is $a = d/\sqrt{3}$ (since the circumscribed sphere of a cube has diameter $a\sqrt{3}$). The corresponding single-particle volumes are

$$Volume_{\text{sphere}} = \frac{\pi}{6}d^3, \qquad Volume_{\text{cube}} = a^3 = \frac{d^3}{3\sqrt{3}},$$

so that

$$\frac{Volume_{\text{cube}}}{Volume_{\text{sphere}}} = \frac{2}{\pi\sqrt{3}}.$$

Hence, to achieve a desired *cubic* particle volume fraction V_{cube} in the final model, the temporary *spherical* packing fraction $V_{\circ}$ used during seeding must be scaled as

$$V_{\circ} = \frac{\pi\sqrt{3}}{2} V_{\text{cube}}.$$

The script first places spherical particles at random locations with randomly assigned radii, performing collision checks after each placement and discarding overlaps. As the cumulative particle volume approaches the target, the particle size is adjusted via a prescribed relation to match the LMS-1D particle size distribution. Once the target volume fraction is reached, particle generation stops and three random rotation angles are assigned to each particle.

A second script then checks for intersections with an XY plane through the matrix and writes only the intersecting particles to an OPENSCAD script. OPENSCAD renders cubes with the assigned rotations applied, inscribed within the spheres using the stored parameters.

After defining all particles, a 2D section is taken along the central XY plane of the matrix. This section is saved as a `.dxf` file representing the particles. The script is then rerun with a subtraction operation to generate the complementary matrix geometry, also saved as a `.dxf`.

Under standard stereological assumptions, the areal fraction measured in the 2D section provides an unbiased estimate of the 3D particle volume fraction. This procedure is effective because the target particle volume fraction is first enforced in 3D, and the subsequent mid–plane cut yields a 2D areal fraction that is representative of the true regolith content.

These sketches are imported into ABAQUS to create individual parts, assign materials, and assemble the 2D matrix–particle system. The next sections describe how the input parameters required for simulation are extracted, calculated, or estimated.

4.3 Composite Density Estimation and Regolith Characterization

The LMS-1D datasheet (Exolith Lab, USA) reports two densities: (i) the uncompressed bulk density of loose simulant, which includes inter-particle voids (0.70 g/cm^3), and (ii) a particle density measured by Archimedean displacement in water (2.92 g/cm^3). Neither value is suitable for finite-element inputs in PEEK–regolith composites. The bulk value reflects packing voids rather than the solid phase. The Archimedean value likely overestimates the effective regolith phase density in PEEK because water penetrates open porosity and surface asperities that molten PEEK (high viscosity, different wetting) does not fill during processing. Neither reconciles with the composite densities obtained via the Archimedean displacement method when combined with the known density of PEEK and the pore fraction estimated from micrographs.

This section therefore, estimates the true particle-phase density and the porosity-free (dense) composite density by combining mass–volume measurements, image-based porosity quantification, and back-calculations across compositions.

Regolith simulant composition

Lunar regolith simulant consists of several oxide phases. Based on the fact sheet, the weight percentages for LMS-1D [5] closely resemble those presented in Table 4.1.

Table 4.1: Weight fractions of different oxides in the material composition [5].

Oxide	**Weight Fraction W_i (%)**
SiO_2 (Silica)	46.9
TiO_2 (Rutile)	3.6
Al_2O_3 (Alumina)	12.4
FeO (Wüstite)	8.6
MnO (Manganosite)	0.2
MgO (Periclase)	16.8
CaO (Lime)	7.0
Na_2O (Sodium Oxide)	1.7
K_2O (Potassium Oxide)	0.7
P_2O_5 (Phosphorus Pentoxide)	0.2

Densities of Oxides (g/cm^3)

Table 4.2 summarizes room–temperature densities for the relevant oxide constituents used in our calculations. Values are taken from standard handbooks and compilations [6–9], where available.

Table 4.2: Density of each oxide [6–9].

Oxide	ρ_i **(g/cm^3)**
SiO_2 (Silica)	2.65
TiO_2 (Rutile)	4.23
Al_2O_3 (Alumina)	3.97
FeO (Wüstite)	5.7
MnO (Manganosite)	5.4
MgO (Periclase)	3.58
CaO (Lime)	3.34
Na_2O (Sodium Oxide)	2.27
K_2O (Potassium Oxide)	2.43
P_2O_5 (Phosphorus Pentoxide)	2.39

Estimation of regolith solid density

To estimate the solid density, we use the equation:

$$\frac{1}{\rho_{\text{regolith}}} = \sum \frac{W_i}{\rho_i} \tag{2}$$

where:

- W_i is the weight fraction of each oxide,
- ρ_i is the density of each oxide.

Assuming no intermediate compositions and ignoring ionic bonding effects, the estimated density of regolith is:

$$\rho_{\text{regolith}} \approx 3.15 \text{ g/cm}^3 \tag{3}$$

4.3.1 Image-Based Porosity Estimation

A backscattered electron (BSE) SEM image of the PEEK–regolith composite filament is processed to estimate porosity. Using grayscale thresholding and circular masking, the porosity is found to be approximately 1.45%. The measured density of the 40 wt% regolith composite is 1.623 g/cm^3.

Correcting for the porosity using:

$$\rho_{\text{dense}} = \frac{\rho_{\text{measured}}}{1 - \phi_{\text{composite}}} = \frac{1.623}{1 - 0.0145} = 1.6469\ \text{g/cm}^3 \approx 1.647\ \text{g/cm}^3. \tag{4}$$

4.3.2 Back-Calculation of Regolith Density

Assuming PEEK has a density of 1.30 g/cm^3 and that the composite contains 40 wt% regolith, the back-calculated (bulk) density of the regolith phase is 2.77 g/cm^3. If the fully dense (pore-free) regolith has a true density of 3.15 g/cm^3 (see above), the intra-particle porosity of the regolith phase ϕ and the corresponding density correction are

$$\phi_{\text{regolith phase}} \;=\; \frac{\rho_{\text{true}} - \rho_{\text{bulk}}}{\rho_{\text{true}}} \;=\; \frac{3.15 - 2.77}{3.15} \;\approx\; 0.121\ (12.1\%). \tag{5}$$

This indicates that the regolith phase contains approximately 12.1% porosity.

4.3.3 Dense Composite Density Calculation

Using the regolith phase density (2.77 g/cm^3) and PEEK density (1.30 g/cm^3), the following table presents the calculated dense composite densities for varying regolith weight fractions:

Table 4.3: Calculated dense composite densities using regolith phase density (2.77 g/cm^3) and PEEK density (1.30 g/cm^3).

Regolith wt%	**Composite Density (g/cm^3)**
10	1.373
20	1.454
30	1.546
40	1.650
50	1.770

4.4 Young's Modulus of LMS-1D: Calculation Using Voigt and Reuss Models

We do not have direct access to the Young's modulus of the regolith particles, either for the bulk material or for individual grains. Moreover, regolith grains are multiphase aggregates with spatially varying properties. For simplicity, each particle is treated as homogeneous with a single, composition-averaged elastic modulus. This assumption is reasonable because our experimental measurements provide bulk moduli at the composite scale, and our goal is to bound effective behavior rather than resolve intragrain heterogeneity. The effective mechanical properties of the regolith particle phase are estimated using classical bounds, primarily the Voigt (iso-strain) [205] upper bound and the Reuss (iso-stress) [206] lower bound, which relate the effective Young's modulus to phase properties and volume fractions.

Voigt upper bound. The Voigt model assumes all phases experience the same strain (parallel arrangement), giving:

$$E_{\text{upper}} = \sum_i V_i E_i, \quad \text{[Voigt; 205]} \tag{6}$$

Reuss lower bound. The Reuss model assumes all phases experience the same stress (series arrangement), yielding:

$$\frac{1}{E_{\text{lower}}} = \sum_i \frac{V_i}{E_i}, \quad \text{[Reuss; 206]} \tag{7}$$

Effect of Porosity: Accurate estimation of E_{eff} is essential when comparing defect-free Voigt/Reuss bounds to measured moduli in materials with complex internal porosity. In practical materials, porosity can significantly reduce the effective Young's modulus, as pores act as stress concentrators and limit the material's load-bearing capacity. This mechanical degradation is commonly captured using the following empirical relation:

$$E_{\text{eff}} = E_0 \big(1 - a\phi\big)^n \quad \text{[207, 208]}, \tag{8}$$

where E_0 is the Young's modulus of the fully dense material, ϕ is the porosity fraction, and a and n are empirical constants reflecting pore morphology and connectivity. For highly irregular and partially connected porosity (e.g., regolith-based composites), literature fits for porous ceramics justify using parameters toward the upper end of typical ranges. In this work we adopt $a = 3.85$ and $n = 4.62$ as representative values [207–210]. Introducing the morphology factor $a > 1$ generalizes the simple $(1 - \phi)^n$ form and improves agreement with data for non-spherical/connected pores

[207, 209].

Young’s Modulus of each oxide in Lunar Regolith Simulant

Based on the literature, the Young’s modulus values for the oxide phases are summarized in Table 4.4 [8, 10–15].

Table 4.4: Young’s modulus values for the oxide phases [8, 10–15]. The values cited here are compiled from primary measurements and standard handbooks. Dense, stable bulk data for Na_2O and K_2O at room temperature are scarce due to their reactivity and hygroscopicity; several studies report single-crystal elastic constants (from which E can be derived), but reliable bulk experimental E values are limited. For FeO (wüstite) and MnO (manganosite), the modulus depends strongly on stoichiometry and defect content, and reported values are frequently inferred from single-crystal elastic constants. For P_2O_5, reported moduli span crystalline polymorphs and phosphate glasses. Where literature variability exists, we provide a representative value.

Oxide	E_i **(GPa)**
SiO_2 (Silica)	73
TiO_2 (Rutile)	230
Al_2O_3 (Alumina)	380
FeO (Wüstite)	150
MnO (Manganosite)	160
MgO (Periclase)	280
CaO (Lime)	110
Na_2O (Sodium Oxide)	30
K_2O (Potassium Oxide)	20
P_2O_5 (Phosphorus Pentoxide)	10

4.4.1 Volume Fraction Calculation

The volume fraction V_i is given by:

$$V_i = \frac{W_i/\rho_i}{\sum(W_i/\rho_i)} \tag{9}$$

as per Tables 4.1 and 4.2. Computing the denominator:

$$\sum(W_i/\rho_i) = 31.191 \text{ cm}^3/\text{g} \tag{10}$$

Resulting computed V_i for each oxide is summarized in Table 4.5.

Table 4.5: Volume fractions of different oxides in the material composition.

Oxide	**Volume Fraction V_i**
SiO_2 (Silica)	0.567
TiO_2 (Rutile)	0.027
Al_2O_3 (Alumina)	0.100
FeO (Wüstite)	0.048
MnO (Manganosite)	0.0012
MgO (Periclase)	0.150
CaO (Lime)	0.067
Na_2O (Sodium Oxide)	0.024
K_2O (Potassium Oxide)	0.0093
P_2O_5 (Phosphorus Pentoxide)	0.0027

4.4.2 Resulting Young's Modulus Estimates

This section reports the composite stiffness predicted from the micromechanics framework. First, we establish the defect-free bounds using Voigt (iso-strain) and Reuss (iso-stress) estimates and their mean, which together bracket the elastic response of a fully dense material with the measured phase fractions. We then account for processing-induced porosity using an empirical stiffness–porosity relation to obtain the effective Young's modulus at realistic pore levels.

Fully Dense Material

For a porosity-free composite, the classical bounds provide a stiffness interval that reflects the best- and worst-case phase load sharing. The Voigt bound corresponds to perfectly constrained (parallel) phases, while the Reuss bound corresponds to perfectly compliant (series) phases. So, their average serves as a practical central estimate for isotropic polycrystals.

- **Upper Bound (Voigt):** $E_{\text{upper}} = 143.94\ \text{GPa}$
- **Lower Bound (Reuss):** $E_{\text{lower}} = 89.40\ \text{GPa}$
- **Average (VRH midpoint):** $E_{\text{avg}} = 116.67\ \text{GPa}$

Effective Modulus f the Regolith Phase with Porosity

To reflect the characteristics of the regolith phase, we reduce the dense modulus by the measured porosity using Equation 8. Here, E_0 is the dense (porosity-free) estimate, ϕ is the porosity fraction obtained from image analysis, and (a, n) capture the sensitivity to pore morphology/connectivity. This converts the idealized stiffness to an effective modulus suitable for comparison with experiments.

With $E_0 = 116.67$ GPa, $a = 3.85$, and $n = 4.62$, we obtain for a representative porosity of $\phi = 0.121$ (12.1%):

$$\begin{aligned} E(\phi{=}0.121) &= 116.67 \times \big(1 - 3.85 \times 0.121\big)^{4.62} \\ &= 116.67 \times (0.534)^{4.62} \\ &\approx \boxed{6.45 \text{ GPa}}. \end{aligned} \tag{11}$$

The calculated value of $E_r = 6.45$ GPa provides a reasonable estimate of the Young's modulus for the regolith particle phase. Again, the true modulus E of a defect-free material lies between the Reuss and Voigt limits. However, in practice, microstructure, phase distribution, and porosity must be considered, since porosity reduces stiffness. This result highlights the severe stiffness knockdown imposed by $\sim$12% porosity relative to the dense upper-bound behavior, consistent with the strong porosity sensitivity of ceramic materials.

4.5 Homogenized Matrix Modulus Estimation for Fine Regolith Particles in PEEK

4.5.1 Objective

To reduce computational complexity in the finite element simulations, regolith particles smaller than 1 µm, comprising approximately 11% of the total regolith volume [5], are excluded from the explicit geometry in Abaqus. Instead, their mechanical contribution is incorporated by homogenizing them with the PEEK matrix. This section outlines the methodology used to compute the effective elastic modulus of this modified matrix using Voigt and Reuss bounds.

4.5.2 Material Properties

- Elastic modulus of PEEK (E_m): 1.14 GPa
- Elastic modulus of regolith (E_r): 6.45 GPa
- Fine regolith fraction: 11% of the total regolith volume

4.5.3 Methodology

The homogenization procedure follows these steps:

(1) Converting the target regolith weight fraction (W_{reg}) into a total volume fraction ($V_{\text{reg,orig}}$), using:

$$V_{\text{reg,orig}} = \frac{W_{\text{reg}}/\rho_{\text{reg}}}{(W_{\text{reg}}/\rho_{\text{reg}}) + ((1 - W_{\text{reg}})/\rho_{\text{PEEK}})} \tag{12}$$

where $\rho_{\text{reg}} = 2.77$ g/cm^3 and $\rho_{\text{PEEK}} = 1.30$ g/cm^3.

(2) Separating the regolith volume into coarse (explicitly modeled) and fine (homogenized) components [5]:

$$V_{\text{coarse}} = 0.89 \cdot V_{\text{reg,orig}}, \quad V_{\text{fine}} = 0.11 \cdot V_{\text{reg,orig}} \tag{13}$$

(3) Calculating the total matrix volume, which consists of the PEEK matrix and the fine regolith:

$$V_{\text{matrix}} = (1 - V_{\text{reg,orig}}) + V_{\text{fine}} \tag{14}$$

(4) Normalizing the fine regolith and PEEK fractions within the matrix:

$$V'_{\text{fine}} = \frac{V_{\text{fine}}}{V_{\text{matrix}}}, \quad V'_{\text{PEEK}} = 1 - V'_{\text{fine}} \tag{15}$$

(5) Calculating the homogenized matrix modulus using the Voigt and Reuss bounds:

$$E_V = V'_{\text{PEEK}} \cdot E_m + V'_{\text{fine}} \cdot E_r \tag{16}$$

$$E_R = \left(\frac{V'_{\text{PEEK}}}{E_m} + \frac{V'_{\text{fine}}}{E_r} \right)^{-1} \tag{17}$$

$$E_{\text{avg}} = \frac{E_V + E_R}{2} \tag{18}$$

4.5.4 Sample Calculation for 10 wt% Regolith

$$V_{\text{reg,orig}} = \frac{0.10/2.77}{(0.10/2.77) + (0.90/1.30)} = 0.0496 \quad (4.96\%) \tag{19}$$

$$V_{\text{fine}} = 0.11 \cdot 0.0496 = 0.00546 \quad (0.55\%) \tag{20}$$

$$V_{\text{matrix}} = 0.9504 + 0.00546 = 0.95586 \quad (95.59\%) \tag{21}$$

$$V'_{\text{fine}} = \frac{0.00546}{0.95586} = 0.00570, \quad V'_{\text{PEEK}} = 1 - 0.00570 = 0.99430 \tag{22}$$

$$E_V = 0.99430 \cdot 1.14 + 0.00570 \cdot 6.45 = 1.1703 \text{ GPa} \tag{23}$$

$$E_R = \left(\frac{0.99430}{1.14} + \frac{0.00570}{6.45}\right)^{-1} = 1.1454 \text{ GPa} \tag{24}$$

$$E_{\text{avg}} = \frac{1.1703 + 1.1454}{2} = 1.1578 \text{ GPa} \tag{25}$$

4.5.5 Results for 10–50 wt% Regolith

Table 4.6 reports the homogenized PEEK matrix modulus when blended with fine (smaller than 1 µm) regolith particles, assuming the fines constitute 11% of the regolith volume.

Table 4.6: Homogenized matrix modulus considering fine regolith particles (11% of the regolith volume) blended with the PEEK matrix.

Reg. wt%	**Volume Fractions (%)**				**Normalized Matrix Fractions**		**Homogenized Modulus (GPa)**		
	Total Reg.	Coarse	Fine	Matrix	PEEK	Fine Reg.	Voigt	Reuss	Average
10	4.96	4.41	0.55	95.59	0.9943	0.0057	1.1703	1.1454	1.1578
20	10.50	9.35	1.16	90.49	0.9873	0.0127	1.2077	1.1521	1.1799
30	16.75	14.90	1.84	85.10	0.9784	0.0216	1.2549	1.1607	1.2078
40	23.83	21.21	2.62	78.79	0.9667	0.0333	1.3167	1.1721	1.2444
50	31.94	28.43	3.51	71.57	0.9509	0.0491	1.4007	1.1880	1.2943

Incorporating submicron regolith particles into the PEEK matrix via homogenization results in an effective matrix modulus ranging from approximately 1.16 to 1.29 GPa across the studied range of 10–50 wt% regolith. These moduli are used in Abaqus simulations to represent the matrix phase, while only the coarse regolith particles are explicitly modeled. This approach maintains mechanical accuracy while substantially reducing meshing complexity and computational cost.

4.6 Simulation Results

This section summarizes the finite element simulation results conducted in Abaqus. Each simulation is performed using a CAD model that includes only coarse regolith particles (above 1 μm), while the matrix is assigned an effective modulus computed from the homogenization of PEEK and fine regolith particles (below 1 μm), as detailed in Section 4.5.

4.6.1 Mesh Sensitivity Analysis

This section presents the mesh sensitivity analysis conducted to ensure that the finite element results are independent of mesh resolution. The analysis is conducted on the most demanding case, which corresponds to an RVE with the highest regolith loading (50 wt%, approximately 31.94 vol%) and the largest domain size (0.3 mm × 0.3 mm). This configuration results in the highest particle count and the most extensive matrix–particle interfacial area.

Three mesh resolutions are tested by progressively halving the global seed size: 2 μm, 1 μm, and 0.5 μm. All simulations are run in Abaqus using CAD models containing only coarse regolith particles (above 1 μm). The matrix phase is assigned an effective modulus accounting for the fine particles, as detailed in Section 4.5.

The table below summarizes the results of the sensitivity analysis. Effective Young's modulus of the composite ($E_{\text{composite}}$) is recorded at each level. Mesh convergence is considered achieved when the change in modulus between successive refinements is below 1%. Based on this criterion, the 1 μm mesh is deemed sufficient and adopted for the rest of the study.

4.6.2 RVE Size Sensitivity Analysis

This section presents the RVE size sensitivity analysis, which is performed to ensure that the finite element predictions are independent of the RVE domain size. The analysis is conducted using the most demanding configuration, which corresponds to an RVE with the highest regolith content (50 wt%, approximately 31.94 vol%). This setup results in the largest particle count and the most

Table 4.7: Mesh sensitivity analysis for the worst-case RVE. Simulation parameters and resulting composite modulus are shown.

CAD File	**RVE Dimensions (mm)**	**Particle Density (%)**	**Mesh Size (µm)**	**Element Count**	**Elongation (%)**	E_{regolith} **(GPa)**	E_{matrix} **(GPa)**	$E_{\text{composite}}$ **(GPa)**
15	0.3×0.3	31.94	2	242212	10	6.45	1.29	1.99
15	0.3×0.3	31.94	1	394612	10	6.45	1.29	1.96
15	0.3×0.3	31.94	0.5	990720	10	6.45	1.29	1.95

complex matrix–particle interface.

Two RVE sizes are evaluated by doubling the domain dimensions, thereby increasing the area by a factor of four: 0.15 mm (see Figure 4.1) and 0.3 mm (see Figure 4.4). All simulations are carried out in Abaqus using CAD models that include only coarse regolith particles (larger than 1 µm). The matrix phase is assigned an effective modulus to account for the fine particles, as described in Section 4.5.

Figure 4.2 shows the longitudinal strain field E_{11} for the 0.15×0.15 mm RVE (CAD file No. 31), and Figure 4.5 presents the corresponding field for the 0.30×0.30 mm RVE (CAD file No. 15). In both cases the matrix carries most of the deformation, with the highest E_{11} concentrated in narrow polymer ligaments and near sharp particle corners, while inclusions remain comparatively strain-shielded. The strain-partitioning pattern is similar between the two RVEs. Enlarging the edge length from 0.15 to 0.30 mm smooths some fine-scale fluctuations yet preserves the topology and areal fraction of high-strain paths. No new banding or emergent length-scale effects appear.

Figure 4.3 displays the axial stress field S_{11} for the 0.15×0.15 mm RVE and Figure 4.6 for the 0.30×0.30 mm RVE under identical macroscopic loading. The stress maps are governed by matrix-borne streaks aligned with the loading direction and by local hot spots at inclusion contacts and re-entrant corners. With the larger RVE these hot spots appear slightly more diffuse due to averaging over a broader particle population, but their intensity levels and spatial frequency remain comparable. The similarity of the stress-bearing skeleton and the limited change in upper-tail stresses indicate convergence of the micro-stress response with respect to RVE size.

Overall, doubling the in-plane RVE dimension from 0.15 to 0.30 mm does not significantly alter strain- and stress-partitioning mechanisms or the homogenized response. Within this size window the microfields are stationary.

In terms of the global elastic modulus, Table 4.8 shows that the homogenized response is essentially size-insensitive over the tested window: $E_{\text{composite}} = 1.98$ and 1.97 GPa for the 0.15×0.15 and 0.30×0.30 mm RVEs, respectively. The relative change is $\approx 0.5\%$, meeting our convergence criterion of $< 1\%$ between successive sizes. Nevertheless, we adopt the larger 0.30 mm RVE for all subsequent analyses as a conservative choice. The larger domain reduces potential finite-size bias, better averages microstructural clustering, and yields smoother tail statistics in the strain/stress fields. In short, the global modulus has converged, but the 0.30 mm RVE offers greater statistical representativeness at acceptable computational cost and is therefore selected going forward.

Table 4.8: RVE size sensitivity analysis for the highest regolith content (50 wt%). Simulation parameters and the resulting composite Young's modulus are presented.

CAD File	**RVE Dimensions (mm)**	**Particle Density (%)**	**Mesh Size (µm)**	**Element Count**	**Elongation (%)**	E_{regolith} **(GPa)**	E_{matrix} **(GPa)**	$E_{\text{composite}}$ **(GPa)**
31	0.15×0.15	31.94	1	56,753	10	6.45	1.29	1.98
15	0.30×0.30	31.94	1	394,612	10	6.45	1.29	1.97

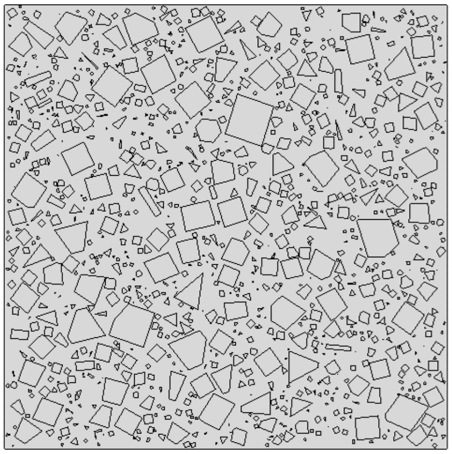

Figure 4.1: CAD file No. 31, with an RVE of 0.15 mm × 0.15 mm and a particle loading of 50 wt%.

4.6.3 Effect of Particle Density

This section examines the influence of particle density on the composite's mechanical behavior. The analysis is carried out using an RVE of dimensions 0.3×0.3 mm with a mesh size of 1 µm. In

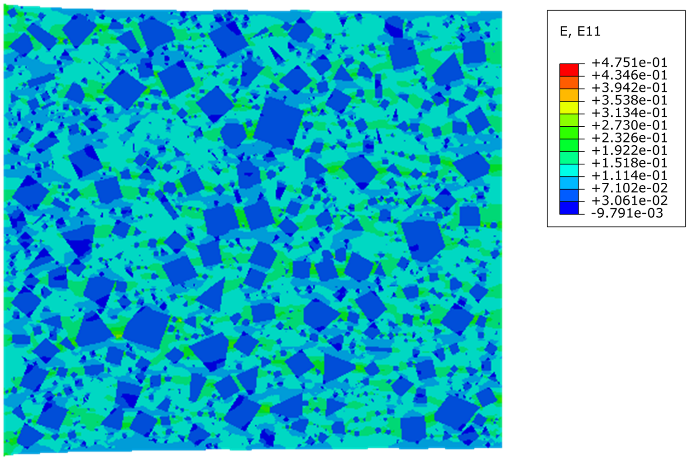

Figure 4.2: Contour plot of the strain component E_{11} obtained from the Abaqus simulation. The results correspond to CAD file No. 31 with an RVE size of 0.15 mm × 0.15 mm and a mesh size of 1 µm. The matrix and regolith phases have Young's moduli of 1.29 GPa and 6.45 GPa, respectively, with a prescribed elongation of 10 %.

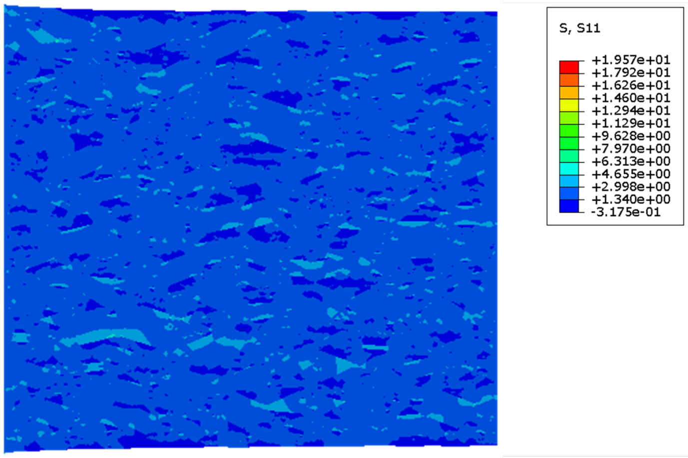

Figure 4.3: Contour plot of the stress component S_{11} obtained from the Abaqus simulation. The results correspond to CAD file No. 31 with an RVE size of 0.15 mm × 0.15 mm and a mesh size of 1 µm. The matrix and regolith phases have Young's moduli of 1.29 GPa and 6.45 GPa, respectively, with a prescribed elongation of 10 %.

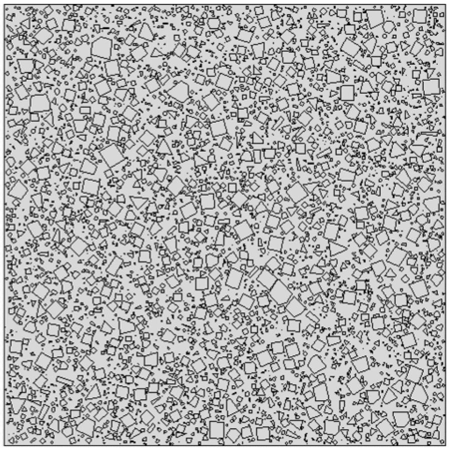

Figure 4.4: CAD file No. 15, with an RVE of 0.3 mm × 0.3 mm and a particle loading of 50 wt%.

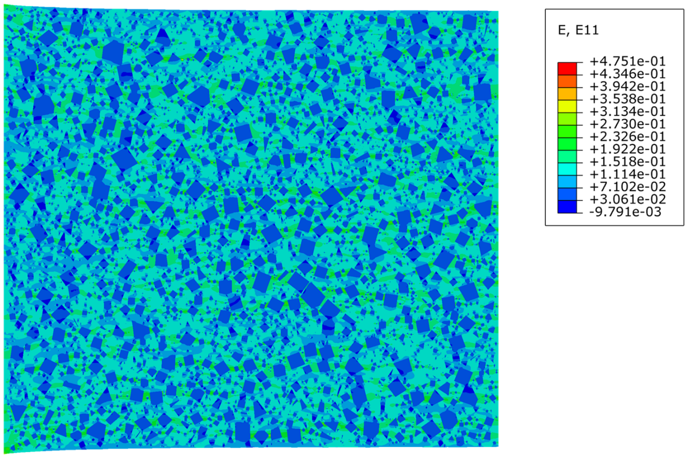

Figure 4.5: Contour plot of the strain component E_{11} obtained from the Abaqus simulation. The results correspond to CAD file No. 15 with an RVE size of 0.3 mm × 0.3 mm and a mesh size of 1 µm. The matrix and regolith phases have Young's moduli of 1.29 GPa and 6.45 GPa, respectively, with a prescribed elongation of 10 %.

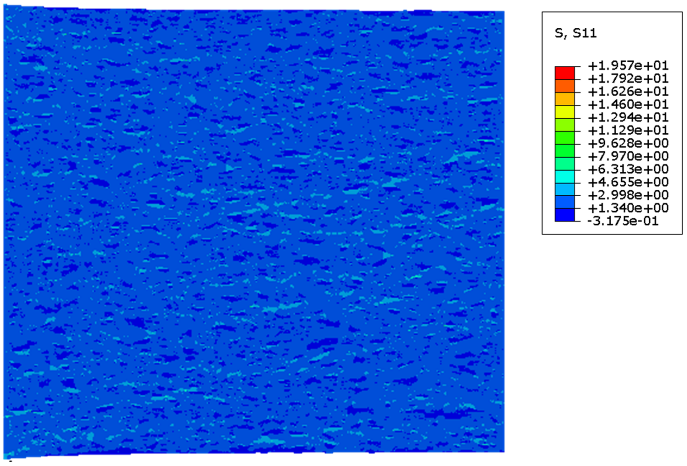

Figure 4.6: Contour plot of the strain component S_{11} obtained from the Abaqus simulation. The results correspond to CAD file No. 15 with an RVE size of 0.3 mm × 0.3 mm and a mesh size of 1 µm. The matrix and regolith phases have Young's moduli of 1.29 GPa and 6.45 GPa, respectively, with a prescribed elongation of 10 %.

alignment with the experimental setup, five regolith loadings are considered: 10 wt% (4.96 vol%), 20 wt% (10.50 vol%), 30 wt% (16.75 vol%), 40 wt% (23.83 vol%), and 50 wt% (31.94 vol%). Representative CAD geometries for these cases (CAD files 1, 6, 7, 10, and 15) are shown in Fig. 4.7.

Representative strain (E_{11}) and stress (S_{11}) maps for 10, 20, 30, 40, and 50 wt% regolith are shown in Figs. 4.8b–4.9b, 4.8c–4.9c, 4.8d–4.9d, 4.8e–4.9e, and 4.8f–4.9f, respectively. Together they reveal a consistent, matrix-dominated load-transfer mechanism with progressively tighter polymer ligaments as the inclusion content increases.

10 wt% (CAD 1). In Figs. 4.8b and 4.9b, inclusions are well separated within a continuous polymer matrix. The E_{11} field is smooth at the mesoscale, with small, localized low-strain halos around particles and mild strain amplification in intervening ligaments. The S_{11} map shows sparse, short stress streaks aligned with loading and limited hot spots at re-entrant corners.

20 wt% (CAD 6). Figs. 4.8c and 4.9c show reduced inclusion spacing due to higher particle loading. Strain-shielded zones expand and begin to overlap, producing more tortuous high-strain paths through the matrix. The S_{11} field exhibits more numerous hot spots and longer streaks, especially where two particles approach within a ligament thickness.

30 wt% (CAD 7). In Figs. 4.8d and 4.9d, quasi-continuous clusters appear. Polymer ligaments are thinner and more anisotropic, so E_{11} localization becomes more segmented. Stress hot spots

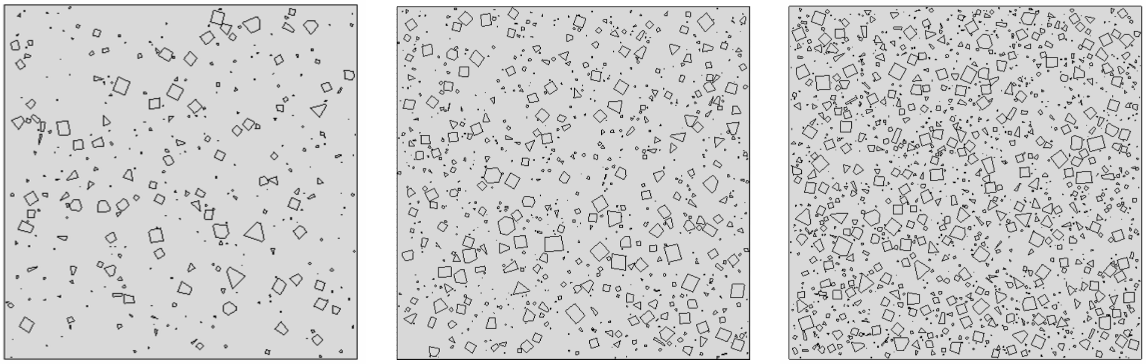

(a) CAD 1 (10% wt)

(b) CAD 6 (20% wt)

(c) CAD 7 (30% wt)

(d) CAD 10 (40% wt)

(e) CAD 15 (50% wt)

Figure 4.7: Representative CAD geometries generated for finite-element analyses, corresponding to regolith loadings of (a) 10 wt%, (b) 20 wt%, (c) 30 wt%, (d) 40 wt%, and (e) 50 wt%.

concentrate at multi-particle junctions and along narrow ligaments. The stress-bearing skeleton is denser, and the spacing between hot regions is reduced relative to 20 wt%.

40 wt% (CAD 10). Figs. 4.8e and 4.9e show common particle clusters and a thinned polymer network. Connectivity is reduced, but the matrix remains continuous. The E_{11} maps display extensive low-strain zones with high-strain channels threading the remaining ligaments. In S_{11}, elongated streaks and near-contact hot spots dominate, with higher intensity and frequency than at 30 wt%.

50 wt% (CAD 15). As seen in Figs. 4.8f and 4.9f, ligaments are very narrow and strain is strongly partitioned. Inclusions remain low-strain while the matrix accommodates most deformation along a fine network of high-E_{11} channels. The S_{11} field is saturated with short-wavelength streaks and hot spots reflecting frequent near-contacts and sharp corners. Despite this micro-level intensification, the macroscale stiffness gain is moderate because the regolith–matrix modulus contrast is only of order unity. The composite remains matrix-controlled even at the highest loading.

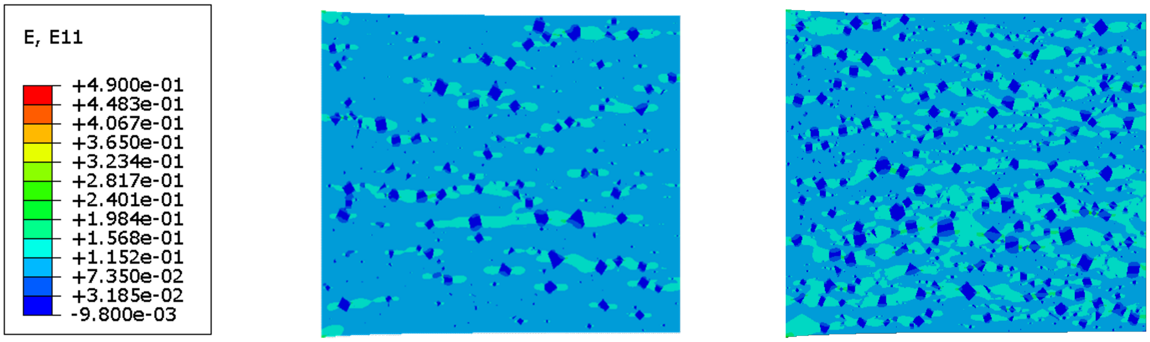

(a) Scale. (b) CAD 1 (10 wt%). (c) CAD 6 (20 wt%).

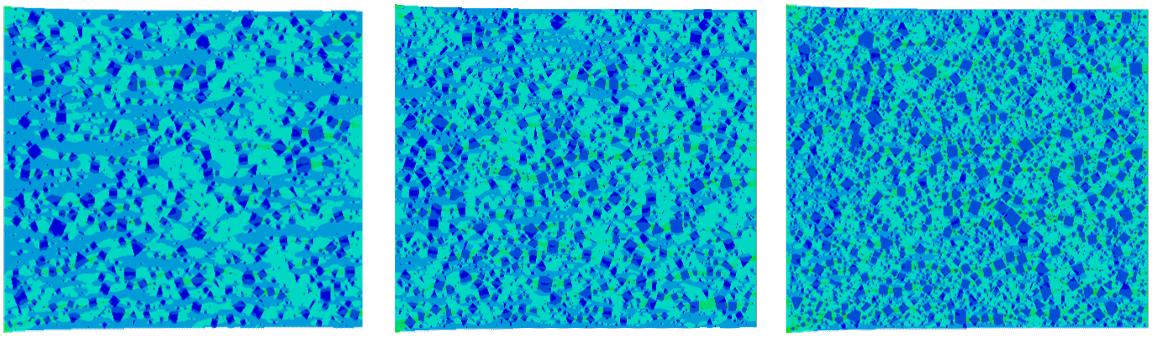

(d) CAD 7 (30 wt%). (e) CAD 10 (40 wt%). (f) CAD 15 (50 wt%).

Figure 4.8: Representative E_{11} strain microfields for regolith loadings of 10, 20, 30, 40, and 50 wt%, shown together with the corresponding color scale. Increasing particle content produces progressively narrower polymer ligaments and stronger strain partitioning.

Trend synthesis. Across 10 → 50 wt% (Figs. 4.8 and 4.9), (i) the matrix carries the majority of strain while inclusions are strain-shielded; (ii) the density and intensity of S_{11} hot spots increase with content due to thinner ligaments and more frequent near-contacts; and (iii) the stress-bearing skeleton becomes finer and more continuous, with no obvious shear-band organization. This explains the change in homogenized stiffness alongside progressively heavier local stress tails.

Table 4.9 includes three independent RVEs per composition to demonstrate reproducibility. Under the idealized assumptions (linear-elastic phases, perfect particle–matrix bonding, and no process defects), the simulations exhibit a smooth, monotonic increase in the homogenized modulus with rising regolith content. Table 4.10 then compares these predictions against measurements from additively manufactured coupons produced in Phase II (Chapter 3).

The small scatter (≤ 0.02 GPa) indicates that the 0.30×0.30 mm RVE captures the statistics of the microstructure with good repeatability.

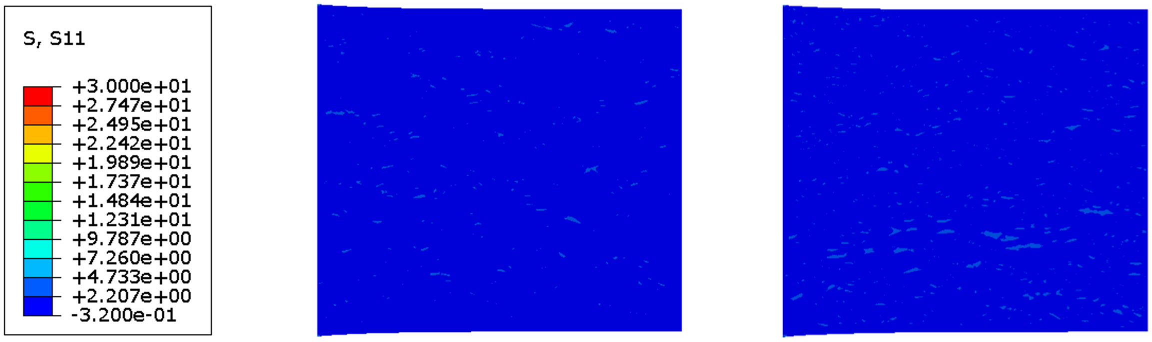

(a) Scale. (b) CAD 1 (10 wt%). (c) CAD 6 (20 wt%).

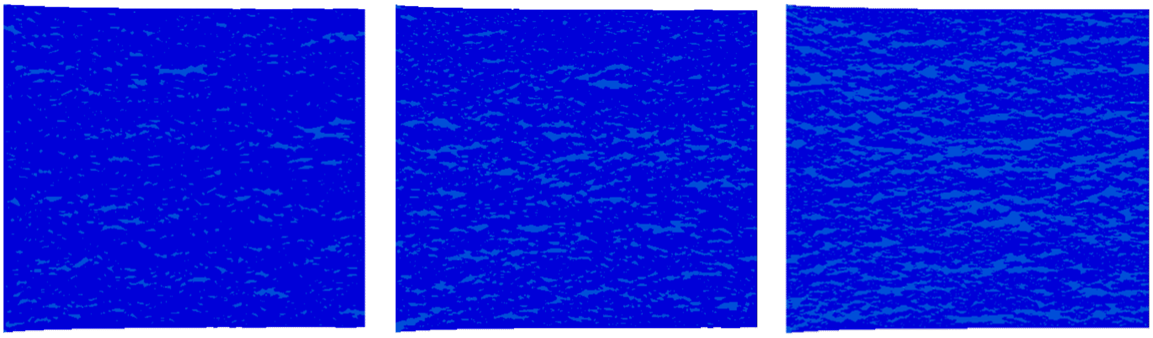

(d) CAD 7 (30 wt%). (e) CAD 10 (40 wt%). (f) CAD 15 (50 wt%).

Figure 4.9: Representative S_{11} stress microfields for regolith loadings of 10, 20, 30, 40, and 50 wt%, shown together with the color scale. Stress hot spots intensify and become more frequent with higher filler contents due to thinner ligaments and increased particle proximity.

The AM measurements show acceptable agreement with the simulations up to 40 wt%. As the particle volume fraction increases from 5 to 24 vol% (10–40 wt%), the maps indicate that (i) inclusions remain largely strain-shielded, (ii) the matrix develops a progressively finer network of high-E_{11} channels, and (iii) S_{11} hot spots become more numerous but remain discontinuous. The E_{11}/S_{11} maps (Figs. 4.8b–4.9f and geometries in Fig. 4.7) explain this trend. This morphology preserves a continuous, load-bearing polymer skeleton, so the global modulus increases modestly and the idealized FE agrees reasonably with experiment. Over this range the stiffening is gradual, a trend which is captured both in simulation and experiment. Percent differences between simulation and experiment of approximately 3.5%, 5.9%, 9.3%, and 10% at 10–40 wt%, respectively; these small but growing residual gaps are consistent with the observed increase in defect content and the progressive loss of matrix continuity as regolith loading rises, as corroborated by density measurements and microstructural analyses in Chapter 3, and with the simplifying assumptions in

Table 4.9: Finite-element predictions of composite Young's modulus for RVEs with different regolith particle densities. Three statistically independent RVEs are included per composition to demonstrate reproducibility.

CAD File	**RVE Dimensions (mm)**	**Particle Density (vol%)**	**Mesh Size (μm)**	**Element Count**	**Elongation (%)**	E_{regolith} **(GPa)**	E_{matrix} **(GPa)**	$E_{\text{composite}}$ **(GPa)**
1	0.3×0.3	4.96	1	335,268	10	6.45	1.16	1.27
2	0.3×0.3	4.96	1	315,282	10	6.45	1.16	1.27
3	0.3×0.3	4.96	1	328,974	10	6.45	1.16	1.28
4	0.3×0.3	10.50	1	360,310	10	6.45	1.18	1.38
5	0.3×0.3	10.50	1	336,102	10	6.45	1.18	1.39
6	0.3×0.3	10.50	1	359,858	10	6.45	1.18	1.39
7	0.3×0.3	16.75	1	346,902	10	6.45	1.21	1.54
8	0.3×0.3	16.75	1	355,626	10	6.45	1.21	1.53
9	0.3×0.3	16.75	1	348,202	10	6.45	1.21	1.52
10	0.3×0.3	23.83	1	360,466	10	6.45	1.24	1.71
11	0.3×0.3	23.83	1	358,802	10	6.45	1.24	1.70
12	0.3×0.3	23.83	1	351,312	10	6.45	1.24	1.71
13	0.3×0.3	31.94	1	396,622	10	6.45	1.29	1.96
15	0.3×0.3	31.94	1	394,612	10	6.45	1.29	1.97
16	0.3×0.3	31.94	1	387,558	10	6.45	1.29	1.99

the simulations.

The results deviate strongly at 50 wt% (experiment 1.27 GPa vs. FE 1.97 GPa, a $\sim 55\%$ gap). The simulated value shows continued gradual increase, while in the experimental dataset there is a drop in E between 40 and 50 wt% (Fig. 3.9). To attempt to capture this reversal in trend, defect-aware and single-printed-layer modeling is adopted, presented in the next subsections.

Defect-aware tiling strategy. A 0.9×0.9 mm region of the SEM image is shown in Fig. 4.10, also indicating a partitioning into a 3×3 grid of 0.3×0.3 mm tiles. As can be seen, different 0.3×0.3 mm patches in the same micrograph exhibit very different defect populations, so directly reproducing the exact defect field from SEM in a single 0.3×0.3 mm RVE is not reliable.

Two paths are considered: (i) a much larger single RVE that statistically averages the heterogeneity, which is computationally prohibitive at these particle counts; or (ii) a defect-aware tiling strategy that preserves spatial variability, described here.

A corresponding RVE is assigned to each tile in which the observed local defects are embedded. Each tile is analyzed in the small-strain elastic regime to obtain its axial modulus E_{ij}. The effective

Table 4.10: Mean FE-predicted modulus with sample standard deviation (three RVEs per composition), experimental modulus from AM coupons, and percent difference computed as $(\overline{E}_{\text{FE}} - E_{\text{Experiment}})/E_{\text{Experiment}} \times 100$.

wt%	**vol%**	$\overline{E}_{\textbf{FE}}$ **(GPa)**	$E_{\textbf{Experiment}}$ **(GPa)**	**Diff. (%)**
10	4.96	1.27 ± 0.01	1.23	3.50
20	10.50	1.39 ± 0.01	1.31	5.88
30	16.75	1.53 ± 0.01	1.40	9.29
40	23.83	1.71 ± 0.01	1.55	10.13
50	31.94	1.97 ± 0.02	1.27	55.35

stiffness of the entire 0.9×0.9 mm region is estimated using the classical Voigt and Reuss bounds [205, 206] and their arithmetic mean (Hill average).

$$E_{\text{Voigt}} = \frac{1}{9}\sum_{i=1}^{3}\sum_{j=1}^{3} E_{ij}, \tag{26}$$

$$E_{\text{Reuss}} = \left(\frac{1}{9}\sum_{i=1}^{3}\sum_{j=1}^{3} \frac{1}{E_{ij}}\right)^{-1}, \tag{27}$$

$$E_{\text{Hill}} = \tfrac{1}{2}\left(E_{\text{Voigt}} + E_{\text{Reuss}}\right). \tag{28}$$

Application to a representative 3×3 set. The procedure is applied to the region shown in Fig. 4.10. The tile moduli (GPa) are taken as

$$\left[1.90,\ 1.97,\ 1.97;\ 1.95,\ 1.60,\ 1.96;\ 1.97,\ 1.93,\ 1.95\right],$$

from which the following region-level estimates are obtained:

$$E_{\text{Voigt}} = 1.911 \text{ GPa}, \quad E_{\text{Reuss}} = 1.903 \text{ GPa}, \quad E_{\text{Hill}} = 1.907 \text{ GPa}.$$

These values remain significantly above the experimental modulus of 1.27 GPa at 50 wt%. It is therefore concluded that, although realistic heterogeneity and weak tiles are introduced by the tiling approach, the full reduction measured in the printed coupons is not captured by this method alone.

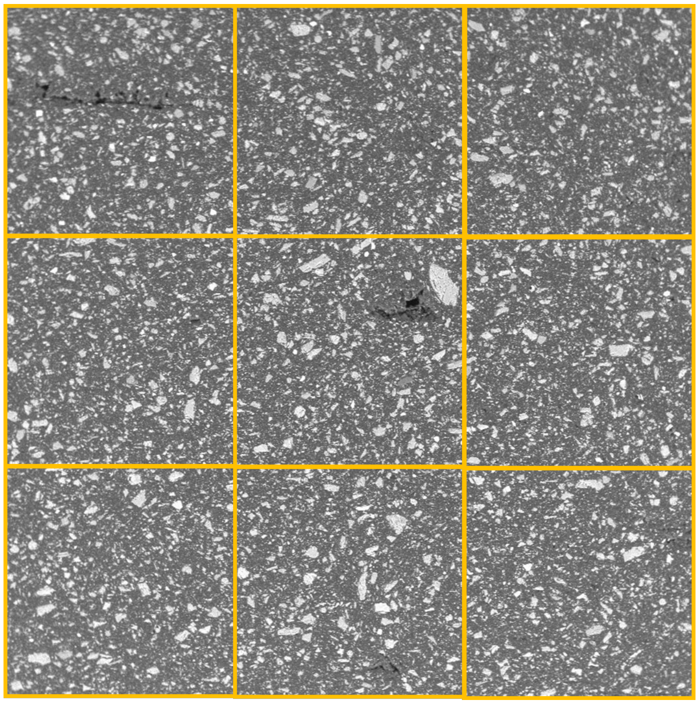

Figure 4.10: A 0.9×0.9 mm region from the SEM micrograph of the PEEK/LRS50 specimen, subdivided into a 3×3 array of 0.3×0.3 mm tiles. Each tile is used to construct a defect-aware RVE that captures local defect variability.

To further interrogate the discrepancy, a complementary approach is adopted: the worst tile is selected (i.e., the tile containing the defect with the largest perpendicular extent relative to the loading direction). Figure 4.11a shows a larger SEM field of the PEEK/LRS50 sample with the printed-layer boundaries and the selected tile (black box) used for the single-layer RVE. A single-printed-layer RVE with in-plane dimensions 0.3 mm (along x, parallel to the load) and 0.24 mm (along y, equal to one printed-layer thickness) is constructed. Figure 4.11 shows the zoomed-in SEM defect and the corresponding idealized geometry used in the model, and Fig. 4.12 presents the resulting E_{11} and S_{11} fields. For this tile, the homogenized modulus decreases from ~ 1.96 GPa (defect-free) to ~ 1.45 GPa, confirming the pronounced stiffness penalty when the defect height-to-tile height ratio, $h_{\text{defect}}/h_{\text{tile}}$, is large.

Single-printed-layer response. With a large, crack-like void inside one printed layer (Figs. 4.11 and 4.12), strain localizes within the thin polymer ligament around the void. Load is then transmitted through a few narrow ligaments, and the layer effectively behaves like two stiff pieces joined

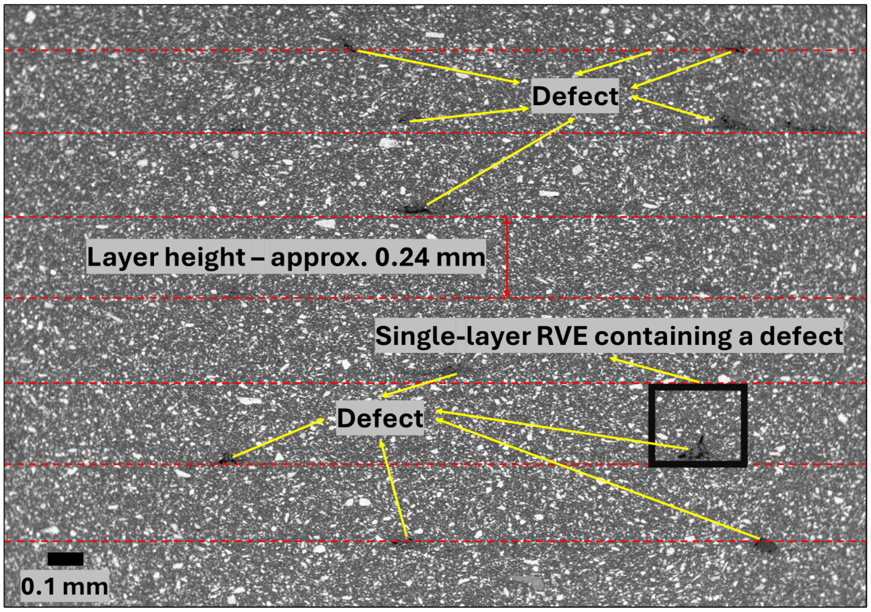

(a) Larger SEM field of the 50 wt% sample. Dashed red lines indicate printed layers (layer height ≈ 0.24 mm); the black box marks the single-layer RVE location.

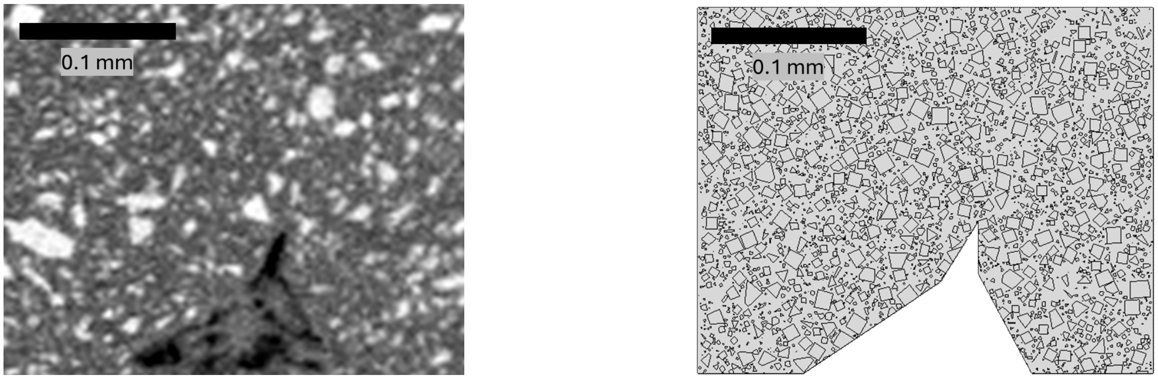

(b) Zoomed tile with a representative defect.

(c) Single-layer geometry adopted from the SEM.

Figure 4.11: Defect-aware single-layer RVE construction. (a) Larger SEM field of the PEEK/LRS50 sample with printed-layer boundaries marked by dashed red lines; the black box denotes the selected tile. (b) Zoomed-in view of the representative defect. (c) Idealized single-layer geometry extracted from the SEM image for finite-element modeling.

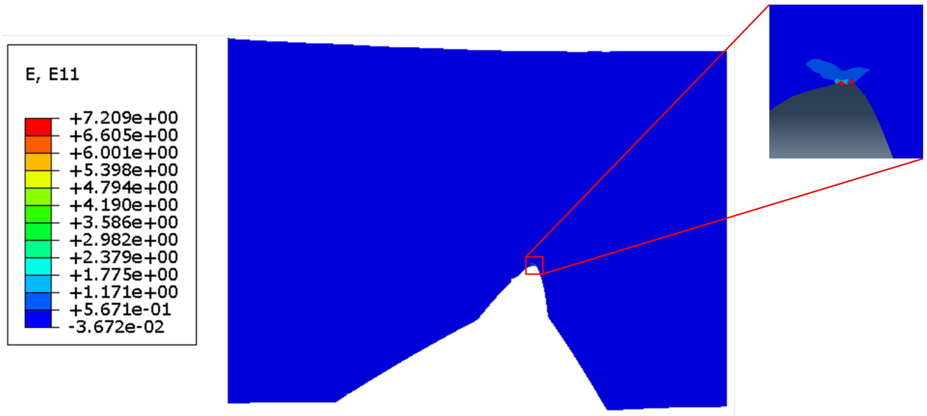

(a) E_{11} field for the defected layer.

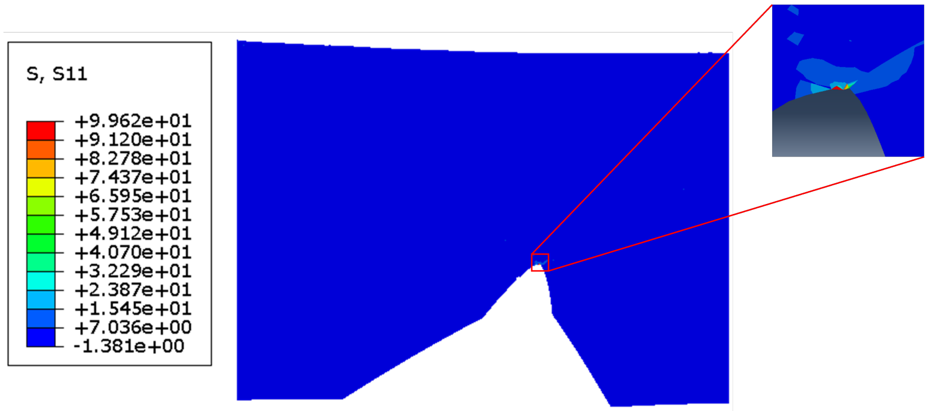

(b) S_{11} field for the defected layer.

Figure 4.12: Computed microfields for the defected single-layer RVE. (a) Axial strain field E_{11} showing strong localization within the narrow ligament surrounding the defect. (b) Axial stress field S_{11} illustrating pronounced stress concentrations and reduced effective stiffness at the layer scale.

by a soft seam. The narrow ligament exhibits strong stress concentration and a locally reduced effective modulus, which lowers the overall (RVE-level) stiffness. In the representative case of Figs. 4.12a–4.12b, the RVE modulus falls from about 1.96 GPa (no defect) to about 1.45 GPa, showing how a single tall void, representing a significant proportion of the layer thickness ($\approx 41\%$ in this example), can strongly reduce stiffness.

Part-level implications. In the printed part, many such interfacial voids are distributed across successive layers. Although the total porosity at 50 wt% is modest, the defect morphology is likely highly deleterious. Elongated voids and partially starved welds occurring along bead–bead and layer–layer boundaries (as shown in Fig. 4.11a), together with local crystallinity variations and early particle–matrix micro-debonding, may create a network of compliant interphases. As these weak regions become connected across multiple layers, the effective load path must repeatedly traverse them, plausibly leading to a network-controlled stiffness that is substantially lower than that predicted by defect-free RVEs or tile-wise averaging. This network effect offers a plausible explanation for why the defect-aware tiling approach still overpredicts E for the whole coupon, whereas the single-printed-layer analysis captures how tall, crack-like interfacial defects can drive the modulus toward the experimental value at 50 wt%.

A broader mechanistic interpretation of this drop is provided in the following section.

4.7 Mechanistic origin of the modulus drop at 50 wt% under in-plane loading

4.7.1 Observation and problem statement

For the 50 wt% (volume fraction $\phi \approx 0.32$) PEEK/regolith composite loaded parallel to the printed layers, a defect-agnostic finite-element (FE) model predicts $E_{\text{FE}} = 1.97 \pm 0.02$ GPa, whereas tensile tests yield $E_{\text{Experiment}} = 1.27$ GPa. Micrographs and porosimetry indicate a modest total porosity ($\phi \approx 0.075$[1]), but the defects seem to be strongly interfacial and crack-like (elongated

---

[1] Here, porosity refers to the bulk porosity of the composite, measured experimentally in Chapter 3. The 12.1% value refers specifically to the porosity of the regolith phase within the composite. It was estimated by (i) measuring part porosity for the 40 wt% sample via image analysis (1.45%), (ii) combining that measurement with the Archimedean

voids aligned with bead–bead and layer–layer boundaries and polymer-starved welds). Adding a few large defects to the RVEs through ”tiling method” explained earlier lowers the prediction only to about 1.90 GPa. However, for a worst-case tile containing a single 0.24 mm printed layer with a major defect it is reduced to about 1.45 GPa.

The measured 1.27 GPa therefore requires additional interfacial compliance beyond isolated pores or a single extreme defect.

4.7.2 How interfaces could dominate even when load is parallel to layers

The main mechanisms that could explain the significant drop in Young’s modulus are summarized below. The aim is to indicate where the basic FE assumptions become limiting at 50 wt%.

(a) Parallel loading does not ensure uniform strain.

If interlayer welds were fully consolidated and defect-free, strain sharing would be expected to remain nearly uniform. At 50 wt%, however, the welds are likely polymer-starved and may exhibit partial debonding, so adjacent roads may transfer load inefficiently. Numerous defects appear at interfaces between successive layers, suggesting weakened interlayer bonding, reduced adhesion, and non-uniform strain transfer. Collectively, these features imply that interlayer regions may act as early-compliant seams that disrupt load continuity even at small strains.

(b) Porosity fraction is modest; porosity shape is harmful. Although the overall porosity is modest ($\phi \approx 7.5\%$), the elongated interfacial voids likely behave more like short, crack-like defects than conventional rounded pores. Their geometry can amplify local strain at weld roots, interrupt stress transfer between adjacent roads, and may even trigger interfacial slip or opening at very small global strains. When such voids are aligned along bead or layer boundaries, the resulting crack-like porosity can impose a disproportionately large stiffness penalty, consistent with the localized strain and stress patterns observed in Fig. 4.12.

---

composite density to infer the fully dense composite density, (iii) using PEEK’s density (1.30 g/cm^3) to back-calculate the in-composite regolith-phase density, and (iv) comparing that density to the fully dense regolith density computed from its oxide constituents and weight fractions. The resulting ratio yields a regolith-phase porosity of 12.1%.

(c) **Early particle–matrix micro-debonding lowers the initial tangent modulus.** At high filler loading, angular particles and residual stresses likely hinder wetting. Nanoscale gaps at particle–matrix interfaces may open at very small strains, creating a compliant annulus around particles while both phases remain nominally elastic. Since welds already concentrate strain, micro-debonding is expected to initiate and grow preferentially along these regions, which lowers the effective stiffness relative to models that assume perfect bonding.

(d) **Local losses of crystallinity and orientation at welds.** Higher melt viscosity at 50 wt% probably reduces the time available for chain interdiffusion and sintering at bead contacts. Faster heat extraction near interfaces may further depress crystallinity and orientation. Because PEEK stiffness depends on both, weld zones are likely softer than road interiors. The gauge then behaves like stiff road segments separated by softer seams, which adds series compliance through interfacial slip.

(e) **Connectivity of weak regions.** At $V_{\text{regolith}} \approx 0.32$, the compliant interphases, starved welds, imperfect particle shells, and strings of crack-like voids may approach a percolation threshold. Once a weak network forms, every load path is likely to cross it, so the macroscopic response becomes governed by the soft network rather than by the volume-average properties of the phases. The effective modulus becomes series-controlled (i.e., weak segments lie in series along the load path, so their compliances add and the softest/thinnest ligaments dominate). Even thin ligaments with locally low stiffness can dominate the overall response when they connect from one side of the gauge to the other. Practically, this may manifest as (i) a rise in the area fraction and contiguity of high-S_{11} zones at weld roots, (ii) reduced minimum ligament width along layer boundaries, and (iii) the emergence of a single connected weak cluster across the field of view. This connectivity provides a plausible explanation for the non-monotonic trend in stiffness: it rises with filler up to about 40 wt%, then drops at 50 wt% despite the higher solid fraction predicted by perfectly bonded micromechanics.

4.7.3 Synthesis

Up to 40 wt% regolith, the experimental modulus remains close to defect-free FE predictions. Including modest, isolated defects would likely improve agreement and is expected to have only a limited influence in this range. At 50 wt% a substantial gap appears: the FE response decreases only slightly, from about 1.97 GPa to about 1.90 GPa when defects are added in an averaged sense, whereas the experiment gives 1.27 GPa. The frequency of tall interfacial defects appears high, with several large defects present in each layer. Interlayer welds are likely weak, so load may not be transferred uniformly between layers. These effects lower the modulus of individual layers and hinder uniform load transfer through the thickness. Particle–matrix boundaries are likely polymer-starved at 50 wt%, and interfacial opening may initiate at relatively low strains.

Overall, the data and observations suggest a transition to an interface-controlled regime in which starved welds, early interfacial debonding, and local losses of crystallinity and orientation combine to form a connected, slip-compliant network along layer boundaries. The simplifying assumptions in the model, especially the neglect of the nonlinear and connected effects of defect morphology, imperfect bonding, and spatial heterogeneity, likely contribute to overprediction when the tensile axis is parallel to layers. A closer match between simulation and experiment is expected for compression-molded parts, where printing-induced interfacial weaknesses and crack-like interfacial defects are absent or strongly reduced. Beyond a threshold filler content, the in-plane elastic response of printed PEEK/regolith composites appears to be governed more by interfacial mechanics, defect morphology, and the percolation of weak seams than by porosity fraction and phase moduli alone.

Chapter 5

Phase IV: Feasibility Study on Laser Powder Bed Fusion of Lunar Regolith-based Materials

This chapter is based on, and in parts reproduces with minor editorial changes, the following in-preparation work:

Azami, M., Lam, R., Patel, S., Walls, X., Oluwajuyigbe, T., Darroch, A., Skonieczny, K., Vlasea, M.,& Feehan, M. (2025). Comparative Investigation of Laser Powder Bed Fusion of Lunar Regolith Simulant and Its Composite with Invar 36. *In preparation*, 2025.

5.1 Motivation

Trends in in-situ resource utilization (ISRU) reinforce the need for on-site manufacturing. Lunar regolith is the loose, unconsolidated layer of material that covers the Moon's solid bedrock. The composition of regolith varies by location, but it is generally rich in silicate minerals such as plagioclase feldspar, pyroxene, and olivine, along with oxides of iron and titanium [26, 211–213]. Using Lunar regolith as the base manufacturing and construction material reduces dependence on Earth and enables a more sustainable Lunar-based manufacturing and construction (LBMC) [24].

For LBMC, no single AM technique is inherently preferred. Instead, the choice depends on factors such as available resources, including energy, equipment, and off-site materials, as well as part requirements like dimensional accuracy and mechanical properties. Among these methods, powder bed fusion (PBF), particularly laser powder bed fusion (LPBF), offers distinct advantages over binder-based techniques. LPBF is especially suited for fabricating small parts that require high dimensional precision and excellent thermal stability. Furthermore, LPBF does not rely on imported binders or consumables, improving sustainability by primarily using in-situ materials. This process also produces parts with superior thermal resistance, making it highly advantageous for the harsh Lunar environment [24, 211].

For instance, in a recent study, Iantaffi et al. [211] investigated the additive manufacturing of Lunar regolith using LPBF with the LMS-1 simulant. They developed a process regime map and identified that the highest quality of sintering occurred at an energy density of 1.5 ± 0.5 J/mm^2, which yielded no more than 47% relative density and a compressive strength of approximately 5 MPa [211]. In another work, Caprio et al. [214] employed LPBF to process the NU-LHT-2M simulant, identifying a printable process window at laser powers of 50–60 W and scan speeds of 200–225 mm/s. Interestingly, the highest compressive strength of 31.4 MPa at roughly 37% relative density is achieved at the edge of this feasible process range ($P = 50$ W, $v_{\text{scan}} = 225$ mm/s) [214]. Similarly, Shi et al. [215] explored LPBF of the OPRH2N simulant and observed that increasing the recoating speed improved powder bed quality. Their parameter study, covering laser powers of 75–90 W and scan speeds of 180–260 mm/s, revealed a general trend in which relative density increased with higher energy density within the tested range [215].

However, despite the trials conducted in the literature, the success of parts fabricated through LPBF of regolith has been limited. Several challenges remain. For instance, the laser coupling efficiency of fiber lasers is generally poor with ceramic-based materials, and particularly with regolith [2, 24]. In addition, the poor flowability and limited layer uniformity of regolith powders hinder effective recoating during the build process [215, 216]. The heterogeneous particle chemistry of regolith presents further difficulties, especially due to the significant differences in melting points and thermal expansion coefficients among its constituent phases [212, 217]. Moreover, as regolith composition varies across different Lunar regions, exploring various simulants can provide valuable insights into the influence of particle size distribution (PSD), morphology, cohesion, chemical composition, and printing conditions on the quality of fabricated parts [24, 217, 218]. Addressing these challenges requires further targeted research.

In this work, we investigate the LPBF of OPRH2N Lunar regolith simulant under a range of processing conditions. To improve powder spreading and laser coupling, we also examine the feasibility of enhancing printability by incorporating 20 wt% Invar 36 as a metallic additive. Invar is selected as it can potentially be produced in-situ on the Moon through suitable resource extraction and alloying processes. To the best of our knowledge, this is the most comprehensive and detailed study reported to date on the LPBF of the OPRH2N simulant. It is also the first study to investigate the influence of metallic additives on the processability of this material in LPBF, building on the approach reported in [2]. The findings of this research provide valuable insights into the LPBF of Lunar regolith and have significant implications for advancing sustainable in-space manufacturing (ISM) and enabling future space exploration.

5.2 Materials and methods

5.2.1 Regolith simulant

This study employs the OPRH2N Lunar–highlands regolith simulant, formulated to approximate the modal mineralogy of Apollo highlands soils. The simulant is dominated by plagioclase-bearing anorthosite (∼70 wt%) with a subordinate basaltic fraction (∼30 wt%), reflecting the feldspar-rich character of Lunar highland material. The bulk oxide composition of the powder lot used is summarized in Table 5.1.

Table 5.1: Bulk oxide composition of the OPRH2N Lunar–highlands simulant used in this work. Values are in wt%. "Balance" denotes minor/trace oxides.

Oxide	**wt%**
SiO_2	47.89
Al_2O_3	27.06
CaO	14.19
Fe_2O_3	3.68
MgO	2.84
Na_2O	2.43
TiO_2	0.52
K_2O	0.25
P_2O_5	0.20
MnO	0.06
Balance	0.88

5.2.2 Selection criteria for the metallic additive

To improve laser–matter coupling, powder flowability, and to mitigate thermal-expansion mismatch among silicate constituents, we investigate the addition of a metallic phase. To preserve LBMC cost relevance, the additive fraction is limited to 20 wt%. Candidate metals are screened using three criteria: (i) *in situ* accessibility on the Moon with minimal Earth-supplied inputs; (ii) a coefficient of thermal expansion (CTE) compatible with silicate phases to reduce residual stresses and crack formation during solidification; and (iii) high absorptivity at the processing wavelength to stabilize the melt pool. With respect to ISRU, plausible extraction routes from regolith include molten-regolith electrolysis (MRE), carbothermal reduction (CR), and molten-salt electrolysis (MSE) [24]. Common targets are Si (abundant in mare and highlands), Fe and Ti (mare-basalt rich), and Al and Ca (highlands-anorthosite rich). Considering Lunar availability, CTE compatibility, and optical absorptivity, Ti-, Fe-, and Al-based systems are promising. Kenny et al. [219] demonstrate a single-layer regolith–metal composite using Inconel 718. However, Inconel 718 contains ∼50–55 wt% Ni, 17–21 wt% Cr, 4.75–5.50 wt% Mo, and 2.80–3.30 wt% Nb (elements scarce on the Moon), which limits ISRU practicality.

As an ISRU-lean alternative, we select Invar 36 (Fe–36 wt% Ni) as the metallic additive. The alloy is primarily Fe and Ni: Fe can be produced at high yield via MRE/CR/MSE, and Ni may be accessed from meteoritic materials or, if necessary, supplied in small quantities. Invar 36 exhibits an exceptionally low CTE, reducing thermal mismatch with the silicate matrix, and a relatively high near-IR absorptivity that can raise the effective absorptivity of Lunar-highlands regolith, promoting melt-pool stability and lowering defect incidence. Key properties for OPRH2N and Invar 36 are summarized in Table 5.2. In this work, Invar 36 is used at 20 wt%.

Table 5.2: Selected physical properties of the OPRH2N Lunar–highlands simulant and Invar 36 used in this work. Densities reported in $\mathrm{g\,cm^{-3}}$.

Property	**Invar 36**	**OPRH2N simulant**
Coefficient of thermal expansion, CTE [K^{-1}]	1×10^{-6}–2×10^{-6}	5.4×10^{-6}–15.3×10^{-6}
Laser absorptivity, A_m [–]	0.55–0.65	0.05–0.20
Density, ρ [$\mathrm{g\,cm^{-3}}$]	8.05	2.74–3.00
Melting temperature, T_m [K]	~ 1700	1400–1900
Vaporization temperature, T_v [K]	N/A	2300–3300

Regolith simulant preparation for LPBF

Prior to LPBF, the OPRH2N simulant is conditioned to achieve a powder state suitable for uniform spreading and stable processing. First, the powder is sieved to isolate a target particle-size fraction; material finer than 30 μm and coarser than 40 μm is removed to keep the 30–40 μm cut, which lies within a desirable processability range for LPBF.

Residual moisture is a critical variable because it degrades flowability and increases cohesion, hindering the formation of consistent layers. To reduce water content, powders are annealed (dry-baked) at 200 °C for 2, 3, and 6 h, and the associated mass loss is measured to quantify drying effectiveness. Results are summarized in Table 5.3.

Powder cohesion analysis

Powder flow behavior is characterized with a rotating-drum rheometer (Granudrum, Granutools, Liège, Belgium). Prior to testing, the regolith simulant is rolled in a sealed canister to homogenize

Table 5.3: Mass measurement results under different treatment conditions

Treatment Conditions		**Resulting mass measurements**			
Annealing time (hr)	**Temperature (°C)**	**Initial mass (g)**	**Final mass (g)**	**Mass loss (g)**	**Remaining mass (%)**
2	200	500.46	498.99	1.47	99.71
3	200	500.00	498.56	1.44	99.71
6	200	500.00	498.07	2.93	99.61

the blend. During measurement, the drum is rotated at controlled speeds (2–60 rpm) while a CCD camera captures the free-surface profile; image analysis yields the dynamic angle of repose and the cohesive index. Each condition is tested in triplicate to assess repeatability.

5.2.3 Powder mixing

The Lunar regolith simulant is blended with Invar 36 at 80/20 wt% (regolith/Invar). Powders are loaded into a sealed metal canister, pre-mixed by hand, and then tumbled on a roller mill for 1.5 h to promote homogeneous mixing.

5.2.4 Scanning electron microscopy (SEM)

OPRH2N powders are imaged using a Tescan VEGA-II XMU scanning electron microscope (SEM). Because the regolith is non-conductive, samples are mounted on conductive carbon tape to minimize charging during imaging.

5.2.5 Printing process

All experiments are performed on a Renishaw AM 400 laser powder bed fusion (LPBF) system operating in argon. The machine employs a modulated laser with a dwell time of 10 μs. Builds are carried out on reduced-build-volume plates made of fused silica and aluminum. Two recoating tools are evaluated: the standard elastomer (rubber) blade supplied with the AM 400 and a cylindrical rod-type metal recoater. Following [220], the effective power P_{eff} and effective scan velocity v_{eff} for a point-exposure strategy are

$$P_{\text{eff}} = P \, \frac{t_e}{t_e + t_d}, \tag{29}$$

$$v_{\text{eff}} = \frac{p_d}{t_e + t_d}, \tag{30}$$

where P is the commanded laser power, t_e is the exposure time per point, t_d is the dwell time between points (10 μs in this study), and p_d is the point (pulse) spacing.

An investigation of LPBF studies on Lunar regolith simulants informs the initial process window [211, 214, 215]. Shi et al. [215] print up to 40 layers using the OPRH2N simulant with a 150 μm layer thickness, reporting improved outcomes at higher energy inputs and a maximum part density of 2.70 $\mathrm{g\,cm^{-3}}$. Iantaffi et al. [211] investigate LMS-1 and identify five regimes (no deposition, balling, sintered, vitrification, vaporization). They find the optimal window in the sintered regime and show that re-scanning helps. Printing on aluminum rather than ceramic substrates reduces delamination.

Printing is conducted on the reduced-build-volume (RBV) plate. A custom metal rod recoater is used to improve spreading of angular, low-flow powders. For feasibility screens (Prints 1–3 and 6–7), small cylinders are used to increase sample throughput (3 mm diameter, 12 mm height). After identifying a workable window, larger cylinders are produced (6 mm diameter, 12 mm height; Prints 4–5).

The majority of conditions target the sintering regime reported in the literature and are refined iteratively across prints.

Print 1 (silica substrate). A broad parameter space is explored for the initial assessment. Layer thickness is 30 μm. The minimum calibrated machine power is 40 W, so larger beam diameters are used to lower energy input. Varied ranges are: $40 < P_{\text{eff}} < 55$ W, $0.15 < v_{\text{eff}} < 0.30$ $\mathrm{m\,s^{-1}}$, beam diameter 100–300 μm. Outcomes indicate excessive energy input with glassy features.

Print 2 (silica substrate). To reduce volumetric energy density (VED), v_{eff} is increased to 0.30–1.20 $\mathrm{m\,s^{-1}}$ and the layer thickness to 150 μm. Power remains 40–55 W; beam diameters follow Print 1.

Print 3 (aluminum substrate). Repeat of Print 2 on aluminum. No meaningful change in adhesion is observed compared to silica, so aluminum is used thereafter.

Print 4 (aluminum substrate; re-scan study). A subset of successful recipes from Prints 2–3 is re-tested using larger cylinders to gauge scalability. Beam diameter is fixed at 200 μm and layer thickness at 150 μm. The matrix covers $P_{\text{eff}} = 40$–55 W and $v_{\text{eff}} = 0.15$–0.35 $\text{m}\,\text{s}^{-1}$. Sixteen parameter sets are built, followed by a second set of sixteen with an immediate re-scan using $P_{\text{eff}} = 40$ W and $v_{\text{eff}} = 0.30$ $\text{m}\,\text{s}^{-1}$ (lowest VED).

Print 5 (location sensitivity; aluminum substrate). Seven recipes from Print 4 are selected and each built in four distinct locations on the plate to probe spatial sensitivity. Power matches Print 4; velocities are 0.15–0.30 $\text{m}\,\text{s}^{-1}$.

Prints 6–7 (regolith + Invar 36, 20 wt%). A 20 wt% Invar 36 addition is introduced to improve flowability and thermal conduction. Print 6 performs an initial sweep based on the Print 2 window, updated using the thermo-physical characteristics of the blend. However, the samples overheat and vaporize, indicating that the method used is not transferable to the metal-containing powder. Print 7 repeats the Print 2 parameters exactly with the regolith–Invar mixture to confirm this behavior.

5.2.6 Micro–computed tomography (micro-CT)

Printed specimens are characterized for internal defects by X-ray computed tomography (Zeiss Xradia 520 Versa) at an isotropic voxel size of 6 μm. Reconstructed volumes are imported into Dragonfly 3.0 (Object Research Systems, Montreal, QC) for visualization and quantification.

Two representative specimens are selected for detailed analysis: *Part 2* from *Print 5* (regolith only; highest integrity in the regolith series) and *Part 51* from *Print 7* (regolith + Invar; most intact example of the blend). Unless otherwise noted, “porosity” refers to the closed-pore fraction within the cropped region of interest.

5.3 Results and discussion

Powder cohesion analysis

The Granudrum results are shown in Fig. 5.1(a) (dynamic angle of repose) and Fig. 5.1(b) (cohesive index). The dynamic angle of repose represents the slope of the flowing free surface; lower values indicate better flowability and, by extension, fewer recoating difficulties in LPBF. Likewise, a lower cohesive index corresponds to more regular flow, with conventional qualitative bands of: good (< 10), fair/passable (10–30), and poor/very poor (> 30).

Across the tested speeds, the dynamic angle of repose remains relatively high, with only a modest downward trend at higher rpm. Error bars are substantial at low–mid speeds, indicating pronounced run-to-run variability and intermittent avalanching, both symptomatic of cohesive, friction-dominated flow. This behavior implies that forming uniform layers during printing is likely to be challenging.

The cohesive-index plot reinforces this picture. From $\sim$5 to 35 rpm, the index consistently sits in the poor/very-poor regime (> 30), indicating strong interparticle cohesion. A marked improvement occurs around 40–50 rpm, where the index drops into the fair/passable band ($\approx$10–30), before rising again at $\geq$55 rpm, a range not generally used for LPBF recoating. The partial improvement at intermediate speeds is consistent with enhanced aeration/agitation reducing cohesive bridges within the bulk [221]. Annealing dries the powder, removing residual moisture that otherwise raises friction and cohesion [221, 222]. Nevertheless, cohesion remains high, which is plausibly explained by the existence of fine particles and the associated increase in particle–particle contacts [222, 223].

Micrography of the powder

Secondary-electron SEM images of the OPRH2N regolith simulant (300$\times$ and 1000$\times$) reveal a highly angular, faceted morphology comprising platy and elongate shards spanning from a few micrometres to > 100 μm. Fracture-dominated surfaces show step edges and asperities, and many large fragments are decorated with fines (< 10 μm), indicating a broad, multimodal particle-size distribution. Irregular shapes and rough surfaces increase interparticle contact area and mechanical interlocking, while fines raise electrostatic attractions. Together, these effects promote cohesive, friction-dominated flow, consistent with the high dynamic angles and cohesive indices measured by Granudrum. For LPBF, this morphology implies reduced packing efficiency, spatial variability in local bed density, and greater recoater shear demand. Micro-roughness and fines may also modestly enhance optical absorption through multiple scattering.

5.3.1 Observations during the printing process

Print 0 (initial trial) Pure regolith is processed using a rubber recoater on a silica build plate. The build is aborted due to poor powder spreading arising from low flowability and high inter-particle

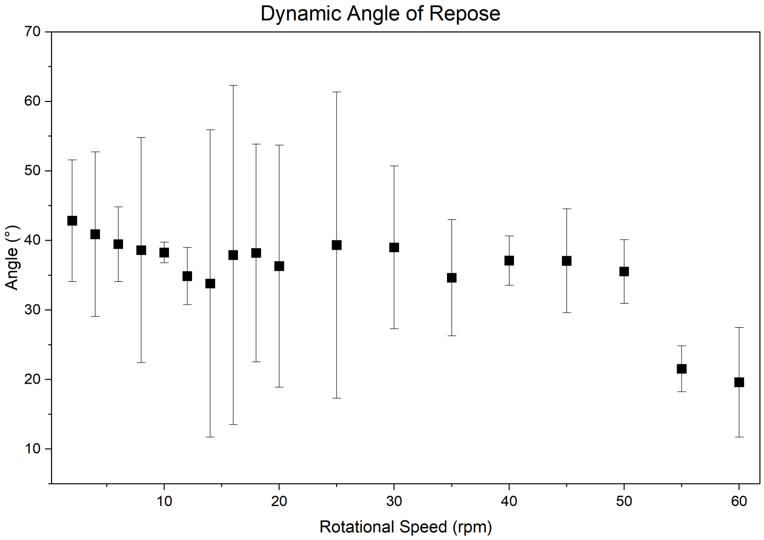

(a) Dynamic angle of repose vs. rotational speed (rpm). Error bars: triplicate variability. Lower angles indicate better flow; values remain relatively high across most speeds.

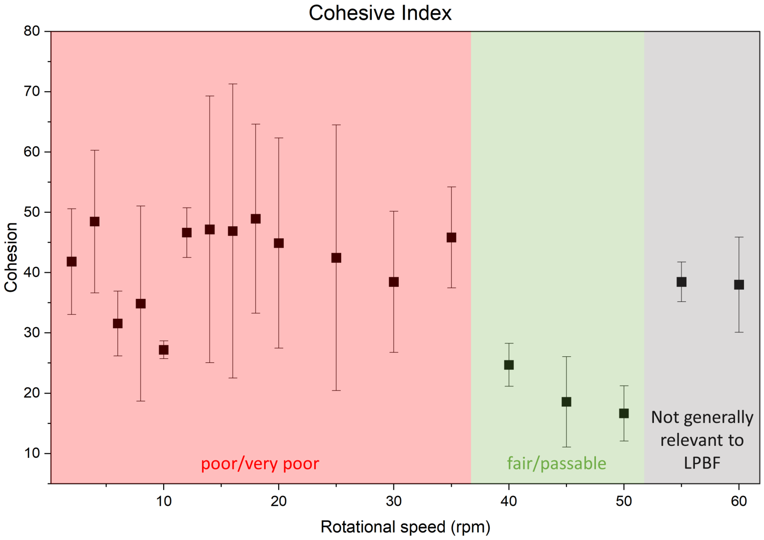

(b) Cohesive index vs. rotational speed (rpm) with qualitative regions: good < 10, fair/passable 10–30, poor/very poor > 30. Cohesion is high at 5–35 rpm, improves at 40–50 rpm, and rises again $\geq$55 rpm (generally not used in LPBF).

Figure 5.1: Granudrum rotating-drum rheometry of OPRH2N simulant after annealing. Together, (a) and (b) indicate limited flowability and elevated cohesion in LPBF-relevant speed ranges, implying challenging recoating behavior.

cohesion. Friction with the rubber blade jams the spreader, dislodging it from its mount.

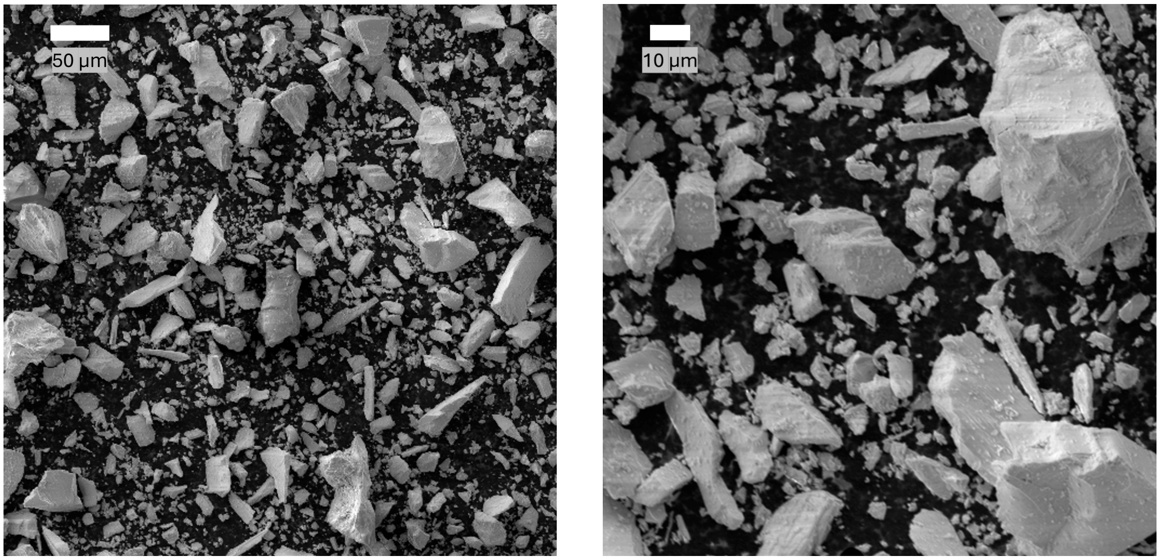

(a) OPRH2N powder at 300× magnification. The field shows angular, platy shards with abundant adherent fines; scale bar: 50 μm.

(b) OPRH2N powder at 1000× magnification. Rough fracture surfaces and fines (< 10 μm) are evident; scale bar: 10 μm.

Figure 5.2: Secondary-electron SEM of the OPRH2N regolith simulant used for Prints 1–5. Angular morphology and fines illustrate the origins of cohesive, friction-dominated flow observed in rheometry.

Print 1 All settings are retained except the recoater and layer thickness: the rubber blade is replaced with an in-house machined cylindrical steel recoater, and the nominal layer thickness is increased from 30 μm to 150 μm. Powder spreading is improved markedly, attributable to lower blade–powder friction. However, specimens exhibit extensive vitrification (glassy appearance) after a few layers, prompting build termination. This response indicates operation at an energy input above the solid-state sintering window [211].

Print 2 Hardware, powder handling, and substrate conditions are unchanged from Print 1. Laser parameters are reduced to lower the volumetric energy input and intentionally target a sintering (rather than melting) regime. Many builds still require early termination due to defect initiation and growth (most commonly interlayer cracking and local swelling) that progress to partial detachment from the bed. The most complete and geometrically stable parts are obtained for Samples 1, 17, 19, 20, and 50–53. When the energy input is too low, neck growth is insufficient, yielding fragile "green" bodies prone to interlayer cracking, and when it is excessive, localized vitrification and thermal-expansion mismatch cause swelling and early loss of adhesion.

Print 3 Print 3 replicates the Print 2 parameter matrix on an aluminum-alloy build plate to isolate substrate effects. No systematic improvement in bed adhesion is detected relative to the porous silica plate. As in Print 2, several builds are terminated early due to cracking and swelling, although some complete with acceptable integrity: Samples 2, 3, 4, 17, 18, 50, and 51. Two competing mechanisms may offset each other: (i) silica has a closer affinity to regolith, potentially aiding interfacial adhesion; (ii) aluminum's higher thermal conductivity enhances heat extraction, reducing thermal stresses and the chance of defect formation. Given the availability, flatness, and thermal uniformity of aluminum, and to ensure consistency, we perform subsequent prints on the aluminum plate.

Print 4 Print 4 scales the geometry to twice the diameter and height used in Print 3 in order to investigate size effects under otherwise similar settings. In addition, a subset of samples employ double exposure (rescanning). The second pass uses a constant energy input to assess whether track homogenization can improve layer continuity. Despite the relatively low energy input for the second exposure, the cumulative dose (from the first and second laser scanning) remains high. This raises the local temperature and the dwell time, promotes viscous spreading and vitrification of surface asperities, and leads to swelling and warping. As a result, most rescanned builds are terminated early. Only one rescanned specimen (Sample 23) completes successfully. Sample 23 has a comparatively large unprinted buffer around it, which reduces lateral heat accumulation and minimizes recoater interference from neighboring parts.

A substantial fraction of other build aborts in Print 4 are attributable to powder-spreading disturbances rather than intrinsically poor melt settings. Specifically, all specimens in the row closest to the powder hopper (Samples 1 to 6) are completed, while only three in the second row (Samples 9, 11, 14) are finished, and none in the remaining rows survive other than Sample 23. This pattern is consistent with position-dependent flowability. The first row encounters the freshest powder and the earliest, cleanest recoater pass. Downstream rows experience increased blade or roller drag across partially sintered surfaces and nascent ridges at the edges of upstream parts, which can cause local powder starvation, streaking, and bed nonuniformity. The effect is amplified when the local energy input is high enough to overheat the top surface, so powder catches on roughened features as the recoater traverses.

Among completed specimens, geometric fidelity correlates with the applied energy input and the local thermal history. Lower to intermediate energy inputs favor porous, necked microstructures that are dimensionally closer to the CAD but remain mechanically weak. Higher energy input, including cumulative effects from rescanning and heat accumulation, produces a vitrified (glassy) surface and measurable distortion. Sample 4 exhibits the best overall geometric compliance despite a vitrified skin, which suggests that its parameter set balances surface energy input and scan-path heat distribution more favorably than adjacent conditions.

Failure morphology also repeats across builds. Most specimens fracture from the build-plate side. In one representative case, the coupon is split into three radial petals that open from the bottom, and the exposed faces are the original first layers. This behavior is attributed to limited preheat and the resulting constrained-sintering stresses. As early layers shrink during neck growth while being rigidly constrained by the plate, tensile hoop stresses accumulate. Large through-thickness thermal gradients during layer cycling further elevate these stresses, so radial cracks nucleate at the interface and propagate upward. A heated build plate is expected to reduce these gradients and the associated stress. In addition, reducing part packing density to mitigate neighbor-induced heat accumulation and recoater interactions should further decrease the incidence of swelling and bottom-initiated cracking.

Print 5 Seven recipes from Print 4 are selected and each built in four distinct locations on the plate to probe spatial sensitivity. Power matches Print 4 and velocities are 0.15–$0.30\ \mathrm{m\,s^{-1}}$. The overall trends are consistent with the previous round. Specifically, Samples 1–6, which are located closest to the powder hopper, again survive to completion. Several specimens in the second row also progress well and approach the end of the build; however, they are terminated due to sudden flowability issues that disrupt powder spreading. No specimens fabricated using the re-scanning strategy survive. This outcome reinforces the interpretation from Print 4 that survivability is strongly correlated with part position and the associated powder delivery conditions. The repeatability of these position-dependent results confirms that powder-spreading limitations, rather than process parameter variability, are the dominant factor governing print success under the present setup.

Print 6 This print evaluates the effect of adding 20 wt% Invar 36 to the OPRH2N simulant. We revert to the rubber recoater because the steel rod recoater attracts the Invar-bearing powder via its magnetic response, which impairs spreading and causes local powder starvation. Visual inspection indicates that fine regolith particles adhere to Invar surfaces by electrostatic attraction, limiting any gain in flowability and diminishing the expected improvement in laser coupling despite the metal phase's higher absorptivity. In combination with the rubber recoater, this behavior yields flowability that is slightly worse than in the previous prints with pure regolith.

Printing parameters are adjusted to match the effective heat input and scan speed of Print 2, with blend properties estimated by a weighted average of the thermo-physical values for OPRH2N and Invar 36. This surrogate proves insufficient to reproduce the actual process behavior. As shown in Fig. 5.3, the build exhibits an excessively bright melt pool and vigorous spatter, consistent with overheating and partial vaporization. These observations indicate that the Print 2 strategy does not transfer to the Invar blend with the method used, and that the operating point shifts into a vitrification or vaporization regime because the mixture experiences an energy density above the required level. For subsequent trials, the energy input should be reduced to limit heat accumulation.

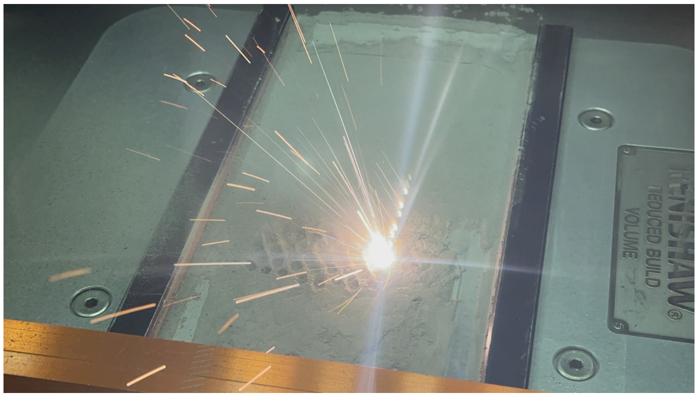

Figure 5.3: Print 6 (OPRH2N + 20 wt% Invar). The image shows a bright melt pool with extensive spatter, consistent with overheating and partial vaporization.

Print 7 Print 7 repeats the Print 2 parameter set exactly with the regolith–Invar mixture to test transferability. The outcomes largely mirror the pure-regolith trials at comparable parameters and geometry. Several builds are terminated early due to cracking and swelling, while a subset are completed with acceptable integrity (Samples 3, 4, 17, 18, 20, 22, 23, 40, 49, 50, 51). The process

Table 5.4: Successful samples by print.

Print	Successful samples
1	N/A
2	1, 17, 19, 20, 50, 51, 52, 53
3	2, 3, 4, 17, 18, 50, 51
4	1, 2, 3, 4, 5, 6, 9, 11, 14, 23
5	1, 2, 3, 4, 5, 6
6	N/A
7	3, 4, 17, 18, 20, 22, 23, 40, 49, 50, 51

window that yields surviving parts is therefore similar to that identified in Prints 2 and 3.

A potential explanation is that fine regolith particles coat the Invar particles, reducing the expected difference in optical and thermal response. Consequently, the addition neither improves laser coupling in a meaningful way nor provides sufficient heat-sink behavior to moderate thermal gradients and residual stresses. In practical terms, the process continues to operate as regolith sintering, with metallic particles remaining solid throughout. Because the Invar melting point is substantially higher than the onset of regolith softening/vitrification, increasing input to melt the metal would drive the regolith into overheating and vaporization, as observed in Print 6. Overall, under the present conditions, the net effect of adding 20 wt% Invar 36 appears limited.

5.3.2 Micro-CT of the samples

X-ray micro–CT of a representative OPRH2N cylinder shows a predominantly dense core surrounded by a more porous shell with surface-connected voids and several through-thickness cracks (Fig. 5.4). After threshold-based segmentation (removing open surfaces), the apparent relative density is 95.8% (porosity $\approx 4.2\%$). Correlating CT with visual inspection indicates that the core is largely vitrified (glassy), whereas the outer regions appear less glassy. This radial contrast is consistent with LPBF thermal fields: (i) in the interior, track overlap and reduced heat loss promote heat accumulation and slower cooling, pushing the silicate phase above the softening/melting range and enabling glass formation; (ii) near the sidewall, higher heat extraction (radiation/convection to the gas, conduction to cooler powder, and edge effects from incomplete hatch overlap) keeps peak temperatures and dwell times lower, favoring sintering with limited vitrification. The outer shell also shows larger, near-spherical pores and unbonded pockets associated with spreading defects and denudation, while the dense, glassy core contains longitudinal cracks that originate at the perimeter and propagate inward, consistent with tensile residual stresses generated by differential shrinkage between vitrified and sintered zones. Together, these features point to strong thermal gradients and nonuniform packing. Mitigation should involve lowering the effective energy input to avoid over-vitrification and crack formation.

X-ray micro-CT of a representative regolith-Invar cylinder indicates a predominantly *sintered* microstructure rather than a melted/vitrified one (Fig. 5.5). In the slices, dark/black regions are pores (low attenuation), bright/white speckles are higher-density Invar particles, and mid-gray corresponds primarily to the sintered regolith phase. Relative to the pure-regolith specimen, the regolith-Invar sample shows a more uniform core, a thinner porous shell, and far fewer through-thickness cracks. Pores are mostly rounded and intergranular, consistent with solid-state neck growth and limited liquid-phase flow. We do not observe large glassy domains or the long, opening cracks characteristic of vitrified cores. This behavior is attributed to (i) a lower volumetric energy density used for the build and (ii) the smaller geometry (about half the height and diameter), both of which accelerate cooling and shorten the thermal dwell above the softening range of the silicate phase. The faster thermal cycle promotes solid-state necking between particles and limits liquid flow, which prevents the heavy vitrification and residual-stress cracking seen in the pure-regolith cylinder. The apparent relative density here is 92.8%. The lower value relative to the pure-regolith case is consistent with sintering-dominated consolidation rather than melt-driven densification.

In this sample, the pore density is slightly higher near the edges, but the interior also contains pores, unlike the strongly edge-biased porosity in the pure regolith. This more uniform distribution reflects more uniform heating and faster overall cooling in the smaller regolith-Invar geometry. From a processing standpoint, these CT observations suggest that the regolith–Invar window is closer to solid-state sintering. Incremental increases in energy input or modest preheat could densify the porosity, but pushing too far risks reintroducing melt-driven defect modes (coalesced pores and post-solidification cracking) observed in the pure-regolith case.

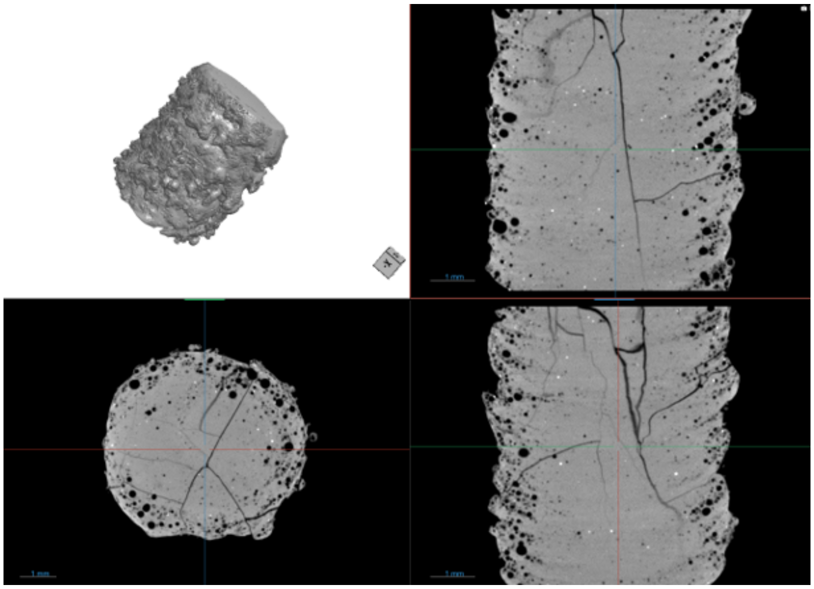

Figure 5.4: X-ray micro–CT of a representative OPRH2N (pure regolith) cylinder, shown as an isometric rendering with orthogonal slices. The images reveal a dense, vitrified core surrounded by a more porous outer shell containing surface-connected voids and several through-thickness cracks. The radial contrast reflects strong thermal gradients during LPBF: interior heat accumulation promotes glass formation, whereas the sidewall experiences lower peak temperatures and limited vitrification, leading to sintering-dominated consolidation and larger edge-localized pores.

5.4 Conclusion and future work

This study evaluated the laser powder bed fusion (LPBF) of the OPRH2N Lunar–highlands regolith simulant across a broad process space and assessed the feasibility of improving printability via a 20 wt% Invar 36 additive. In line with Lunar in-situ resource utilization (ISRU) constraints, the work emphasizes binder-free processing with minimal imported consumables. To our knowledge, this is the most detailed LPBF investigation of OPRH2N to date and the first to examine a metallic-additive route for this simulant.

Key findings.

- **Powder flowability is the primary limiter.** OPRH2N shows high cohesion at LPBF-relevant speeds (consistent with angular shards and fines), making uniform recoating difficult. Print survivability correlated with local powder delivery (parts near the hopper fared better). A steel-rod recoater and thicker layers improved spreading relative to a rubber blade.

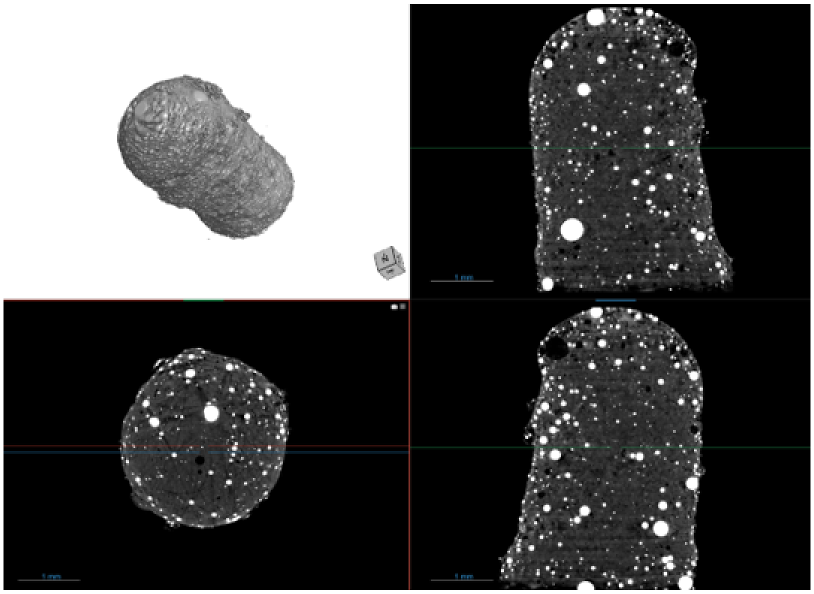

Figure 5.5: X-ray micro–CT of a regolith–Invar cylinder, highlighting pores (dark), dense Invar particles (bright), and the sintered regolith phase (mid-gray). In contrast to the pure-regolith cylinder, the microstructure is predominantly sintered with a thinner porous shell, fewer through-thickness cracks, and a more uniform interior. These features reflect the reduced volumetric energy density and smaller part geometry, which favor rapid cooling and solid-state neck growth rather than vitrification-driven consolidation.

- **A narrow, low-energy sintering window exists but is easy to overshoot.** Most complete parts arose at low–intermediate inputs; rescans largely degraded outcomes via cumulative heating (vitrification, swelling, early aborts). Switching silica to aluminum plates did not yield a systematic adhesion benefit. Micro-CT of a representative pure-regolith sample revealed a vitrified, crack-prone core surrounded by a more porous shell; the high apparent relative density ($\sim$97%) stems from melt-driven gap filling but accompanies residual-stress cracking. These trends favor lower effective energy, wider spacing, and thermal management/preheat over rescanning.

- **Adding 20 wt% Invar 36 did not deliver net gains under the present setup.** Electrostatic adhesion of fines to Invar particles limited the additive's ability to improve powder–laser coupling and flowability. At reduced inputs, the blend behaved as solid-state sintering (representative density $\sim$92.8%) with fewer through-thickness cracks than vitrified pure-regolith parts, but without the anticipated densification or coupling benefits.

Future work. Priorities include: (i) flowability enhancement (e.g., low-dosage silica-based flow aids to create micro-spacers and limit moisture bridges), (ii) tighter thermal control (plate preheat and reduced part packing) to remain within the sintering window, and (iii) post-processing (sinter-annealing and/or polymer/metal infiltration) to close pores and mitigate cracking. Expanded powder/part characterization (SEM/EDS, CT-based defect statistics) together with mechanical testing (compression, hardness) on geometrically consistent coupons will quantify strength–defect trade-offs and guide parameter refinement.

For comparison, FFF of PEEK/LRS composites demonstrates higher technology maturity than LPBF of pure regolith for in-space manufacturing. FFF entails lower system and process complexity, scales more readily to large components, integrates better with robotic platforms, and, importantly, exhibits lower energy demand. In this study it also achieved higher strength and adequate dimensional accuracy for the targeted parts, whereas LPBF was more sensitive to build size increases and even millimeter-scale upscaling introduced notable process challenges. Given its relatively lower dependence on Earth-supplied consumables, LPBF of regolith remains promising for small, high-precision components that require high thermal resilience, especially if challenges in process control and powder conditioning are addressed. With continued advances, LPBF can complement FFF by enabling niche, high-temperature, fine-feature parts, while FFF remains the primary option for structural, large-format regolith-based manufacturing. Ultimately, neither process is universally superior, and the choice depends on mission logistics, part scale, performance targets, and available resources.

Overall, these results clarify the dominant failure modes in LPBF of highlands-type regolith and outline a practical pathway for powder handling, thermal management, and targeted post-processing, toward robust, binder-free regolith parts relevant to sustainable in-space manufacturing.

Chapter 6

Conclusion and Future Work

Synthesis of Key Findings across Research Phases

Material extrusion additive manufacturing of PEEK/regolith (Phases I–II). Phase I established the feasibility of filament manufacture and FFF of a high-temperature thermoplastic (PEEK) reinforced with 30 wt% LMS-1D Lunar regolith simulant (LRS), using a commercial neat-PEEK filament as a baseline. At 30 wt% LRS, tensile strength decreased by 26.8% relative to neat PEEK, driven primarily by an ∼21% reduction in relative density. Nevertheless, the measured strength of 67.0 MPa remains adequate for many practical applications. The LRS addition increased the Young's modulus from ∼917.3 MPa (neat PEEK) to 1152.1 MPa, a 25.6% gain.

Phase II extended the same route with refined filament making and print conditions to enable higher LRS loadings and improved part quality. Filaments compounded via twin-screw extrusion yielded dense feedstocks ($> 96\%$) and mechanically coherent filaments from 10 to 50 wt% LRS. As-printed porosity increased with LRS content (from $< 1\%$ for neat PEEK to ∼7.5% at 50 wt%), consistent with higher melt viscosity and flow resistance. Regolith raised matrix crystallinity (from ∼17.4% to ∼20.5%) and increased elastic modulus by $+6$–41%, while reducing delamination/warping. Tensile strength declined progressively from ∼107 MPa (neat) to ∼90 MPa at 40 wt% and then sharply to ∼70 MPa at 50 wt%. Post-print annealing at 300 °C improved density and stiffness up to ∼30 wt% LRS, with diminishing returns at higher loadings due to entrapped porosity. Overall, ∼40 wt% LRS emerged as a practical trade-off for mechanically critical parts, whereas 50 wt% remains printable for non-critical or shielding applications.

Defect-aware simulation of PEEK/LRS composites (Phase III). A hierarchical modeling framework, comprising (i) a homogenized matrix with fine-particle estimates, (ii) RVE-based defect-free composite models, and (iii) defect-aware RVEs was employed to analyze composite behavior across particle–matrix ratios. The defect-free models captured the measured stiffness trends with acceptable accuracy up to ~ 40 wt% LRS. The model–experiment divergence increased from $\sim 3.50\%$ at 10 wt% to $\sim 10.13\%$ at 40 wt%, consistent with acceptable but rising defect density, and then jumped to $\sim 55.35\%$ at 50 wt%. This large mismatch at 50 wt% is most plausibly attributed to the combined effects of a higher critical void fraction and weak/partly debonded inter-bead interfaces. The simulations quantify how tall interfacial defects and polymer-starved welds may suppress load transfer, even under in-plane loading, producing a clear modulus knock-down attributable to realistic AM defect ensembles. Once a weak, percolating network forms, all load paths traverse it, so the macroscopic response is likely governed by that soft network rather than by volume-average phase properties. The effective modulus might become series-controlled (compliant segments lie in series along the load path, their compliances may add, and the thinnest or softest ligaments could potentially dominate). Practically, this appears as (i) an increased area fraction and contiguity of high-stress zones at weld roots, (ii) reduced minimum ligament width along layer boundaries, and (iii) the emergence of a single connected weak cluster across the field of view. This connectivity provides a plausible explanation for the non-monotonic trend: stiffness rises with filler to $\sim 40\ \mathrm{wt}\%$, then falls at $50\ \mathrm{wt}\%$.

LPBF feasibility with OPRH2N (Phase IV). LPBF outcomes were dominated by powder flowability and thermal management. Rotating-drum rheometry and SEM confirmed cohesive, angular OPRH2N powders with fines, leading to position-sensitive recoating and a narrow low-energy sintering window that was easy to overshoot. Rescans generally raised cumulative heat (vitrification, swelling, early aborts). Micro-CT of representative pure-regolith cylinders showed a vitrified, crack-prone core surrounded by a porous shell. High apparent density (via melt gap-filling) coexisted with residual-stress cracking. A 20 wt% Invar 36 blend did not yield net gains under the present hardware/recipes. Electrostatic adhesion of fines to Invar particles reduced the additive's effectiveness in improving flowability and powder–laser coupling. At reduced inputs, the blend operated in a solid-state sintering regime (representative relative density $\sim 92.8\%$), exhibiting fewer through-thickness cracks but lacking the higher densification observed in the melting/vitrification regime.

Overall, FFF of PEEK/LRS composites appears to demonstrate higher technology maturity than LPBF of pure regolith for in-space manufacturing. FFF entails lower system and process complexity, scales more readily to large components, integrates better with robotic platforms, and importantly, exhibits lower energy demand. In this study it also achieved higher strength and adequate dimensional accuracy for the targeted parts, whereas LPBF was more sensitive to build size increases and even millimeter-scale upscaling introduced notable process challenges. Given its relatively lower dependence on Earth-supplied consumables, LPBF of regolith remains promising for small, high-precision components that require high thermal resilience, especially if challenges in process control and powder conditioning are addressed. With continued advances, LPBF can complement FFF by enabling niche, high-temperature, fine-feature parts, while FFF remains the primary option for structural, large-format regolith-based manufacturing. Ultimately, neither process is universally superior and the choice depends on mission logistics, part scale, performance targets, and available resources.

Future Work

A. PEEK/LRS composites.

(1) **Compression molding of PEEK/LRS.** It will be valuable to pursue hot-press consolidation of compounded pellets for PEEK and PEEK/LRS. In this configuration, compression molding is expected to reduce entrapped porosity and eliminate inter-bead weld defects, simplify the thermal history by removing toolpath-induced cold interfaces, and yield cleaner microstructures that enable more direct comparison with FE predictions that rely on simplifying assumptions. A press-based route would also lower system complexity relative to AM and help establish an upper-bound baseline for properties at each LRS loading.

(2) **Pushing the 50 wt% limit (only if mission-justified).** It will be informative to investigate targeted increases in melt temperature and residence time, coupled with slower, steadier extrusion using a high-torque extruder and larger nozzle diameters. The anticipated benefit is a higher ISRU fraction with reduced reliance on Earth-supplied polymer, while the corresponding trade-offs include elevated risk of thermal oxidation and chain scission, wider heat-affected zones that promote dimensional drift, and crystallinity-driven brittleness. A DOE framing would bound a safe window across melt temperature, chamber temperature, speed, nozzle size, and cooling rate, while tracking porosity, interlayer adhesion, crystallinity, and oxidation markers (e.g., DSC).

(3) **Broaden materials space: polymers and simulants.** It will be useful to replicate the workflow with space-grade matrices (e.g., PEKK, ULTEM/PEI) and multiple LRS types in order

to isolate the influence of simulant chemistry and particle-size distribution. Comparative assessment should highlight both gains and added difficulties arising from differences in resin viscosity, crystallization kinetics, and PSD-driven rheology.

(4) **Post-processing, with feasibility checks.** It will be worthwhile to evaluate lower-energy densification routes (such as staged sinter-anneals, warm pressing, and localized roller compaction), before considering higher-overhead options. Hot isostatic pressing (HIP) should be contemplated only where mass and energy budgets support Lunar deployment; otherwise, Earth-side HIP baselines can be developed to quantify the theoretical ceiling on properties.

(5) **Advanced characterization of thermal, mechanical, and interfacial behavior.** It will be useful to expand the characterization toolbox to more fully capture the mechanisms that govern stiffness loss, interlayer bonding, and particle to matrix interaction in high regolith content composites. Dynamic mechanical analysis (DMA) can quantify storage and loss moduli, glass transition behavior, and temperature dependent damping, providing insight into interphase mobility and the softening of weld zones. Thermomechanical analysis (TMA) can measure dimensional stability and thermal expansion mismatch between layers, while thermogravimetric analysis (TGA) can clarify polymer degradation onset and thermal stability. Melt flow index (MFI) measurements on compounded pellets can further establish how filler content influences melt viscosity and flowability. Mechanical testing in the z direction, including through thickness tensile tests or interlaminar fracture tests, can directly evaluate weld integrity and quantify the influence of particle loading on layer to layer adhesion. Interface focused methods such as cryo fracture field emission scanning electron microscopy (FE-SEM), ion-polished cross-section imaging, nanoindentation modulus mapping, focused ion beam scanning electron microscopy (FIB-SEM) tomography, and X-ray micro-computed tomography (micro-CT) can be employed to assess nanoscale debonding, interfacial porosity, stiffness gradients within the interphase, and three-dimensional pore connectivity.

B. Modeling: toward predictive design.

(1) **3D microstructure-resolved FE.** It will be valuable to extend the present 2D mid–section

analysis to statistically representative 3D RVEs that capture through–thickness weld topology, bead curvature, and defect connectivity. Fully 3D simulations would help avoid possible scaling discrepancies that may arise due to inherent 2D/3D differences. In addition, future work should explore improved boundary conditions beyond the current fixed constraint at the left edge of the specimen. Implementing periodic boundary conditions (PBCs) in both in-plane and through-thickness directions, or employing mixed periodic–kinematic constraints, would better mimic an infinite repeating microstructure and reduce artificial stress concentrations induced by fixed boundaries. These boundary conditions are more physically representative of printed rasters embedded within a continuous material field. The transition to 3D RVEs will likely require advanced numerical techniques and/or higher-performance computing hardware (e.g., GPU-based solvers, reduced-order modeling, or adaptive mesh refinement) to manage the substantially higher element counts and defect complexity. Incorporating experimentally derived pore size and shape distributions obtained from micro-CT, together with interface traction–separation laws calibrated from fracture testing or micro digital image correlation (micro DIC), would enable more realistic predictions. In parallel, advanced characterization such as FE-SEM, FIB-SEM tomography, ion-polished cross-sections, and nanoindentation modulus mapping can be used to assess particle–matrix interfacial quality and interlayer bonding. Complementary Z-direction tensile testing may further quantify interface strength.

(2) **Process physics coupling.** It will be useful to develop process-to-structure models for (i) filament extrusion and cooling (non-Newtonian flow, heat transfer, crystallization kinetics), (ii) bead–bead sintering and neck growth, and (iii) transient chamber thermal fields. Calibration with IR thermography and embedded thermocouples during FFF can then be propagated to predict resulting stiffness and strength.

(3) **Uncertainty quantification (UQ).** It will be important to propagate variability in particle size/morphology, porosity, and interface toughness through to mechanical response, thereby establishing conservative design allowables for Lunar service.

C. LPBF of regolith.

(1) **Flowability enhancement.** It will be valuable to assess low-dosage silica-based flow aids (fumed or precipitated silica) alongside controlled fines reduction to lower the cohesive index without compromising ISRU mass budgets. Screening should confirm that flow gains do not degrade downstream consolidation or contaminate chemistry.

(2) **Process window refinement.** It will be useful to systematically map low-energy sintering regimes using in-situ sensing (photodiodes, coaxial cameras) to identify the onset of vitrification and the margins to overheating. The resulting maps can guide stable, power-efficient builds.

(3) **Post-processing.** It will be worthwhile to apply sinter-annealing cycles tailored to the silicate softening range and, where justified, polymer or metal infiltration to close pores and heal microcracks. Micro-CT statistics (pore size and connectivity, crack density) should be used to quantify the resulting gains.

D. Environmental durability and mission integration.

(1) **Lunar-relevant conditioning.** It will be important to expose PEEK/LRS and LPBF coupons to Lunar day–night thermal cycling, vacuum outgassing checks, UV/γ radiation, and dust abrasion, so that degradation pathways and knock-down factors are quantified under mission-realistic stressors.

(2) **Scale-up and autonomy.** It will be valuable to demonstrate PEEK/LRS printing with a mobile robotic 3D printer for large-scale components, then transition to large-format extrusion and modular presses for panels/brackets. Integrating in-line quality monitoring (vision, IR) with simple closed-loop controllers under constrained power will help avoid defects and stabilize build quality.

Closing Remarks

This work provides an experimentally anchored and simulation-informed map of what is feasible today for ISRU-relevant polymer–regolith composites and regolith laser sintering on Earth-based hardware with consideration of Lunar constraints. The results show that (i) carefully managed PEEK/LRS extrusion can deliver structurally useful parts for Lunar-based manufacturing, (ii) defect-aware modeling is essential to interpret and predict performance at high loadings, and (iii) LPBF of regolith is presently flow- and heat-limited but can progress via powder handling, thermal control, and post-processing. Together, these findings establish a practical foundation for sustainable in-space manufacturing and a clear research agenda to translate materials and processes to the Lunar surface.

Bibliography

[1] Nevine Tagscherer, André Marcel Bär, Swen Zaremba, and Klaus Drechsler. Mechanical analysis of parameter variations in large-scale extrusion additive manufacturing of thermoplastic composites. *Journal of Manufacturing and Materials Processing*, 6(2):36, 2022.

[2] Mohammad Azami, Armin Siahsarani, Amir Hadian, Zahra Kazemi, Davood Rahmatabadi, Seyed Farshid Kashani-Bozorg, and Karen Abrinia. Laser powder bed fusion of alumina/fe–ni ceramic matrix particulate composites impregnated with a polymeric resin. *Journal of Materials Research and Technology*, 24:3133–3144, 2023.

[3] Mohammad Azami, Pierre-Lucas Aubin Fournier, and Krzysztof Skonieczny. Additive manufacturing of polyether ether ketone (peek)/lunar regolith composites via fused filament fabrication. In *Earth and Space 2024: Engineering for Extreme Environments*, pages 976–986. 2024.

[4] Mohammad Azami, Pierre-Lucas Aubin-Fournier, and Krzysztof Skonieczny. Enhancing economical lunar-based manufacturing by incorporating lunar regolith into polyether–ether–ketone (peek): material development, additive manufacturing, and characterization. *Progress in Additive Manufacturing*, pages 1–7, 2025.

[5] Exolith. Lunar mare dust (lms-1d) moon dirt simulant - fact sheet. Accessed on 2023/10/19.

[6] Pradyot Patnaik. *Handbook of inorganic chemicals*, volume 529. McGraw-Hill New York, 2003.

[7] William M Haynes. *CRC handbook of chemistry and physics*. CRC press, 2016.

[8] James F Shackelford and William Alexander. *CRC materials science and engineering handbook*. CRC press, 2000.

[9] Robert B Cook. Handbook of mineralogy. *Rocks and Minerals*, 76(4):278, 2001.

[10] DG Isaak, JD Carnes, OL Anderson, H Cynn, and E Hake. Elasticity of tio2 rutile to 1800 k. *Physics and Chemistry of Minerals*, 26(1):31–43, 1998.

[11] RE Pacalo and EK Graham. Pressure and temperature dependence of the elastic properties of synthetic mno. *Physics and chemistry of minerals*, 18(1):69–80, 1991.

[12] David M Roessler and Donald R Huffman. Magnesium oxide (mgo). In *Handbook of optical constants of solids*, pages 919–955. Elsevier, 1997.

[13] Sergio Speziale, Sean R Shieh, and Thomas S Duffy. High-pressure elasticity of calcium oxide: A comparison between brillouin spectroscopy and radial x-ray diffraction. *Journal of Geophysical Research: Solid Earth*, 111(B2), 2006.

[14] B Bridge, ND Patel, and DN Waters. On the elastic constants and structure of the pure inorganic oxide glasses. *physica status solidi (a)*, 77(2):655–668, 1983.

[15] Xiaoxin Wu, Yan Zhang, Junkai Zhang, Ran Liu, Jinghai Yang, Bin Yang, Hongxin Xu, and Yanz Ma. High pressure x-ray diffraction study of sodium oxide (na2o): Observations of amorphization and equation of state measurements to 15.9 gpa. *Journal of Alloys and Compounds*, 823:153793, 2020.

[16] Samantha Hill. An updated list of space missions: Current and upcoming voyages. *astronomy.com*, 2024.

[17] Jeff Foust. Success, failure and something in between for lunar landers. *SpaceNews Magazine*, 2023.

[18] Koorosh R Araghi. Nasa lunar in-situ resource utilization technology overview. In *Korean Institute of Geoscience and Mineral Resources (KIGAM) ISRU Workshop*, 2022.

[19] Gerald Jerry Sanders and Julie Kleinhenz. Progress review of nasa lunar isru development: 2019 to 2025. In *Luxembourg Space Resources Week*. European Space Research and Technology Centre, 2025.

[20] HR Abedi, A Zarei Hanzaki, M Azami, M Kahnooji, and D Rahmatabadi. The high temperature flow behavior of additively manufactured inconel 625 superalloy. *Materials Research Express*, 6(11):116514, 2019.

[21] Zahra Kazemi and Craig A Steeves. Uncertainty quantification of local elastic properties in additively manufactured materials for topology optimization applications using machine learning. *Acta Mechanica*, pages 1–10, 2025.

[22] Zahra Kazemi and Craig A Steeves. Uncertainty quantification in material properties of additively manufactured materials for application in topology optimization. In *ASME International Mechanical Engineering Congress and Exposition*, volume 86656, page V003T04A009. American Society of Mechanical Engineers, 2022.

[23] Miguel Hoffmann and Alaa Elwany. In-space additive manufacturing: A review. *Journal of Manufacturing Science and Engineering*, 145(2):020801, 2023.

[24] Mohammad Azami, Zahra Kazemi, Sare Moazen, Martine Dubé, Marie-Josée Potvin, and Krzysztof Skonieczny. A comprehensive review of lunar-based manufacturing and construction. *Progress in Aerospace Sciences*, 150:101045, 2024.

[25] Jinbo Li, Pierre-Lucas Aubin-Fournier, and Krzysztof Skonieczny. Slaam: Simultaneous localization and additive manufacturing. *IEEE Transactions on Robotics*, 37(2):334–349, 2020.

[26] Maxim Isachenkov, Svyatoslav Chugunov, Iskander Akhatov, and Igor Shishkovsky. Regolith-based additive manufacturing for sustainable development of lunar infrastructure–an overview. *Acta Astronautica*, 180:650–678, 2021.

[27] Ruilin Li, Guoqing Zhou, Kang Yan, Jun Chen, Daqing Chen, Shangyue Cai, and Pin-Qiang Mo. Preparation and characterization of a specialized lunar regolith simulant for use in lunar

low gravity simulation. *International Journal of Mining Science and Technology*, 32(1):1–15, 2022.

[28] Robert P Mueller, Laurent Sibille, Paul E Hintze, Thomas C Lippitt, James G Mantovani, Matthew W Nugent, and Ivan I Townsend. Additive construction using basalt regolith fines. In *Earth and Space 2014*, pages 394–403. 2014.

[29] MJ Creedon, Tara Linneman, Douglas L Rickman, and Michael Effinger. Development of new lunar highland regolith simulant, nuw-lht-5m. In *Lunar Surface Innovation Consortium Spring Meeting*, 2023.

[30] Yushen Wang, Liang Hao, Yan Li, Qinglei Sun, Mingxi Sun, Yuhong Huang, Zheng Li, Danna Tang, Yijing Wang, and Long Xiao. In-situ utilization of regolith resource and future exploration of additive manufacturing for lunar/martian habitats: A review. *Applied Clay Science*, 229:106673, 2022.

[31] TJ Prater, QA Bean, RD Beshears, TD Rolin, NJ Werkheiser, EA Ordonez, RM Ryan, and FE Ledbetter III. Summary report on phase i results from the 3d printing in zero g technology demonstration mission, volume i. Technical report, 2016.

[32] Niki Werkheiser. In-space manufacturing: pioneering a sustainable path to mars. Technical report, 2015.

[33] Enea Sacco and Seung Ki Moon. Additive manufacturing for space: status and promises. *The International Journal of Advanced Manufacturing Technology*, 105:4123–4146, 2019.

[34] Angela Huang and Zheng H Zhu. An experimental investigation of microgravity conditions on fdm-based in-space polymer additive manufacturing. *Acta Astronautica*, 228:886–899, 2025.

[35] James S Moore Jr, David R Mengers, Theodore D Swanson, Reinhard Radermacher, and Frederick A Costello. Low-temperature thermal control for a lunar base. *SAE Transactions*, pages 598–612, 1990.

[36] Adam A Marek and Vincent Verney. Photochemical reactivity of pla at the vicinity of glass transition temperature. the photo-rheology method. *European Polymer Journal*, 81:239–246, 2016.

[37] Yottha Srithep, Paul Nealey, and Lih-Sheng Turng. Effects of annealing time and temperature on the crystallinity and heat resistance behavior of injection-molded poly (lactic acid). *Polymer Engineering & Science*, 53(3):580–588, 2013.

[38] Y Badr, ZI Ali, and Rasha M Khafagy. On the mechanism of low temperature glass transition in low density polyethylene films. *Radiation Physics and Chemistry*, 58(1):87–100, 2000.

[39] Andrew P Abbott, Tariq Z Abolibda, Wanwan Qu, William R Wise, and Luka A Wright. Thermoplastic starch–polyethylene blends homogenised using deep eutectic solvents. *RSC Advances*, 7(12):7268–7273, 2017.

[40] Ferdinand C Stehling and Leo Mandelkern. The glass temperature of linear polyethylene. *Macromolecules*, 3(2):242–252, 1970.

[41] Ali Reza Zanjanijam, Ian Major, John G Lyons, Ugo Lafont, and Declan M Devine. Fused filament fabrication of peek: A review of process-structure-property relationships. *Polymers*, 12(8):1665, 2020.

[42] Neil A Walter and John J Scialdone. Outgassing data for selecting spacecraft materials. Technical report, 1997.

[43] Paolo Chiggiato. Outgassing. In *CERN Accelerator School*, 2006.

[44] CAMPBELL William. Outgassing data for selecting spacecraft materials. *NASA Reference Publication 1124*, 1993.

[45] Aditya Pulipaka, Kunal Manoj Gide, Ali Beheshti, and Z Shaghayegh Bagheri. Effect of 3d printing process parameters on surface and mechanical properties of fff-printed peek. *Journal of Manufacturing Processes*, 85:368–386, 2023.

[46] Kathy C Chuang, Joseph E Grady, Robert D Draper, Euy-Sik E Shin, Clark Patterson, and Thomas D Santelle. Additive manufacturing and characterization of ultem polymers and composites. Technical report, 2015.

[47] AR McLauchlin, OR Ghita, and L Savage. Studies on the reprocessability of poly (ether ether ketone)(peek). *Journal of Materials Processing Technology*, 214(1):75–80, 2014.

[48] Alfons Pascual, Michael Toma, Panayota Tsotra, and Markus C Grob. On the stability of peek for short processing cycles at high temperatures and oxygen-containing atmosphere. *Polymer Degradation and Stability*, 165:161–169, 2019.

[49] Nathan J Gelino, Jackson L Smith, Tesia D Irwin, Thomas A Lipscomb, Evan A Bell, David I Malott, Stephen J Pfund, Leonel H Herrera, Caela G Gomes, Tracy L Gibson, et al. Selection, production, and properties of regolith polymer composites for lunar construction. In *2024 IEEE Aerospace Conference*, pages 1–21. IEEE, 2024.

[50] Jana Herzberger, Justin M Sirrine, Christopher B Williams, and Timothy E Long. Polymer design for 3d printing elastomers: Recent advances in structure, properties, and printing. *Progress in Polymer Science*, 97:101144, 2019.

[51] Steven Pollack, Chaitra Venkatesh, Martin Neff, Andrew V Healy, Guang Hu, Evert A Fuenmayor, John G Lyons, Ian Major, and Declan M Devine. Polymer-based additive manufacturing: historical developments, process types and material considerations. In *Polymer-Based Additive Manufacturing*, pages 1–22. Springer, 2019.

[52] S Mohammad H Hojjatzadeh, Niranjan D Parab, Qilin Guo, Minglei Qu, Lianghua Xiong, Cang Zhao, Luis I Escano, Kamel Fezzaa, Wes Everhart, Tao Sun, et al. Direct observation of pore formation mechanisms during lpbf additive manufacturing process and high energy density laser welding. *International Journal of Machine Tools and Manufacture*, 153:103555, 2020.

[53] Eduardo Salcedo, Dongcheon Baek, Aaron Berndt, and Jong Eun Ryu. Simulation and validation of three dimension functionally graded materials by material jetting. *Additive Manufacturing*, 22:351–359, 2018.

[54] Jacob P Moore and Christopher B Williams. Fatigue properties of parts printed by polyjet material jetting. *Rapid Prototyping Journal*, 2015.

[55] Amir Hadian, Leonard Koch, Philipp Koberg, Fateme Sarraf, Antje Liersch, Tutu Sebastian, and Frank Clemens. Material extrusion based additive manufacturing of large zirconia structures using filaments with ethylene vinyl acetate based binder composition. *Additive Manufacturing*, 47:102227, 2021.

[56] Shima Pilehvar, Marlies Arnhof, Ramón Pamies, Luca Valentini, and Anna-Lena Kjøniksen. Utilization of urea as an accessible superplasticizer on the moon for lunar geopolymer mixtures. *Journal of Cleaner Production*, 247:119177, 2020.

[57] Pragnya Kunchala and Keerti Kappagantula. 3d printing high density ceramics using binder jetting with nanoparticle densifiers. *Materials & Design*, 155:443–450, 2018.

[58] Amir Mostafaei, Amy M Elliott, John E Barnes, Fangzhou Li, Wenda Tan, Corson L Cramer, Peeyush Nandwana, and Markus Chmielus. Binder jet 3d printing—process parameters, materials, properties, modeling, and challenges. *Progress in Materials Science*, 119:100707, 2021.

[59] JC Heigel, P Michaleris, and Edward William Reutzel. Thermo-mechanical model development and validation of directed energy deposition additive manufacturing of ti–6al–4v. *Additive manufacturing*, 5:9–19, 2015.

[60] Beth E Carroll, Todd A Palmer, and Allison M Beese. Anisotropic tensile behavior of ti–6al–4v components fabricated with directed energy deposition additive manufacturing. *Acta Materialia*, 87:309–320, 2015.

[61] Altan Alpay Altun, Florian Ertl, Maude Marechal, Advenit Makaya, Antonella Sgambati, and Martin Schwentenwein. Additive manufacturing of lunar regolith structures. *Open Ceramics*, 5:100058, 2021.

[62] Carli Marsico, Marit Øilo, Jeff Kutsch, Mark Kauf, and Dwayne Arola. Vat polymerization-printed partially stabilized zirconia: Mechanical properties, reliability and structural defects. *Additive manufacturing*, 36:101450, 2020.

[63] Prahar M Bhatt, Ariyan M Kabir, Max Peralta, Hugh A Bruck, and Satyandra K Gupta. A robotic cell for performing sheet lamination-based additive manufacturing. *Additive Manufacturing*, 27:278–289, 2019.

[64] Mark Norfolk and Hilary Johnson. Solid-state additive manufacturing for heat exchangers. *Jom*, 67(3):655–659, 2015.

[65] Pedro Carreira, Fábio Cerejo, Nuno Alves, and Maria Teresa Vieira. In search of the optimal conditions to process shape memory alloys (niti) using fused filament fabrication (fff). *Materials*, 13(21):4718, 2020.

[66] Marius A Wagner, Amir Hadian, Tutu Sebastian, Frank Clemens, Thomas Schweizer, Mikel Rodriguez-Arbaizar, Efrain Carreño-Morelli, and Ralph Spolenak. Fused filament fabrication of stainless steel structures-from binder development to sintered properties. *Additive Manufacturing*, 49:102472, 2022.

[67] Shelby A Skoog, Peter L Goering, and Roger J Narayan. Stereolithography in tissue engineering. *Journal of Materials Science: Materials in Medicine*, 25(3):845–856, 2014.

[68] Ferry PW Melchels, Jan Feijen, and Dirk W Grijpma. A review on stereolithography and its applications in biomedical engineering. *Biomaterials*, 31(24):6121–6130, 2010.

[69] Jochen Schmidt, Marius Sachs, Christina Blümel, Bettina Winzer, Franziska Toni, Karl-Ernst Wirth, and Wolfgang Peukert. A novel process chain for the production of spherical sls polymer powders with good flowability. *Procedia engineering*, 102:550–556, 2015.

[70] Manfred Schmid, Antonio Amado, and Konrad Wegener. Polymer powders for selective laser sintering (sls). In *AIP Conference proceedings*, volume 1664, page 160009. AIP Publishing LLC, 2015.

[71] Nicos Kalapodis, Georgios Kampas, and Olga-Joan Ktenidou. A review towards the design of extraterrestrial structures: From regolith to human outposts. *Acta Astronautica*, 175:540–569, 2020.

[72] Athanasios Goulas, Russell A Harris, and Ross J Friel. Additive manufacturing of physical assets by using ceramic multicomponent extra-terrestrial materials. *Additive Manufacturing*, 10:36–42, 2016.

[73] Miranda Fateri, Alexandre Meurisse, Matthias Sperl, Diego Urbina, Hemanth Kumar Madakashira, Shashank Govindaraj, Jeremi Gancet, Barbara Imhof, Waltraut Hoheneder, René Waclavicek, et al. Solar sintering for lunar additive manufacturing. *Journal of Aerospace Engineering*, 32(6):04019101, 2019.

[74] Houssam A Toutanji, Steve Evans, and Richard N Grugel. Performance of lunar sulfur concrete in lunar environments. *Construction and Building Materials*, 29:444–448, 2012.

[75] Additive Manufacturing—General Principles—Terminology. Iso/astm 52900. *International Organization for Standardization: Geneva, Switzerland*, 2015.

[76] MF Arif, S Kumar, KM Varadarajan, and WJ Cantwell. Performance of biocompatible peek processed by fused deposition additive manufacturing. *Materials & Design*, 146:249–259, 2018.

[77] Shouling Ding, Bin Zou, Peng Wang, and Hongjian Ding. Effects of nozzle temperature and building orientation on mechanical properties and microstructure of peek and pei printed by 3d-fdm. *Polymer Testing*, 78:105948, 2019.

[78] Madheswaran Subramaniyan, Sivakumar Karuppan, Prakash Eswaran, Anandhamoorthy Appusamy, and A Naveen Shankar. State of art on fusion deposition modeling machines process parameter optimization on composite materials. *Materials Today: Proceedings*, 45:820–827, 2021.

[79] Guilhem Rival, Thierry Paulmier, and Eric Dantras. Influence of electronic irradiations on

the chemical and structural properties of peek for space applications. *Polymer Degradation and Stability*, 168:108943, 2019.

[80] Stefan Siarov. Additive manufacturing with engineering thermoplastics in space: recyclability and radiation protection. 2018.

[81] Kristen T Kern, Phillip C Stancil, Wynford L Harries, Edward R Long Jr, and Sheila A Thibeault. Simulated space environmental effects on a polyetherimide and its carbon fiber-reinforced composites. *Sampe Journal*, 29(3), 1993.

[82] Xiaojun Liu, Zhongde Shan, Jianhua Liu, Huanxiong Xia, Xiaohui Ao, Ailing Zou, and Siyuan Wu. Mechanical and electrical properties of additive manufactured high-performance continuous glass fiber reinforced peek composites. *Composites Part B: Engineering*, 247:110292, 2022.

[83] Michael Flanagan, David M Grogan, Jamie Goggins, Simon Appel, Keith Doyle, Sean B Leen, and CM Ó Brádaigh. Permeability of carbon fibre peek composites for cryogenic storage tanks of future space launchers. *Composites Part A: Applied Science and Manufacturing*, 101:173–184, 2017.

[84] RK Goyal, AN Tiwari, and Yuvraj Singh Negi. Microhardness of peek/ceramic micro-and nanocomposites: Correlation with halpin–tsai model. *Materials Science and Engineering: A*, 491(1-2):230–236, 2008.

[85] AA Stepashkin, DI Chukov, FS Senatov, AI Salimon, AM Korsunsky, and SD Kaloshkin. 3d-printed peek-carbon fiber (cf) composites: Structure and thermal properties. *Composites Science and Technology*, 164:319–326, 2018.

[86] Dong Yang, Yi Cao, Zhikun Zhang, Yifa Yin, and Dichen Li. Effects of crystallinity control on mechanical properties of 3d-printed short-carbon-fiber-reinforced polyether ether ketone composites. *Polymer Testing*, 97:107149, 2021.

[87] Ivan Townsend, Robert Mueller, Nathan Gelino, Jonathan Smith, Matthew Nugent, Andrew

Nick, Jason Schuler, and Bradley Buckles. Print head for regolith-polymer mixture and associated feedstock, March 1 2022. US Patent 11,260,589.

[88] Zahra Kazemi and Mohammad Azami. Overall mechanical properties of self-healing composites: Effects of microcapsules shape, volume concentration, shell thickness, and material properties. In *ASME International Mechanical Engineering Congress and Exposition*, volume 86717, page V009T12A001. American Society of Mechanical Engineers, 2022.

[89] Julia Cadorim Facenda, Marcia Borba, and Pedro Henrique Corazza. A literature review on the new polymer-infiltrated ceramic-network material (picn). *Journal of Esthetic and Restorative Dentistry*, 30(4):281–286, 2018.

[90] JP Kilroy, Conchur O Bradaigh, and C OA Semprimoschnig. Mechanical and physical evaluation of new carbon fibre/peek composites for space applications. *Sampe Journal*, 44(3):23–34, 2008.

[91] Guilhem Rival, Eric Dantras, and Thierry Paulmier. Electronic irradiation ageing in the vicinity of glass transition temperature for peek space applications. *Polymer Degradation and Stability*, 181:109305, 2020.

[92] Tengfei Liu, Mingjie Zhang, Youwei Kang, Xiaoyong Tian, Jifeng Ding, and Dichen Li. Material extrusion 3d printing of polyether ether ketone in vacuum environment: Heat dissipation mechanism and performance. *Additive Manufacturing*, 62:103390, 2023.

[93] Peng Geng, Ji Zhao, Wenzheng Wu, Wenli Ye, Yulei Wang, Shuobang Wang, and Shuo Zhang. Effects of extrusion speed and printing speed on the 3d printing stability of extruded peek filament. *Journal of Manufacturing Processes*, 37:266–273, 2019.

[94] Gunilla MK Ostberg and James C Seferis. Annealing effects on the crystallinity of polyetheretherketone (peek) and its carbon fiber composite. *Journal of Applied Polymer Science*, 33(1):29–39, 1987.

[95] Cemile Basgul, Tony Yu, Daniel W MacDonald, Ryan Siskey, Michele Marcolongo, and Steven M Kurtz. Does annealing improve the interlayer adhesion and structural integrity of

fff 3d printed peek lumbar spinal cages? *Journal of the mechanical behavior of biomedical materials*, 102:103455, 2020.

[96] Chuncheng Yang, Xiaoyong Tian, Dichen Li, Yi Cao, Feng Zhao, and Changquan Shi. Influence of thermal processing conditions in 3d printing on the crystallinity and mechanical properties of peek material. *Journal of Materials Processing Technology*, 248:1–7, 2017.

[97] Marianna Rinaldi, Tommaso Ghidini, Federico Cecchini, Ana Brandao, and Francesca Nanni. Additive layer manufacturing of poly (ether ether ketone) via fdm. *Composites Part B: Engineering*, 145:162–172, 2018.

[98] Xia Gao, Shunxin Qi, Xiao Kuang, Yunlan Su, Jing Li, and Dujin Wang. Fused filament fabrication of polymer materials: A review of interlayer bond. *Additive Manufacturing*, 37:101658, 2021.

[99] Jafar Ghorbani, Pratik Koirala, Yu-Lin Shen, and Mehran Tehrani. Eliminating voids and reducing mechanical anisotropy in fused filament fabrication parts by adjusting the filament extrusion rate. *Journal of Manufacturing Processes*, 80:651–658, 2022.

[100] Hao Wu and Joseph H Koo. Characterization of high-temperature polymers for extreme environments. In *Analysis of Flame Retardancy in Polymer Science*, pages 299–331. Elsevier, 2022.

[101] S Sundarram, Y-H Kim, and W Li. Preparation and characterization of poly (ether imide) nanocomposites and nanocomposite foams. In *Manufacturing of Nanocomposites with Engineering Plastics*, pages 61–85. Elsevier, 2015.

[102] Eugene B Caldona, John Ryan C Dizon, Robert Andrew Viers, Vincent Joseph Garcia, Zane J Smith, and Rigoberto C Advincula. Additively manufactured high-performance polymeric materials and their potential use in the oil and gas industry. *Mrs Communications*, 11(6):701–715, 2021.

[103] J Vina, EA Garcia, A Argüelles, and I Vina. The effect of moisture on the tensile and interlaminar shear strengths of glass or carbon fiber reinforced pei. *Journal of materials science letters*, 19:579–581, 2000.

[104] Yahya Abderrafai, Audrey Diouf-Lewis, Facundo Sosa-Rey, Rouhollah D Farahani, Nicola Piccirelli, Martin Lévesque, and Daniel Therriault. Additive manufacturing and characterization of high temperature thermoplastic blends for potential aerospace applications. *Composites Science and Technology*, 231:109839, 2023.

[105] Anouar El Magri, Khalil El Mabrouk, and Sébastien Vaudreuil. Preparation and characterization of poly (ether ether ketone)/poly (ether imide)[peek/pei] blends for fused filament fabrication. *Journal of Materials Science*, 56(25):14348–14367, 2021.

[106] Hao Wu, Michael Sulkis, James Driver, Amado Saade-Castillo, Adam Thompson, and Joseph H Koo. Multi-functional ultem™ 1010 composite filaments for additive manufacturing using fused filament fabrication (fff). *Additive Manufacturing*, 24:298–306, 2018.

[107] Eric L Gilmer, Craig Mansfield, John M Gardner, Emilie J Siochi, Donald G Baird, and Michael J Bortner. Characterization and analysis of polyetherimide: realizing practical challenges of modeling the extrusion-based additive manufacturing process. In *Polymer-Based Additive Manufacturing: Recent Developments*, pages 69–84. ACS Publications, 2019.

[108] Eric L Gilmer, David Anderegg, John M Gardner, Godfrey Sauti, Emilie J Siochi, Steven H McKnight, David A Dillard, Claire McIlroy, and Michael J Bortner. Temperature, diffusion, and stress modeling in filament extrusion additive manufacturing of polyetherimide: An examination of the influence of processing parameters and importance of modeling assumptions. *Additive Manufacturing*, 48:102412, 2021.

[109] Christine Ajinjeru, Vidya Kishore, John Lindahl, Zeke Sudbury, Ahmed Arabi Hassen, Brian Post, Lonnie Love, Vlastimil Kunc, and Chad Duty. The influence of dynamic rheological properties on carbon fiber-reinforced polyetherimide for large-scale extrusion-based additive manufacturing. *The International Journal of Advanced Manufacturing Technology*, 99:411–418, 2018.

[110] Bo Yuan, Qinwen Cheng, Rui Zhao, Xiangdong Zhu, Xiao Yang, Xi Yang, Kai Zhang, Yueming Song, and Xingdong Zhang. Comparison of osteointegration property between pekk and peek: Effects of surface structure and chemistry. *Biomaterials*, 170:116–126, 2018.

[111] Hatim Alqurashi, Zohaib Khurshid, Azeem Ul Yaqin Syed, Syed Rashid Habib, Dinesh Rokaya, and Muhammad Sohail Zafar. Polyetherketoneketone (pekk): An emerging biomaterial for oral implants and dental prostheses. *Journal of Advanced Research*, 28:87–95, 2021.

[112] Helena Perez-Martin, Paul Mackenzie, Alex Baidak, Conchúr M Ó Brádaigh, and Dipa Ray. Crystallinity studies of pekk and carbon fibre/pekk composites: A review. *Composites Part B: Engineering*, 223:109127, 2021.

[113] Aliza Rabinowitz, Paul M DeSantis, Cemile Basgul, Hannah Spece, and Steven M Kurtz. Taguchi optimization of 3d printed short carbon fiber polyetherketoneketone (cfr pekk). *Journal of the Mechanical Behavior of Biomedical Materials*, 145:105981, 2023.

[114] Kaifur Rashed, Abdullah Kafi, Ranya Simons, and Stuart Bateman. Effects of fused filament fabrication process parameters on tensile properties of polyether ketone ketone (pekk). *The International Journal of Advanced Manufacturing Technology*, 122(9-10):3607–3621, 2022.

[115] Kaifur Rashed, Abdullah Kafi, Ranya Simons, and Stuart Bateman. Optimization of material extrusion additive manufacturing process parameters for polyether ketone ketone (pekk). *The International Journal of Advanced Manufacturing Technology*, 126(3-4):1067–1091, 2023.

[116] AI SpaceFactory. Marsha. `https://spacefactory.ai/marsha`, Accessed: 2024-07-03.

[117] Steven D Anderson and Jekan Thangavelautham. Solar-powered additive manufacturing in extraterrestrial environments. In *2021*, pages 732–744. 2021.

[118] MC Roman, Michael R Fiske, Shadi Nazarian, Melodie Yashar, Jason Ballard, Michael Bentley, Platt Boyd, and Amanda Moon Adams. From 3d-printing lunar and mars habitats to

affordable sustainable housing on earth. In *50th International Conference on Environmental Systems*, number MSFC-E-DAA-TN79169, 2020.

[119] Designboom. AI SpaceFactory's MARSHA wins NASA's 3D-Printed Habitat Challenge. `https://www.designboom.com/`, 2019. Accessed: 2024-07-03.

[120] AI SpaceFactory. Lina. `https://spacefactory.ai/lina`, Accessed: 2024-07-03.

[121] Marius A Wagner, Jona Engel, Amir Hadian, Frank Clemens, Mikel Rodriguez-Arbaizar, Efrain Carreño-Morelli, Jeffrey M Wheeler, and Ralph Spolenak. Filament extrusion-based additive manufacturing of 316l stainless steel: Effects of sintering conditions on the microstructure and mechanical properties. *Additive Manufacturing*, 59:103147, 2022.

[122] Frank Clemens, Fateme Sarraf, Aurelio Borzì, Antonia Neels, and Amir Hadian. Material extrusion additive manufacturing of advanced ceramics: Towards the production of large components. *Journal of the European Ceramic Society*, 43(7):2752–2760, 2023.

[123] Miranda Fateri, Ali Kaouk, Aidan Cowley, Stefan Siarov, Manel Vera Palou, Fernando Gobartt González, Romain Marchant, Samantha Cristoforetti, and Matthias Sperl. Feasibility study on additive manufacturing of recyclable objects for space applications. *Additive Manufacturing*, 24:400–404, 2018.

[124] Carleton B Moore, Charles F Lewis, Everett K Gibson, and Walter Nichiporuk. Total carbon and nitrogen abundances in lunar samples. *Science*, 167(3918):495–497, 1970.

[125] Jalava Kalle, Korpi Joni, Strakh Alexander, and Orkas Juhani. Potential and challenges of fused granular fabrication in patternmaking. *International Journal of Metalcasting*, pages 1–8, 2023.

[126] JR Sarasua and J Pouyet. Recycling effects on microstructure and mechanical behaviour of peek short carbon-fibre composites. *Journal of materials science*, 32:533–536, 1997.

[127] Maha Zaghdoudi, Anja Kömmling, Matthias Jaunich, and Dietmar Wolff. Scission, crosslinking, and physical relaxation during thermal degradation of elastomers. *Polymers*, 11(8):1280, 2019.

[128] Celia Martín-Pérez, Daniel Rodriguez-Del Rosario, Elena Rodríguez-Senín, and Noelia González-Castro. Fused granulated fabrication (fgf) processing study for novel scf/lmpaek recycled material to manufacture aeronautic structural parts. In *International Manufacturing Science and Engineering Conference*, volume 86601, page V001T01A003. American Society of Mechanical Engineers, 2022.

[129] Victrex. Accessed on 2023-10-10.

[130] Amishga Alphonius, Alexandre Bonami, Taha Bouhmouch, Rodrigue Cadena, Amina Chelabi, Amani Cheriti, Christophe Croisetiere, Loic Cummings-Jomphe, Mehdi Djitli, Mathew Karam, Olivier Leclair, Francois Michaud, Rani Naaman, Nayer Nassif, Jerome Igeon, Raphael Plante, Philippe Rioux, Marc-Antoine Robillard, Jad Tahri, Emilie Vidal-Klassen, Marc Zaki, Antoine Letarte, Olivier Duchesne, Sare Moazen, Feng Yang Chen, and Marie-Josee Potvin. Lunar 3d printing with in-situ resources. Technical report, Polytechnique Montreal, 2023.

[131] Antoine Missout. Flow control of molten material and gas extraction via electrolysis, March 1 2022. US Patent 11,260,590.

[132] Kilncore Company. Accessed: 2023-10-11.

[133] Marcus G Langseth Jr, Stephen J Keihm, and John L Chute Jr. Heat flow experiment. *NASA. Johnson Space Center Apollo 17 Prelim. Sci. Rept.*, 1973.

[134] Elise Bon. *Structural opportunities for glass*. PhD thesis, Massachusetts Institute of Technology, 2003.

[135] Miranda Fateri, Andreas Gebhardt, and Maziar Khosravi. Experimental investigation of selective laser melting of lunar regolith for in-situ applications. In *ASME International Mechanical Engineering Congress and Exposition*, volume 56185, page V02AT02A008. American Society of Mechanical Engineers, 2013.

[136] Miranda Fateri and Andreas Gebhardt. Process parameters development of selective laser

melting of lunar regolith for on-site manufacturing applications. *International Journal of Applied Ceramic Technology*, 12(1):46–52, 2015.

[137] Athanasios Goulas and Ross J Friel. 3d printing with moondust. *Rapid Prototyping Journal*, 22(6):864–870, 2016.

[138] Athanasios Goulas, Jon GP Binner, Daniel S Engstrøm, Russell A Harris, and Ross J Friel. Mechanical behaviour of additively manufactured lunar regolith simulant components. *Proceedings of the Institution of Mechanical Engineers, Part L: Journal of Materials: Design and Applications*, 233(8):1629–1644, 2019.

[139] Athanasios Goulas, Jon GP Binner, Russell A Harris, and Ross J Friel. Assessing extraterrestrial regolith material simulants for in-situ resource utilisation based 3d printing. *Applied Materials Today*, 6:54–61, 2017.

[140] Leonardo Caprio, Ali Gökhan Demir, Barbara Previtali, and Bianca Maria Colosimo. Determining the feasible conditions for processing lunar regolith simulant via laser powder bed fusion. *Additive Manufacturing*, 32:101029, 2020.

[141] William M Steen and Jyotirmoy Mazumder. *Laser material processing*. springer science & business media, 2010.

[142] Laurent Sibille, Rob Mueller, Beverly Kemmerer, and Tommy Lipscomb. Vacuum sintering of highland simulant csm-lht-1g. In *XXIII Meeting Space Resources Roundtable (SRR)*, 2023.

[143] Rui Wang, Guofu Qiao, and Guangping Song. Additive manufacturing by laser powder bed fusion and thermal post-treatment of the lunar-regolith-based glass-ceramics for in-situ resource utilization. *Construction and Building Materials*, 392:132051, 2023.

[144] Stephen J Indyk and Haym Benaroya. A structural assessment of unrefined sintered lunar regolith simulant. *Acta astronautica*, 140:517–536, 2017.

[145] Hailong Liao, Junjie Zhu, Shijie Chang, Gang Xue, Jingxi Pang, and Haihong Zhu. Lunar regolith-alsi10mg composite fabricated by selective laser melting. *Vacuum*, 187:110122, 2021.

[146] Juan-Carlos Ginés-Palomares, Miranda Fateri, Eckehard Kalhöfer, Tim Schubert, Lena Meyer, Nico Kolsch, Monika Brandić Lipińska, Robert Davenport, Barbara Imhof, René Waclavicek, et al. Laser melting manufacturing of large elements of lunar regolith simulant for paving on the moon. *Scientific Reports*, 13(1):15593, 2023.

[147] Melodie Yashar, W Elshanshoury, M Esfandabadi, D Gomez, A Guzeev, V Netti, A Rajkumar, E Jensen, J Ballard, and M Moghimi Esfandabadi. Project olympus: off-world additive construction for lunar surface infrastructure. In *50th International Conference on Environmental Systems*, pages 12–15, 2021.

[148] Jensen E. Project olympus: Off-planet construction. https://lsic.jhuapl.edu/uploadedDocs/focus-files/2291-ICON%20Olympus%20LSIC%20Slides%2031JAN2024.pdf, 2023. Accessed: July 5, 2024.

[149] Jiao Xu, Xiaoyong Sun, Hongzhong Cao, Hong Tang, Honglin Ma, Lei Song, Xiongyao Li, Xuanmin Duan, and Jianzhong Liu. 3d printing of hypothetical brick by selective laser sintering using lunar regolith simulant and ilmenite powders. In *9th International Symposium on Advanced Optical Manufacturing and Testing Technologies: Subdiffraction-limited Plasmonic Lithography and Innovative Manufacturing Technology*, volume 10842, pages 38–48. SPIE, 2019.

[150] Alex Ellery. Generating and storing power on the moon using in situ resources. *Proceedings of the Institution of Mechanical Engineers, Part G: Journal of Aerospace Engineering*, 236(6):1045–1063, 2022.

[151] David R Criswell and Peter A Curreri. Photovoltaics using in situ resource utilization for heds. In *Space 98*, pages 286–289. 1998.

[152] Andrew Blakers, Ngwe Zin, Keith R McIntosh, and Kean Fong. High efficiency silicon solar cells. *Energy Procedia*, 33:1–10, 2013.

[153] Alexandre Freundlich, Alex Ignatiev, Charles Horton, Michael Duke, P Curreri, and Laurent Sibille. Manufacture of solar cells on the moon. In *Conference Record of the Thirty-first IEEE Photovoltaic Specialists Conference, 2005.*, pages 794–797. IEEE, 2005.

[154] TE Girish and S Aranya. Photovoltaic power generation on the moon: problems and prospects. In *Moon: Prospective Energy and Material Resources*, pages 367–376. Springer, 2012.

[155] Alex Ellery, Ian Mellor, Priti Wanjara, and Melchiorri Conti. Metalysis fray farthing chen process as a strategic lunar in situ resource utilization technology. *New Space*, 10(2):224–238, 2022.

[156] Igor Yadroitsev, Ina Yadroitsava, Anton Du Plessis, and Eric MacDonald. *Fundamentals of laser powder bed fusion of metals*. Elsevier, 2021.

[157] Esmaeil Sadeghi, Paria Karimi, Soroush Momeni, Mohsen Seifi, Anders Eklund, and Joel Andersson. Influence of thermal post treatments on microstructure and oxidation behavior of eb-pbf manufactured alloy 718. *Materials characterization*, 150:236–251, 2019.

[158] Joe T Howell, John C Fikes, Carole A McLemore, and James E Good. On-site fabrication infrastructure to enable efficient exploration and utilization of space. In *59th International Aeronautical Congress (IAC) 2008*, number MSFC-2120-1, 2008.

[159] CA McLemore, JC Fikes, KS McCarley, JE Good, JP Kennedy, and SD Gilley. From lunar regolith to fabricated parts: technology developments and the utilization of moon dirt. In *Earth & Space 2008: Engineering, Science, Construction, and Operations in Challenging Environments*, pages 1–11. 2008.

[160] Solar sinter. `https://kayserworks.com/798817030644`. Accessed: 2024-06-29.

[161] Takashi Nakamura and Benjamine Smith. Solar thermal system for lunar isru applications: Development and field operation at mauna kea, hi. In *49th AIAA Aerospace Sciences Meeting including the New Horizons Forum and Aerospace Exposition*, page 433, 2011.

[162] EH Cardiff and BC Hall. A dust mitigation vehicle utilizing direct solar heating. In *Joint annual meeting of lunar exploration analysis group-international conf. on exploration and utilization of the moon-space resources roundtable*, 2008.

[163] James R Gaier. The effects of lunar dust on eva systems during the apollo missions. Technical report, 2007.

[164] Sandra Wagner. The apollo experience lessons learned for constellation lunar dust management. Technical report, 2006.

[165] Sarah Noble. Assessing the dangers of moon dust. In *Second national conference on USGS human*, 2007.

[166] Noreen Khan-Mayberry. The lunar environment: Determining the health effects of exposure to moon dusts. *Acta Astronautica*, 63(7-10):1006–1014, 2008.

[167] Paul Hintze, Jerry Curran, and Teddy Back. Lunar surface stabilization via sintering or the use of heat cured polymers. In *47th AIAA Aerospace Sciences Meeting including The New Horizons Forum and Aerospace Exposition*, page 1015, 2009.

[168] Alexandre Meurisse, A Makaya, C Willsch, and M Sperl. Solar 3d printing of lunar regolith. *Acta Astronautica*, 152:800–810, 2018.

[169] A. Carter, A. T. Brewer, and T. Southard. Solar additive manufacturing with lunar regolith. In *Proceedings of the XXIII Meeting Space Resources Roundtable (SRR)*, 2023.

[170] Sungwoo Lim and Mahesh Anand. Numerical modelling of the microwave heating behaviour of lunar regolith. *Planetary and Space Science*, 179:104723, 2019.

[171] Miranda Fateri, Aidan Cowley, Matthias Kolbe, Oriane Garcia, Matthias Sperl, and Samantha Cristoforetti. Localized microwave thermal posttreatment of sintered samples of lunar simulant. *Journal of Aerospace Engineering*, 32(4):04019051, 2019.

[172] Lawrence A Taylor and Thomas T Meek. Microwave sintering of lunar soil: properties, theory, and practice. *Journal of Aerospace Engineering*, 18(3):188–196, 2005.

[173] Lawrence August Taylor, Donghwa Shin Taylor, Richard Franklin Perez, and Michael A DiGiuseppe. Apparatus for in-situ microwave consolidation of planetary materials containing nano-sized metallic iron particles, May 25 2010. US Patent 7,723,654.

[174] Lawrence A Taylor, Carlé Pieters, Allan Patchen, Dong-Hwa S Taylor, Richard V Morris, Lindsay P Keller, and David S McKay. Mineralogical and chemical characterization of lunar highland soils: Insights into the space weathering of soils on airless bodies. *Journal of Geophysical Research: Planets*, 115(E2), 2010.

[175] Lawrence A Taylor. Generation of native fe in lunar soil. *Engineering, Construction, and Operations in Space*, pages 67–77, 1988.

[176] M Barmatz, D Steinfeld, D Winterhalter, D Rickman, and MA Weinstein. Microwave heating studies and instrumentation for processing lunar regolith and simulants. In *44th Annual Lunar and Planetary Science Conference*, number 1719, page 1223, 2013.

[177] Martin Barmatz, David Steinfeld, Shelley B Begley, Daniel Winterhalter, and Carlton Allen. Microwave permittivity and permeability measurement on lunar soils. In *42nd Lunar and Planetary Science Conference*, number JSC-CN-22645, 2011.

[178] M Barmatz, D Steinfeld, D Winterhalter, D Rickman, R Gustafson, D Butts, and M Weinstein. Microwave permittivity and permeability measurements on lunar simulants. In *43rd Annual Lunar and Planetary Science Conference*, number 1659, page 1050, 2012.

[179] M Barmatz, D Steinfeld, M Anderson, and D Winterhalter. 3d microwave print head approach for processing lunar and mars regolith. In *45th Annual Lunar and Planetary Science Conference*, number 1777, page 1137, 2014.

[180] Scott A Howe, Brian H Wilcox, Christopher McQuin, Julie Townsend, Richard R Rieber, Martin Barmatz, and John Leichty. Faxing structures to the moon: Freeform additive construction system (facs). In *AIAA SPACE 2013 conference and exposition*, page 5437, 2013.

[181] Sungwoo Lim, Vibha Levin Prabhu, Mahesh Anand, and Lawrence A Taylor. Extra-terrestrial construction processes–advancements, opportunities and challenges. *Advances in Space Research*, 60(7):1413–1429, 2017.

[182] Young-Jae Kim, Byung-Hyun Ryu, Hyun Woo Jin, Jangguen Lee, and Hyu-Soung Shin.

Microwave sintering of lunar regolith simulant for manufacturing building elements. In *2021*, pages 985–991. 2021.

[183] Young-Jae Kim, Byung Hyun Ryu, Hyunwoo Jin, Jangguen Lee, and Hyu-Soung Shin. Microstructural, mechanical, and thermal properties of microwave-sintered kls-1 lunar regolith simulant. *Ceramics International*, 47(19):26891–26897, 2021.

[184] Arup Dey, Isnala Nanjin Roan Eagle, and Nita Yodo. A review on filament materials for fused filament fabrication. *Journal of manufacturing and materials processing*, 5(3):69, 2021.

[185] Marianna Rinaldi, Federico Cecchini, Lucia Pigliaru, Tommaso Ghidini, Francesco Lumaca, and Francesca Nanni. Additive manufacturing of polyether ether ketone (peek) for space applications: A nanosat polymeric structure. *Polymers*, 13(1):11, 2020.

[186] M Anand, Ian A Crawford, M Balat-Pichelin, S Abanades, W Van Westrenen, G Péraudeau, R Jaumann, and W Seboldt. A brief review of chemical and mineralogical resources on the moon and likely initial in situ resource utilization (isru) applications. *Planetary and Space Science*, 74(1):42–48, 2012.

[187] Yoshinobu Nakamura, Miho Yamaguchi, Masayoshi Okubo, and Tsunetaka Matsumoto. Effect of particle size on mechanical properties of epoxy resin filled with angular-shaped silica. *Journal of applied polymer science*, 44(1):151–158, 1992.

[188] R Abraham, SP Thomas, S Kuryan, J Isac, KT Varughese, and S Thomas. Mechanical properties of ceramic-polymer nanocomposites. *Express Polym Lett*, 3(3):177–89, 2009.

[189] Hao Wu, WP Fahy, Steven Kim, H Kim, Nanzhu Zhao, Louis Pilato, Abdullah Kafi, Stuart Bateman, and JH Koo. Recent developments in polymers/polymer nanocomposites for additive manufacturing. *Progress in Materials Science*, 111:100638, 2020.

[190] Carlos Montes, Kaylin Broussard, Matthew Gongre, Neven Simicevic, Johanna Mejia, Jessica Tham, Erez Allouche, and Gabrielle Davis. Evaluation of lunar regolith geopolymer binder as a radioactive shielding material for space exploration applications. *Advances in Space Research*, 56(6):1212–1221, 2015.

[191] Grant Heiken, David Vaniman, and Bevan M French. *Lunar sourcebook: A user's guide to the Moon*. Number 1259. Cup Archive, 1991.

[192] Andrea Zocca, Janka Wilbig, Anja Waske, Jens Günster, Martinus Putra Widjaja, Christian Neumann, Mélanie Clozel, Andreas Meyer, Jifeng Ding, Zuoxin Zhou, et al. Challenges in the technology development for additive manufacturing in space. *Chinese Journal of Mechanical Engineering: Additive Manufacturing Frontiers*, 1(1):100018, 2022.

[193] Lawrence A Taylor, Carle M Pieters, and Daniel Britt. Evaluations of lunar regolith simulants. *Planetary and Space Science*, 126:1–7, 2016.

[194] Caterina Iantaffi, Chu Lun Alex Leung, George Maddison, Eral Bele, Samy Hocine, Rob Snell, Alexander Rack, Martina Meisnar, Thomas Rohr, Iain Todd, et al. Laser additive manufacturing of lunar regolith simulant: New insights from in situ synchrotron x-ray imaging. *Additive Manufacturing*, 101:104711, 2025.

[195] Timothy Yap, Nathaniel Heathman, Tim Phillips, Joseph Beaman, and Mehran Tehrani. Additive manufacturing of polyaryletherketone (paek) polymers and their composites. *Composites Part B: Engineering*, 266:111019, 2023.

[196] David J Blundell and BN Osborn. The morphology of poly (aryl-ether-ether-ketone). *Polymer*, 24(8):953–958, 1983.

[197] Yen-Huei Lai, MC Kuo, JC Huang, and M Chen. On the peek composites reinforced by surface-modified nano-silica. *Materials Science and Engineering: A*, 458(1-2):158–169, 2007.

[198] A Arzak, JI Eguiazabal, and J Nazabal. Effect of annealing on the properties of poly (ether ether ketone). *Polymer Engineering & Science*, 31(8):586–591, 1991.

[199] Erika Lannunziata, Giovanna Colucci, Paolo Minetola, and Alberto Giubilini. Effect of annealing treatment and infill percentage on 3d-printed peek samples by fused filament fabrication. *The International Journal of Advanced Manufacturing Technology*, 131(9):5209–5222, 2024.

[200] Zhiyuan Jiang, Peng Liu, Hung-Jue Sue, and Tim Bremner. Effect of annealing on the viscoelastic behavior of poly (ether-ether-ketone). *Polymer*, 160:231–237, 2019.

[201] Hang Kuen Lau. Effect of thermal degradation on polymer thermal properties. `https://www.tainstruments.com/applications-notes/effect-of-thermal-degradation-on-polymer-thermal-properties/`, 2025. TA Instruments Application Note TA430. Controlled chain-scission lowers T_g by 9 °C. Accessed on May 29, 2025.

[202] JR Sarasua, PM Remiro, and JBAUDB Pouyet. Effects of thermal history on mechanical behavior of peek and its short-fiber composites. *Polymer composites*, 17(3):468–477, 1996.

[203] M Day, T Suprunchuk, JD Cooney, and DM Wiles. Thermal degradation of poly (aryl-ether–ether-ketone)(peek): A differential scanning calorimetry study. *Journal of applied polymer science*, 36(5):1097–1106, 1988.

[204] Dimitrios Gaitanelis, Angeliki Chanteli, Chris Worrall, Paul M Weaver, and Mihalis Kazilas. A multi-technique and multi-scale analysis of the thermal degradation of peek in laser heating. *Polymer Degradation and Stability*, 211:110282, 2023.

[205] Woldemar Voigt. *Lehrbuch der kristallphysik:(mit ausschluss der kristalloptik)*, volume 34. BG Teubner, 1910.

[206] András Reuß. Berechnung der fließgrenze von mischkristallen auf grund der plastizitätsbedingung für einkristalle. *ZAMM-Journal of Applied Mathematics and Mechanics/Zeitschrift für Angewandte Mathematik und Mechanik*, 9(1):49–58, 1929.

[207] Kalyan Kumar Phani and SK Niyogi. Young's modulus of porous brittle solids. *Journal of materials science*, 22:257–263, 1987.

[208] Zhong Ling and Jinping Hou. A nanoindentation analysis of the effects of microstructure on elastic properties of al2o3/sic composites. *Composites science and technology*, 67(15-16):3121–3129, 2007.

[209] Willi Pabst, Eva Gregorová, and Gabriela Tichá. Elasticity of porous ceramics—a critical study of modulus- porosity relations. *Journal of the European Ceramic Society*, 26(7):1085–1097, 2006.

[210] H M Ledbetter, M Lei, and S K Datta. Elastic constants of porous ceramics. 2001.

[211] Caterina Iantaffi, Chu Lun Alex Leung, George Maddison, Eral Bele, Samy Hocine, Rob Snell, Alexander Rack, Martina Meisnar, Thomas Rohr, Iain Todd, and Peter D. Lee. Laser additive manufacturing of lunar regolith simulant: New insights from in situ synchrotron x-ray imaging. *Additive Manufacturing*, 101:104711, 2025.

[212] David S McKay, Grant Heiken, Abhijit Basu, George Blanford, Steven Simon, Robert Reedy, Bevan M French, and James Papike. The lunar regolith. *Lunar sourcebook*, 567:285–356, 1991.

[213] JE Colwell, S Batiste, M Horányi, S Robertson, and Steve Sture. Lunar surface: Dust dynamics and regolith mechanics. *Reviews of Geophysics*, 45(2), 2007.

[214] Leonardo Caprio, Ali Gökhan Demir, Barbara Previtali, and Bianca Maria Colosimo. Determining the feasible conditions for processing lunar regolith simulant via laser powder bed fusion. *Additive Manufacturing*, 32:101029, 2020.

[215] Xiaoming Shi, Sam Tammas-Williams, and Matjaz Vidmar. Gateway earth isru: Manufacturing mechanical modules on the moon. In *Proceedings of the 75th International Astronautical Congress (IAC)*, Milan, Italy, 2024. International Astronautical Federation (IAF). IAC-24-C2.8.10.

[216] Vinay Kenny, Salil Bapat, and Ajay P Malshe. Exploring the feasibility of processing inconel-718 and highland regolith composite using laser-assisted powder bed fusion. *Procedia CIRP*, 121:198–203, 2024.

[217] Lunar Sourcebook. Lunar sourcebook: A user's guide to the moon. *Cambridge, UK*, 1991.

[218] Mohammad Azami, Pierre-Lucas Aubin-Fournier, Mehdi Hojjati, and Krzysztof Skonieczny.

Additive manufacturing of peek/lunar regolith composites for sustainable lunar manufacturing. *arXiv preprint arXiv:2508.00894*, 2025.

[219] Vinay Kenny, Salil Bapat, and Ajay P Malshe. Exploring the feasibility of processing inconel-718 and highland regolith composite using laser-assisted powder bed fusion. In *Procedia CIRP*, volume 121, pages 198–203. Elsevier, 2024. 11th CIRP Global Web Conference (CIRPe 2023).

[220] Sagar Patel, Allan Rogalsky, and Mihaela Vlasea. Towards understanding side-skin surface characteristics in laser powder bed fusion. *Journal of Materials Research*, (15), August 2020.

[221] G. Lumay, K. Traina, F. Boschini, V. Delaval, A. Rescaglio, R. Cloots, and N. Vandewalle. Effect of relative air humidity on the flowability of lactose powders. *Journal of Drug Delivery Science and Technology*, 35:207–212, October 2016.

[222] Silvia Vock, Burghardt Klöden, Alexander Kirchner, Thomas Weißgärber, and Bernd Kieback. Powders for powder bed fusion: a review. *Progress in Additive Manufacturing*, 4(4):383–397, December 2019.

[223] Dietmar Schulze. Properties exhibited by some bulk solids. In *Powders and Bulk Solids: Behavior, Characterization, Storage and Flow*, pages 199–230. Springer Berlin Heidelberg, Berlin, Heidelberg, 2008.